



# Review: Pair distribution functions from neutron total scattering for the study of local structure in disordered materials

Martin T. Dove<sup>a,b,c,\*</sup>, Gong Li<sup>d</sup>

<sup>a</sup> College of Computer Science, Sichuan University, Chengdu, 610065, Sichuan, China

<sup>b</sup> School of Mechanical Engineering, Dongguan University of Technology, Dongguan, 523808, Guangzhou, China

<sup>c</sup> School of Physical and Chemical Sciences, Queen Mary University of London, Mile End Road, London, E1 4NS, United Kingdom

<sup>d</sup> State Key Laboratory of Metastable Materials Science and Technology, Yanshan University, Qinhuangdao, 066004, Hebei, China

## ARTICLE INFO

### Keywords:

Pair distribution function

Neutron scattering

Local structure

## ABSTRACT

With the development of pulsed spallation sources of neutrons in recent years has come the possibility to generate intense beams of higher energy than possible at reactor sources. This has enabled neutron total scattering methods to develop significantly for studies across a wide range of application areas. In this article we will review the background theory for analysis of total scattering in terms of the pair distribution function, we will review modern facilities and instrumentation, we will describe a range of analysis methods, and finally we will present a number of examples of recent work that illustrate many of the ideas discussed here.

## Contents

1. Introduction .....	2
2. Background ideas: underpinning theory and practical issues .....	3
2.1. Origin of the neutron scattering law: the Debye equation .....	3
2.2. Introducing the pair distribution function .....	3
2.3. Example of the PDF from a simple system .....	4
2.4. Warning! the scientific community does not have an agreed nomenclature .....	5
2.5. Some practical issues .....	6
2.6. Calculations of the PDF .....	6
3. Facilities .....	7
3.1. Neutron beams .....	7
3.2. Synchrotron radiation .....	10
3.3. Laboratory x-ray sources for PDF measurements .....	10
3.4. Brief comparison of different types of radiation for user applications .....	11
4. Brief discussion of data treatment .....	13
4.1. Neutron total scattering .....	13
4.1.1. Data corrections .....	13
4.1.2. Data normalisation .....	14
4.1.3. Corrections for inelastic effects .....	14
4.1.4. User experience and user responsibility .....	15
4.1.5. Software .....	15
4.2. X-ray total scattering .....	16
5. Analysis of the PDF .....	16
5.1. Fingerprint-type analysis .....	16
5.2. Peak fitting .....	17
5.3. Fitting the whole PDF .....	17

\* Corresponding author. College of Computer Science, Sichuan University, Chengdu, 610065, Sichuan, China.

E-mail addresses: [martin.dove@scu.edu.cn](mailto:martin.dove@scu.edu.cn) (M.T. Dove), [gongli@ysu.edu.cn](mailto:gongli@ysu.edu.cn) (G. Li).

5.4.	The reverse Monte Carlo method	18
5.5.	Empirical Potential Structure Refinement method	19
5.6.	Comparison and guidance	19
6.	PDF studies in the 2020s	20
7.	Examples of PDF studies	20
7.1.	Atomic structure of an organic amorphous network	20
7.2.	Negative thermal expansion in scandium trifluoride	21
7.3.	Local order in high-entropy alloys	22
7.4.	Deep eutectic organic mixtures with water	23
7.5.	Atomic and magnetic structure of iron-oxide nanoparticles	24
7.6.	Spin-ice physics in cadmium cyanide	25
8.	Discussion and forward look	25
9.	Summary	27
10.	Appendix: neutron–nuclei data	27
10.1.	Values of the neutron scattering lengths	27
10.2.	The case of hydrogen	27
10.3.	Some absorbing elements	28
	Use of figures from other papers	29
	CRediT authorship contribution statement	29
	Declaration of competing interest	29
	Acknowledgements	29
	References	29

## Abbreviations

DES	Deep Eutectic Solvent
EPSR	Empirical Potential Structure Refinement
HEA	High Entropy Alloy
MD	Molecular Dynamics
NTE	Negative Thermal Expansion
PAF	Porous Aromatic Framework
PDF	Pair Distribution Function
RMC	Reverse Monte Carlo
RUM	Rigid Unit Mode
SDF	Spatial Distribution Function

## 1. Introduction

Soon after the discovery of x-rays [1–3], it was demonstrated that x-rays can be diffracted by crystals [4–7], and that they must therefore have wave properties. Moreover, it was realised that the diffracted intensity contains information about the positions of atoms inside the crystals [8,9], and within a remarkably short period of time the scientific methods of x-ray crystallography were developed [10]. Some years later, after the discovery of nuclear fission and the subsequent development of the first nuclear reactors, it was possible to extend the methods of x-ray crystallography to work with beams of neutrons [11].

Crystallography has a formalism that allows the atomic structure of crystals to be determined with both high precision and high accuracy, even for very complicated crystal structures. Thus we may think we know where the atoms are located inside a crystal. On the other hand, for disordered materials – whether fluids, glasses or disordered crystalline materials – this situation is much less satisfactory. Indeed, for a fluid or glass the idea of knowing where the atoms are is fanciful. What we need in this case is not the absolute positions of atoms but the relative positions of groups of atoms over short length scales. We will call this the *local structure*. For a disordered crystal, such as one where atoms can hop between related sites, or where molecules are freely tumbling, or where there is such high ionic conductivity that it is not reasonable to identify

specific locations to the mobile ions, the concept of local structure is as important as the overall crystal structure.

The basic theory of the scattering of radiation from disordered atomic systems, which leads to a mathematical description of the local structure, was established reasonably soon after the development of the first formalism of Bragg diffraction [12–14]. However, there were several problems faced by early experimentalists, not least of which was that collection of data of sufficient quality to extract quantitative information is hard to achieve. We will discuss this point in more detail towards the end of the next section. It was with the developments of the means to produce beams of (relatively) high-energy neutrons that led to measurements of local structure becoming part of the mainstream scientific investigation of disordered materials.

The key quantity in the analysis is the *pair distribution function* (PDF), which is a one-dimensional function that is based on a histogram of instantaneous distances between all pairs of atoms. We define this more precisely in Section 2 – in fact we will see that there is more than one definition – but the looser understanding of the PDF reflecting the histogram of distances is conceptually useful. In particular, the PDF will have peaks corresponding to first, second, third neighbours etc, and these contain exact quantitative information about the mean neighbour distances, numbers of neighbouring atoms, and the amplitude of local vibrational motion.

In fact, at the time of writing, the international situation for studies of local structure in disordered materials using PDF methods is very healthy, with several new facilities becoming available for researchers at both neutron and synchrotron x-ray sources (see Section 3). For this reason it was felt opportune to prepare this review with an explicit pedagogical objective. We will attempt to explain the essential ideas behind the experimental determination of the PDF, discuss a number of practical points, and present some illustrative examples. Whilst local scattering studies using the scattering of radiation are available for both neutrons and x-rays, we will focus mostly on neutron scattering methods, given the remit of the journal. It is sufficient to note that there is considerable overlap of the basic ideas for both neutron and x-ray methods, and we will discuss how in some cases the two types of radiation can act as complementary rather than competing methods. Complementary information about local structure can also be obtained by x-ray absorption methods; we refer to recent reviews for more information [15].

For more in-depth background information, the reader is recommended to consult the excellent book by Egami and Billinge [16]. We also recommend two reviews with a historical perspective, by Gelisio & Scardi [14] and Keen [17]. Some historical background information on the rise of x-ray PDF methods has recently been provided by Billinge [18]. Young and Goodwin have also provided a useful review of the

application of PDF methods to problems in materials chemistry [19].

The next section is devoted to the background information. We recognise that many readers will not want to read about the underpinning formalism, and so we aim to make the presentation of background theory as light as possible. However, there are a number of important points that emerge from understanding the background formalism, and so we will aim to focus our presentation on these. Section 2 also presents an example of the form of the PDF for a real example, using it to highlight some important features. We will note that there is more than one way to present the PDF, and indeed there is more than one nomenclature for describing the PDF; both have the potential to confuse the new user! In Section 2 we also discuss some practical issues, and describe ways in which the PDF can be calculated from a prior model. Section 3 describes facilities that are available for measurement of the PDF. Due to the scope of this article, we focus mostly on neutron methods, but we make comparison with synchrotron x-ray methods and introduce modern laboratory x-ray methods. In Section 4 we briefly describe methods for treating total scattering data, again with more emphasis on neutron data but providing information on the essential differences between methods for treating x-ray and neutron data. Then in Section 5 we describe five different methods for quantitative analysis of PDF data. Section 6, entitled 'PDF studies in the 2020s' is a summary of all this information, but we give a number of warnings concerning some trends we see developing as PDF methods become more easily available to the wider scientific community. In Section 7 we describe a number of different examples of modern use of neutron PDF methods across a range of science areas. Finally in Section 8 we make some concluding comments.

## 2. Background ideas: underpinning theory and practical issues

### 2.1. Origin of the neutron scattering law: the Debye equation

In this first part we present a semi-classical derivation of the neutron scattering law for a configuration of atoms, and thereby show how the pair distribution function can be obtained directly from total scattering data. In order to make the discussion accessible to the non-expert, we will take a relatively simplified approach, since our objective is not to give a comprehensive understanding but instead to provide the key essential insights.

Our starting point is to consider the scattering of a wave from a pair of point particles, as illustrated in Fig. 1. An incoming wave of wave vector  $\mathbf{k}_i$  is incident on the two atoms, and then scattered from both with final wave vector  $\mathbf{k}_f$ . The scattering from the two distinct point particles with separation  $\mathbf{r}$  leads to a relative path difference for the two of  $r \cos \alpha_1 - r \cos \alpha_2 = (-\mathbf{k}_i/k_i + \mathbf{k}_f/k_f) \cdot \mathbf{r}$ , as defined in Fig. 1. This translates to a phase difference of  $\mathbf{Q} \cdot \mathbf{r}$ , where  $\mathbf{Q} = \mathbf{k}_f - \mathbf{k}_i$ , and is called the *scattering vector*. This phase difference leads to classic interference effects.

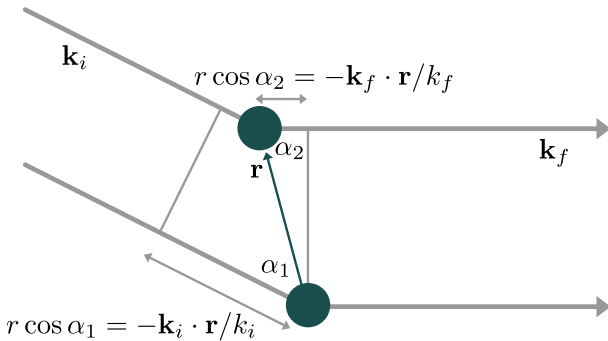


**Fig. 1.** Scattering of radiation from two atoms separated by vector  $\mathbf{r}$ . The initial (incoming) and final (scattered) wave vectors are  $\mathbf{k}_i$  and  $\mathbf{k}_f$  respectively. The two scalar distances  $r \cos \alpha_1$  and  $r \cos \alpha_2$  represent the additional path lengths of two rays. By vector products these equal  $-\mathbf{k}_i \cdot \mathbf{r}/k_i$  and  $-\mathbf{k}_f \cdot \mathbf{r}/k_f$  respectively.

Defining the position of the two point atoms as  $\mathbf{r}_1$  and  $\mathbf{r}_2$  respectively, such that  $\mathbf{r}_2 = \mathbf{r}_1 + \mathbf{r}$ , the amplitude of the scattered beam will be

$$\mathcal{F}(\mathbf{Q}) = b_1 \exp(i\mathbf{Q} \cdot \mathbf{r}_1) + b_2 \exp(i\mathbf{Q} \cdot \mathbf{r}_2) \quad (1)$$

where  $b_1$  and  $b_2$  represent the size of scattering from each point atom, called the *scattering length* for the case of neutron scattering. An experiment will measure  $|\mathcal{F}(\mathbf{Q})|^2$ , which is given as

$$|\mathcal{F}(\mathbf{Q})|^2 = b_1^2 + b_2^2 + 2b_1 b_2 \cos(\mathbf{Q} \cdot \mathbf{r}) \quad (2)$$

where the first two terms reflect the properties of the two individual atoms, and the last term reflects the interference of scattering from the relative positions of the two atoms. Note that in this equation there is no direct information on the absolute positions of the two atoms,  $\mathbf{r}_1$  and  $\mathbf{r}_2$ , only information about their separation  $\mathbf{r}$ .

This analysis can easily be generalised for a material containing many atoms, which we denote by subscript  $j$ <sup>1</sup>:

$$\mathcal{F}(\mathbf{Q}) = \sum_j b_j \exp(i\mathbf{Q} \cdot \mathbf{r}_j) \quad (3)$$

with overall scattering function

$$S(\mathbf{Q}) = \frac{1}{N} |\mathcal{F}(\mathbf{Q})|^2 = \frac{1}{N} \sum_{jk} b_j b_k \exp(i\mathbf{Q} \cdot \mathbf{r}_{jk}) \quad (4)$$

where  $\mathbf{r}_{jk} = \mathbf{r}_j - \mathbf{r}_k$ , and  $N$  is the total number of atoms. The factor  $1/N$  gives a normalisation.

In many cases we do not require – or practically care about – the relative orientations of  $\mathbf{Q}$  and the vectors between pairs of atoms,  $\mathbf{r}_{jk}$ . Thus it is common to consider the average over all relative orientations of these two vectors, which is written mathematically as

$$\langle \exp(i\mathbf{Q} \cdot \mathbf{r}_{jk}) \rangle = \frac{1}{4\pi} \int_0^{2\pi} d\phi \int_0^\pi \exp(iQr_{jk} \cos \theta) \sin \theta d\theta \quad (5)$$

where  $Q = |\mathbf{Q}|$ ,  $r_{jk} = |\mathbf{r}_{jk}|$ ,  $\theta$  is the polar angle between  $\mathbf{Q}$  and  $\mathbf{r}_{jk}$ , and  $\phi$  is the corresponding azimuthal angle. We substitute  $x = \cos \theta$  so that  $-\sin \theta d\theta = dx$ . The integration over  $\phi$  is trivial, giving us the simple factor of  $2\pi$  which cancels with the spherical volume factor of  $1/4\pi$ , and thus we have

$$\langle \exp(i\mathbf{Q} \cdot \mathbf{r}_{jk}) \rangle = \frac{1}{2} \int_{-1}^{+1} \exp(iQr_{jk}x) dx = \frac{\sin(Qr_{jk})}{Qr_{jk}} \quad (6)$$

Hence we can write the scattering function as

$$S(Q) = \frac{1}{N} \sum_{jk} b_j b_k \frac{\sin(Qr_{jk})}{Qr_{jk}} \quad (7)$$

This is the famous *Debye equation* [12,14].

### 2.2. Introducing the pair distribution function

The Debye equation is of limited practical use when the number of atoms  $N$  is large. In this case we do not want to know about the  $N^2$  values of  $r_{jk}$ , but instead we are more interested in the *distribution* of interatomic separations. To start we note that equation (7) contains terms where the two atoms are the same, namely  $j = k$ , and it is useful to separate these from the terms with  $j \neq k$ :

<sup>1</sup> We use the symbol  $\mathcal{F}(\mathbf{Q})$  in direct analogy to the symbol  $F(\mathbf{Q})$  used for the crystallographic structure factor, which is defined in a similar way. In fact  $F(\mathbf{Q}) = \langle \mathcal{F}(\mathbf{Q}) \rangle$ , where the average is over all unit cells in the crystal.

$$S(Q) = \frac{1}{N} \sum_j b_j^2 + \frac{1}{N} \sum_{j \neq k} b_j b_k \frac{\sin(Qr_{jk})}{Qr_{jk}} \quad (8)$$

The first term – known as the *self-scattering term* – contains no information about the individual atoms, and it is more useful to represent this as a sum over atom type rather than over individual atoms. We denote  $c_m$  as the fraction of atoms of type  $m$ , with  $\sum_m c_m = 1$ , so the self-scattering term can be written as

$$\frac{1}{N} \sum_j b_j^2 = \sum_m c_m b_m^2 \quad (9)$$

The second term in equation (8) can also be represented in terms of atom types, using the distribution of distances between atoms of two types. We consider an atom of type  $m$ , surrounded by a spherical shell of radius  $r$  and infinitesimal thickness  $dr$ . The average number of atoms of type  $n$  lying within this shell can be written as a product of the volume of this shell,  $4\pi r^2 dr$ , the density of atoms of type  $n$ ,  $c_n \rho$  ( $\rho$  is the total number of atoms per unit volume) and a factor to account for the correlation between atomic positions,  $g_{mn}(r)$  (this factor has value  $g = 1$  for a random distribution of atoms). Thus the average number of atoms of type  $n$  lying within these spherical shells around atoms of type  $m$  is given as  $4\pi r^2 dr \times c_n \rho \times g_{mn}(r)$ . We can therefore replace the summation in equation (8) by an integral over the distribution function:

$$\frac{1}{N} \sum_{j \neq k} b_j b_k \frac{\sin(Qr_{jk})}{Qr_{jk}} = 4\pi \rho \int \sum_{m,n} c_m c_n b_m b_n r^2 g_{mn}(r) \frac{\sin(Qr)}{Qr} dr \quad (10)$$

The function  $g_{mn}(r)$  has two limiting properties:  $g_{mn}(r < r_{\min}) = 0$  and  $g_{mn}(r \rightarrow \infty) = 1$ . The first reflects the fact that there is a minimum distance  $r_{\min}$  between any pairs of atoms, related to the finite sizes of atoms, and the second reflects the fact that when the spherical shell has a large volume it will contain a correspondingly large number of atoms with a distribution of atom types that is indistinguishable from that given by a random distribution of atoms.

Reflecting the second of these limits, it is appropriate to rewrite equation (8) as

$$S(Q) = \sum_m c_m b_m^2 + i(Q) + S_0 \quad (11)$$

where

$$i(Q) = 4\pi \rho \int \sum_{m,n} c_m c_n b_m b_n r^2 (g_{mn}(r) - 1) \frac{\sin(Qr)}{Qr} dr \quad (12)$$

and

$$S_0 = 4\pi \rho \int \sum_{m,n} c_m c_n b_m b_n r^2 \frac{\sin(Qr)}{Qr} dr \quad (13)$$

This integral gives a delta function at  $Q = 0$ , so that  $S_0$  is in practice impossible to measure.

Equation (12) is the important one containing the information about the pair distribution function. We can take account of the various factors by defining

$$D(r) = 4\pi \rho r \sum_{m,n} c_m c_n b_m b_n (g_{mn}(r) - 1) \quad (14)$$

With this definition we can rearrange equation (12) as

$$Qi(Q) = \int_0^\infty D(r) \sin(Qr) dr \quad (15)$$

This has the reverse transformation:

$$D(r) = \frac{2}{\pi} \int_0^\infty Qi(Q) \sin(Qr) dr \quad (16)$$

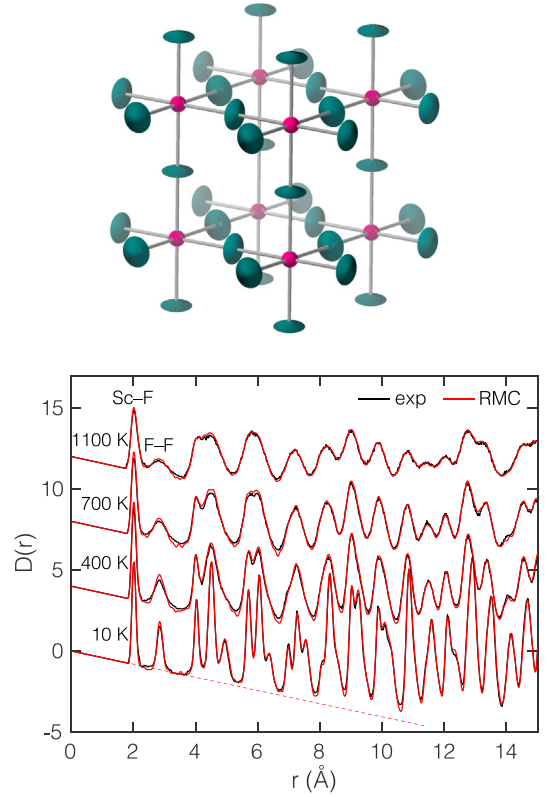


**Fig. 2.** Example of the PDF  $D(r)$  for  $\text{ScF}_3$  (crystal structure shown above) measured by neutron scattering (black curves) and fitted by RMC analysis (red curves) [20], shown for a selection of temperatures (below). The dashed red line associated with the data for 10 K shows the expected baseline for the PDF.

$D(r)$  is the fundamental PDF, since it is the Fourier transform of the experimental scattering data.<sup>2</sup>

It should be noted that since  $g(r) = 0$  for low values of  $r$ , the limiting value of  $D(r)$  is  $-4\pi \rho \sum c_m c_n b_m b_n$ . That is,  $D(r \rightarrow 0) \propto -r$ . The baseline for  $D(r)$  is not an oscillation around  $D(r) = 0$  but a line extending downwards with gradient  $-4\pi \rho \sum c_m c_n b_m b_n$ . We will illustrate this point in detail next, where we will show a practical example.

### 2.3. Example of the PDF from a simple system

**Fig. 2** shows an example of a PDF, represented by the function  $D(r)$ , measured for the cubic material  $\text{ScF}_3$  (atomic structure shown in the figure) for a selection of temperatures using neutron total scattering [20]. The PDF data shown in this figure reveals a number of important features.

The *first* thing to notice from **Fig. 2** is that we show two sources of data, namely the experimental PDF (black lines), and curves fitted using the Reverse Monte Carlo method (discussed later in Section 5.4). The point is that it is possible to build atomic models that can reproduce the experimental PDF to an extremely high degree, including the variation with temperature, as seen in **Fig. 2**, where the temperature range is from 10 to 1100 K.

*Second*, we note that the data for low temperature shows very sharp peaks (graph marked “10 K” in **Fig. 2**). These peaks correspond to specific distances between atoms. The first two peaks correspond to the Sc-F and F-F distances within the  $\text{ScF}_6$  octahedra, as seen in the top image in **Fig. 2**. Other peaks correspond to different interatomic distances. The

<sup>2</sup> It is interesting to note that these equations first appeared in the scientific literature in a paper of Zernike and Prins in 1927 [13] in the form that is still used today.

graph for the lowest temperature in Fig. 2 is annotated with a dashed line to show the true background level of the PDF, namely where the individual pair functions have values  $g(r) = 0$  as discussed above. Identifying this background is necessary in order to be able to identify a maximum in  $D(r)$  as a pure peak instead of a combination of peaks.

This leads to our *third* point, which is illustrated by considering the data for higher temperatures in Fig. 2. On heating, atomic motions will cause broadening of the peaks in the individual  $g(r)$  functions, and eventually this will lead to an overlap of close peaks in the PDF. Consider the thermal motion indicated by the ellipsoidal representation of atoms in the crystal structure shown at the top of Fig. 2. The variance in the Sc–F distance increases slightly with temperature, but because of the significant amplitude of transverse motions, the variance in the F–F distances increases much more rapidly on heating. This can clearly be seen as broadening of the second peak (F–F) in the PDF at 2.8 Å, in contrast to the first peak (S–F) at 2 Å. Furthermore, the third (4 Å, corresponding to pairs of atoms related by a single lattice repeat), fourth (4.5 Å) and fifth (4.9 Å) peaks are seen as distinct peaks at low temperature, but these are merged into a single feature at around 4.2 Å at high temperature. Whilst this feature at high-temperature has a shape suggestive of being a composite of more than one peak, this cannot be said to be the case for the ‘peak’ just below 6 Å at high temperature. This has no features to suggest that it is a composite peak, but at low temperature it can be seen to be composed of two relatively strong peaks and a third weaker peak.

Our *fourth* point is that it is very important to be able to see, or at least identify, the baseline in the PDF – the downwards sloping line in  $D(r)$  that is marked as the dashed line in Fig. 2 – at least at low temperatures when the peaks in the PDF are relatively sharp. If the baseline is not clear, the implication is that probably most features in the PDF represent broad and overlapping peaks, rather than individual peaks. The data for low temperature shown in Fig. 2 can only be analysed in terms of individual peaks up to a distance of 11 Å; at high temperature this distance is as low as 4 Å. Where the baseline is not clear, interpretation of the features in a PDF needs to be done with considerable care. And for certain, features in the PDF where the baseline is not clear should not be interpreted too easily as representing individual peaks. An example of this danger is seen at distance of around 14.1 Å in Fig. 2. The data at low temperature show a peak at this distance, but on heating, as the peaks in the PDF broaden due to thermal motion, the peak at 14.1 Å contributes to the PDF at a lower level than the two peaks either side, and appears as a dip in the PDF. That dip is still a peak in the PDF, but most researchers will naturally consider the PDF at 14.1 Å to merely represent a part of the PDF lying between two peaks at 13.5 and 14.8 Å.

*Fifthly*, note that the PDF functions in Fig. 2 are plotted all the way down to zero values of  $r$ . We observe that it is common practice to plot the PDF only down to a value of  $r$  that is slightly below the position of the first peak. On one hand this practice may appear to be maximising the real estate of the space contained within the axes of the graph, given that  $D(r)$  is not obviously interesting for smaller values of  $r$ . However, as argued by Adrian Wright [21], the quality of the PDF for lower values of  $r$  gives an indication of the overall quality of the scattering data, and particularly whether there are systematic errors of unknown origin. These may arise from poor choices in the data correction/normalisation process, inadequate range of  $Q$ , inadequate knowledge of the sample (particularly if there is chemical substitutions), wrong estimates of the amount of sample seen by the neutron beam, impurities within the sample that have absorption resonance energies within range of the useful part of the neutron beam (such as Hf impurities in oxides of Zr), effects of magnetic scattering that are not taken into account, and inadequate corrections for the effects of inelastic processes. Some of these issues are discussed in an older paper concerning data corrections for ISIS data [22]. Thus, following Adrian Wright [21], we argue that published graphs of the PDF should always extend down to  $r = 0$ .

Our *sixth* point is that data in Fig. 2 show clearly the two limiting cases, namely  $D(r)$  as  $r \rightarrow 0$  and  $r \rightarrow \infty$ . By showing both cases, it is clear that the function being plotted really is  $D(r)$ , with a linear downward slope in the first limit and oscillation around zero in the second. We have seen many cases where the PDF, often called  $G(r)$ , is not defined mathematically in the paper (as if everyone naturally knows what function is being plotted; see the discussion in Section 2.4), and where the two limiting cases of the displayed PDF (which are rarely shown down to  $r = 0$ ) do not indicate which form of the PDF is being displayed. In particular, it often seems that the  $r \rightarrow 0$  limiting form of the PDF is so badly damaged through the data correction procedures that it is impossible to tell from the data what is actually being plotted. This takes us back to the previous point.

#### 2.4. Warning! the scientific community does not have an agreed nomenclature

Before we go any further, we want to point out that the scientific community does not agree on how to represent the quantities we have discussed here. Even the name is not unique, with the term *pair distribution function* (PDF) superseding the older term *radial distribution function*. In our opinion there is no value in attempting to identify separate subtle differences in meaning between these two terms; they are used synonymously sufficiently often that there is no point trying to be pedantic.

Of more importance for any reader of papers reporting studies of pair distribution functions is that there is more than one nomenclature for the basic quantities. David Keen [23] has published a very helpful comparison of different nomenclatures. The most important point for readers of the literature is that what we have called  $D(r)$  is often represented by the symbol  $G(r)$ .

Whilst it may not matter too much what we call things, it does matter that researchers understand that different sets of symbols are used for similar quantities. Briefly we point out that there is a reason why some workers prefer  $D(r)$  over  $G(r)$ . Let us define some basic pair functions derived from  $g_{mn}(r)$ :  $t_{mn}(r) = rg_{mn}(r)$ , and  $d_{mn}(r) = r(g_{mn}(r) - 1)$ . Clearly we can then define

$$T(r) = 4\pi\rho \sum_{m,n} c_m c_n b_m b_n t_{mn}(r) \quad (17)$$

and

$$D(r) = 4\pi\rho \sum_{m,n} c_m c_n b_m b_n d_{mn}(r) \quad (18)$$

But what should we call this potentially useful function:

$$4\pi\rho \sum_{m,n} c_m c_n b_m b_n g_{mn}(r) ? \quad (19)$$

We would ideally have called this  $G(r)$  by analogy; you can immediately see why we prefer to use  $D(r)$  for the PDF represented by equation (18). We note that this is not an idle question; later we will cite work [24] in which both functional forms of equations (18) and (19) are used, with the labels  $D(r)$  and  $G(r)$  applied respectively, sensibly so.

The function  $T(r)$ , which we have introduced here, is preferred by some established workers [21,25,26]. This has the property that at low  $r$  the baseline is zero rather than the downward linear slope of  $D(r)$ . This makes fitting a peak-shape function (such as a symmetrical Gaussian) to the peaks in the PDF rather more natural. At higher values of  $r$ , where  $g(r)$  oscillates around unity and  $D(r)$  oscillates around zero,  $T(r)$  consists of oscillations round a background that increases linearly with  $r$ .

It is also the case that what we have called  $i(Q)$  is sometimes called  $F(Q)$ . We prefer to avoid using  $F(Q)$  because this symbol has a long-



standing and well-established use as the structure factor in crystallography.

The other point to be aware of is that sometimes the scattering functions  $S(Q)$  and the PDFs are presented in a way that has some measure of normalisation, rather than being on the absolute scale set by equations (14), (16) and (18). Thus,  $S(Q \rightarrow \infty) = 1$  using a definition of a normalised function, but  $S(Q \rightarrow \infty) = \sum c_m b_m^2$  in the definition we are using here (equations (8) and (11)).<sup>3</sup>

## 2.5. Some practical issues

The application of the key equations (15) and (16) is less straightforward than appears at first sight, because in practice it is not easy to fulfil the condition of integrating between the limits of zero to infinity. The most pressing question is that of how close to infinity is necessary to get a good transformation. The common answer to this question – that in practice the ideal case is  $Q_{\max} > 20 \text{ \AA}^{-1}$  – meant that most studies of the PDF of disordered materials with x-rays were initially limited to a few demonstrations. It was with the advent of sources of higher energy neutrons, obtained using hot moderators in the cores of nuclear reactors designed to produce neutron beams, that enabled PDF measurements of liquids and glasses to become routine [25]. The capabilities of PDF measurements with neutron beams were further extended with the use of spallation sources of neutrons, where measurements up to  $Q = 50 \text{ \AA}^{-1}$  are routine [27,28]. It is important to appreciate that the resolution of the PDF is restricted by the value of  $Q_{\max}$ : the effective best resolution in the features in the PDF is given as  $\Delta r = 2\pi/Q_{\max}$ . With a small value of  $Q_{\max}$  the resolution may be too poor to see important features within the PDF. Some aspects of the significance of this were explored in a round-robin comparison of PDFs extracted from neutron total scattering data obtained at 6 instruments in three of the then-operating (2004) pulsed spallation neutron facilities [29].

Even with the ability to measure the total scattering to high values of  $Q$ , giving a reasonable value of the resolution  $\Delta r$ , the problems with a finite range of  $Q$  are not eliminated. Mathematically, the total scattering can be described as the ideal case (total scattering measured to  $Q_{\max} \rightarrow \infty$ ) multiplied by the box function  $M_{\text{box}}(Q) = 1$  for  $0 < Q < Q_{\max}$ ,  $M_{\text{box}}(Q) = 0$  for  $Q > Q_{\max}$ . The Fourier transform of  $Q_i(Q)$  will be that of the ideal case – the perfect  $D(r)$  – convolved by the Fourier transform of  $M_{\text{box}}(Q)$ . This will be the sinc function, with a central peak at the origin and a series of oscillations either side of the central peak. When a sharp peak in the PDF  $D(r)$  – usually the first peak – is convolved with this function, it will generate a series of spurious ripples either side of the peak. These ripples, known as *termination ripples*, appear as noise to the lower- $r$  side of the first sharp peak, but on the higher- $r$  side the termination ripples will overlap with the true peaks in the PDF. In the best case the experienced researcher can take account of the presence of termination ripples in analysis of the PDF, but in the worst case the inexperienced researcher may interpret the termination ripples as real features. This can be a great risk when the position of the peaks in the termination ripples correspond to distances that the researcher may recognise as those associated with chemical bonds.

A common approach is to multiply  $Q_i(Q)$  by a modification function  $M(Q)$  prior to Fourier transform [21,25,26], so that the practical transform is

$$D'(r) = \frac{2}{\pi} \int_0^{Q_{\max}} M(Q) Q_i(Q) \sin(Qr) dr \quad (20)$$

Ideally  $M(Q)$  falls continuously to zero as  $Q \rightarrow Q_{\max}$ . A commonly-

used modification function is that proposed by Lorch [30,31]:

$$M(Q) = \frac{\sin(\pi Q/Q_{\max})}{\pi Q/Q_{\max}} \quad (21)$$

This has the desired properties of  $M(Q \rightarrow 0) \rightarrow 1$  and  $M(Q \rightarrow Q_{\max}) \rightarrow 0$ .<sup>4</sup>

Application of the modification function leads to significant suppression of termination ripples. Mathematically, in the Fourier transform, the product of  $M(Q)$  and  $Q_i(Q)$  leads to convolution of the derived  $D(r)$  with the Fourier transform of  $M(Q)$ .<sup>5</sup> This transform, from above, is the box function, so essentially the application of the Lorch modification function is equivalent to performing a smoothing operation by averaging neighbouring points in the derived  $D(r)$ .

The use of  $M(Q)$  has another practical advantage. In general we might expect a measurement of  $i(Q)$  to be statistically of lower quality at the higher- $Q$  end of the data, where the value of  $i(Q)$  oscillates around the value zero. The quantity we need for Fourier transform is  $Q_i(Q)$ , and the multiplication by  $Q$  will further increase the amplitude of the noise at higher values of  $Q$ . Thus a second advantage of the use of the modification function is to suppress the effect of noise feeding through to the resultant PDF.

Some time ago Andrey Krylov and Andrey Vvedenskii [33] pointed out that the PDF can be fitted using Hermite functions [34]. These functions have the useful feature that they are the eigenfunctions of the Fourier transform operation, and thus by fitting  $Q_i(Q)$  using Hermite functions it is possible to obtain the PDF directly by recombining the Hermite functions. This method was initially applied only to data for liquids with a short range of scattering data, up to 8 or 12  $\text{\AA}^{-1}$ , giving PDFs for distances up to 8 and 12  $\text{\AA}$  respectively. This approach has not been used significantly since the initial test work, but we have recently revisited it [35], making some changes in line with the use of modern spallation neutron sources (particularly the wider range of values of  $Q$ ), and taking account of the effects of resolution.

A preliminary example from our work using Hermite functions to fit the scattering function is shown in Fig. 3 [35]. This shows fitting of the  $Q_i(Q)$  function for amorphous silica [32], measured using the GEM diffractometer at ISIS [28,36] and formed by merging (by hand) data from different banks of detectors. The scattering data have been multiplied by the modification function  $M(Q)$  given by equation (21) prior to fitting. Fig. 3a shows that the expansion of the scattering function in terms of Hermite function gives a very good description of the data, and the method is able to fit smoothly through the noise in the data at higher values of  $Q$ . The corresponding PDF  $D(r)$  is seen to be reasonable, and in good agreement with earlier high-quality data [21], albeit that we are comparing our  $D(r)$  function with the reported  $T(r)$  function.

## 2.6. Calculations of the PDF

In any experimental study of the PDF, it is often useful to calculate a theoretical PDF for comparison with measurement. For a disordered system, such as a fluid or glass, this can be formed from an appropriate simulation, for example from a molecular dynamics (MD) model. With a sufficient number of atoms, and with sufficient averaging over

<sup>4</sup> In the hope that it is not necessary to say this, but for completeness, in the cases where  $Q_{\max}$  is chosen by the researcher to be lower than the upper limit of the range of the data, we have  $M(Q > Q_{\max}) = 0$ .

<sup>5</sup> In this context, we want to remark that it is actually useful for researchers using the PDF method to have some intuition about one-dimensional Fourier transforms, including the mathematical concept of convolution, how the convolution operation in one space converts to a multiplication in the Fourier transform, and how the finite resolution in  $Q$ -space leads to damping of the PDF at higher  $r$ . Not only are these insights useful in understanding issues such as the origin and treatment of termination ripples, and the technique of “zero padding” when performing practical Fourier transforms, but will also be necessary to understand the treatment of x-ray total scattering data discussed in Section 4.2.

<sup>3</sup> David Keen [23] has pointed out that the normalised form of  $S(Q)$  is more commonly used within the PDF community rather than the absolute form cited here. However, those of us who first learned that  $S(Q)$  is derived from the integral of the dynamical scattering function,  $S(Q) = \int S(Q, \omega) d\omega$ , will be more naturally inclined to work with the form of  $S(Q)$  in absolute units.

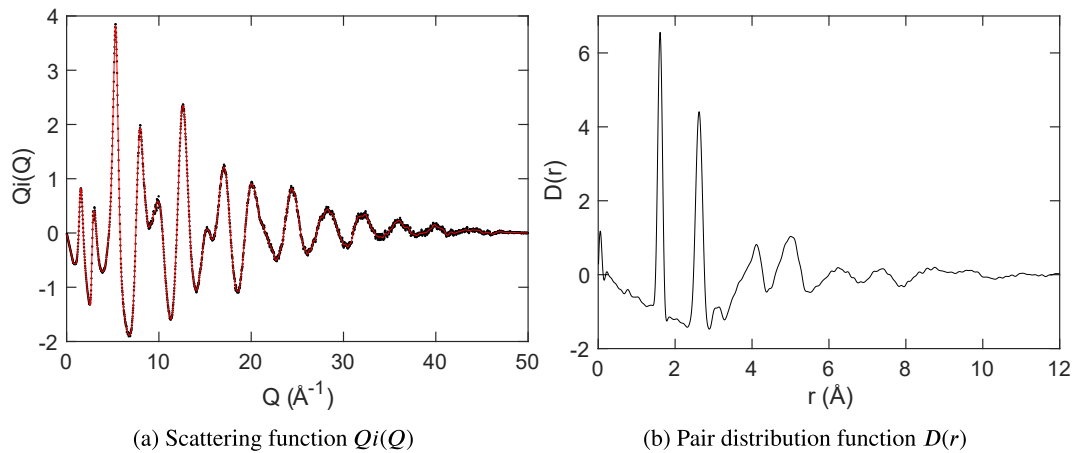


**Fig. 3.** Example of a) fitting the scattering function  $Q_i(Q)$  to neutron scattering data for amorphous silica [32] using Hermite functions; and b) the derived pair distribution function  $D(r)$  over the interesting range of distances. In (a) the data are shown as black points and the red curve shows the fitted function. (For interpretation of the references to colour in this figure legend, the reader is referred to the Web version of this article.)

independent configurations, the PDF may be a reasonable approximation of the experimental PDF.

For a crystal it is possible to compute a PDF from a list of interatomic distances, with each distance giving the centre of a Gaussian function of width selected by the researcher. There are a number of structure plotting software tools that can do this automatically, such as CrystalMaker [37].

Because the user's choice of a width is arbitrary, and will typically apply to all peaks in the PDF equally (Fig. 2 is a case where the peaks in the PDF clearly do not have equal width), we developed a package for the GULP lattice simulation code [38,39] in which the widths of each peak in the PDF could be obtained directly from a lattice dynamics calculation [40]. This approach has the advantage of incorporating peak shapes that explicitly reflect the different atomic motions, meaning that if there are sharp and broad peaks in the experimental PDF, these will be reproduced in the calculation. The only requirement for this type of calculation is a model of interatomic forces that is part-way realistic. Such a level of realism can be achieved using very simple models in fact. The main requirement about realism is that the experimental crystal structure should be reproduced by the lattice simulation, that none of the phonons should have imaginary frequencies characteristic of a structural instability, and that broadly vibrations that stretch bonds should have higher frequencies than those that bend bond angles. This approach has been used to assess structural models of the cubic phase of cristobalite [41], a polymorph of  $\text{SiO}_2$ , and to understand the role of the frequency spectrum on the PDF of  $\text{SrTiO}_3$  [42]. The approach was also used to identify the phases present in  $\text{CdS}$  nanoparticles [43].

### 3. Facilities

#### 3.1. Neutron beams

From the outset [45], research with neutron beams was based on the generation of neutrons within a nuclear fission reactor.<sup>6</sup> From the 1960s many research reactors with beam-lines for neutron scattering were constructed in many countries, but over the years a large number have

closed without replacement. Indeed, several of the major reactor facilities, as given in Table 1, are now very old, having been refurbished to prolong their lifespan. Amongst these are two of the leading sources, at the Institute Laue-Langevin in France and at Oak Ridge National Laboratory in the USA. The only modern reactor sources are the FRM-II facility in Germany and the OPAL facility in Australia. Other facilities worldwide operate on a smaller scale, with another 6 in Europe that go down to the scale of being a training reactor with just 2 instruments. The same is true in the USA, where there are 3 small reactor facilities that are operational with as few as 2 instruments. A number of other reactor facilities worldwide may potentially come online in the future following extended shutdowns or lengthy refurbishment.

The facilities given in Table 1 all offer access to external users. The list includes both the major reactor sources and also the five international spallation neutron sources. Readers interested in wider aspects of neutron scattering for studies of the structure and properties of materials, including the technical details of the generation of neutron beams, detector methods, and instrumentation, are referred to recent books by Willis and Carlile [48], Carpenter and Loong [49] and Boothroyd [50].

Because nuclear fission reactors operate at thermal energies, the spectrum of neutrons that are reflected from within the reactor into beam

**Table 1**

Some of the major international and national neutron sources in the world that are current operating with external user programmes [44]. In the case of the ILL, where we designate France/Europe as the country, it indicates that France is hosting a pan-European facility funded by a number of countries that are members of the facility consortium.

Source/Institute	Country
<i>Spallation neutron sources</i>	
CSNS/IHEP	China
JSNS/J-PARC	Japan
SNS/ORNL	USA
ISIS/RAL	United Kingdom
SINQ/PSI	Switzerland
<i>Reactor neutron sources</i>	
CARR/CLAE	China
CMRR/CAEP	China
OPAL/ANSTO	Australia
JRR-3M/JAERI	Japan
HANARO/KAERI	Korea
HFIR/ORNL	USA
HFR/ILL	France/Europe
FRM-II/MLZ	Germany

<sup>6</sup> The timeline from the discovery to exploitation of neutrons in materials research is interesting, and similar to that for X-rays as discussed in the Introduction. The neutron was discovered by James Chadwick in 1932 [46]. Four years later Mitchell and Powers [47] showed that neutrons possess wave properties, and observed that they can be Bragg-diffracted by a crystal. The seminal paper on the first use of neutron beams for crystal diffraction experiments was published in 1948 by Wollan and Shull [11].

tubes leading to the instruments is too low to generate high values of  $Q$ . For studies of highly-disordered fluids, where the PDF contains only two broad peaks, the neutron scattering function contains very little detail at higher values of  $Q$ , and the limited range of values of  $Q$  need not matter. However, for studies of disordered materials where there is a distinct local structure, such as for amorphous silica which has a precise arrangement of  $\text{SiO}_4$  tetrahedra, linked at corners, within a continuous random network, the very sharp nature of the first peaks in the PDF leads to the existence of oscillations within the scattering function that extend to very high  $Q$  (see the example in Fig. 3 and data presented in some previous publications [21,32]). Thus a reactor source of neutrons suitable for PDF measurements needs to be able to provide a spectrum of high-energy neutrons. This is achieved using a special moderator held at high temperatures; neutrons reach a thermal equilibrium within this moderator with much higher energies – and hence lower wavelengths – than in the thermally-moderated neutron reflectors in a normal fission reactor.

The major ‘hot source’ for neutron beams available worldwide is at the Institute Laue-Langevin (ILL) in France [51], provided by a graphite block that is held at a temperature of around 2400 K. Until recently a hot source of temperature 1400 K had been available at the Orphée reactor of the Laboratoire Léon Brillouin (LLB) [52], also in France, but this reactor was taken out of service in 2019. The ILL facility has a dedicated PDF instrument on one of the beam-lines from the hot source, denoted as D4 [53,54], which has seen a number of upgrades since it was first installed. Until the reactor closure, the LLB had a similar PDF instrument, denoted as 7C2 [55]. Whilst this reference may only appear to have historical value, it does provide a very good description of PDF instrumentation on a reactor facility with a hot source, and is worth reading for this reason.

The major difficulty faced by fission reactor sources of neutrons is that it is very hard to increase the neutron flux without significant safety – and hence cost – implications. Thus in contrast with synchrotron sources, which have seen orders-of-magnitude increases in photon flux, the neutron flux from fission reactor sources has barely increased in decades. Instead, gains in the performance of instruments can be achieved by increasing the flux delivered to the sample through better neutron optics, and by increasing the number of ‘useful’ neutrons within the instrument. This can typically be achieved by the use of very large numbers of detectors covering a wider proportion of the total solid angle of scattering than was possible in the past. This is enabled as much by advances in fast electronics and fast computing and data capabilities as by advances in detector technologies.

Maximising the number of useful neutrons is not only important for reactor sources, but is the key to the current exploitation of accelerator-based pulsed spallation neutron sources. The neutrons are produced by shining beams of protons onto a target of a heavy metal. A nucleus within the target material that is struck by a proton will become thermally excited, and will lose some of its excess neutrons before returning to a lower temperature. The neutrons that are lost from the nuclei will be ejected at high speeds. They can be cooled by passing them through a moderator, and then directed along beam tubes to a range of instruments.

The SINQ spallation neutron source in Switzerland [56–59], which has been in operation since 1996, is designed to produce a continuous beam of neutrons. However, the more common approach is to produce beams neutrons that are pulsed in time, and it is at these neutron sources that we find the state-of-the-art instruments for neutron PDF measurements.

Building on experiments in Japan and USA since the late 1960s, the first pulsed spallation sources operating for user experiments were the KENS facility in Japan (1980–2004) [60,61], and the Intense Pulsed

Neutron Source (IPNS, 1981–2008) [62–64]. Soon after, the ISIS facility in the UK (operating since 1984) [65–69] and the Los Alamos Neutron Science Center (LANSCE, operating since 1986, but not currently running as a general user facility<sup>7</sup>) [71,72] were established. More recently the USA constructed a new pulsed spallation neutron source (SNS, operating since 2007) at the Oak Ridge National Laboratory (ORNL) [73,74], and Japan replaced the KENS facility with the Japan Spallation Neutron Source (JSNS) at J-PARC (operating since 2008) [75–78]. China is now developing the China Spallation Neutron Source (CSNS) in the southern city of Dongguan [79–82], operating with its first instruments since 2018, and becoming the fourth such operating general user facility worldwide. These facilities all make use of short pulses of neutrons containing a spectrum of neutron energies. The wavelengths associated with individual neutrons can be determined by accurately measuring the time taken for each neutron to leave the moderator and reach the detectors. The sharpness of the pulse means that the uncertainty on the measured time will be small. For example, the neutron pulses at ISIS are typically around 30–50  $\mu\text{s}$  wide, with pulses separated by 0.02 s.

In contrast, the new European Spallation Source, currently under construction in Lund, Sweden, will operate with a long pulse of protons.

The case of the investment by the USA in its new spallation neutron source is interesting in one regard. There had been much consideration of building an advanced reactor source [83], but the costs associated with the safety implications of a high flux reactor were found to be prohibitive. Thus it was decided instead to develop a high-power spallation neutron source, co-located with the existing high-flux reactor source at ORNL [84] to be run together within the national laboratory [85].

Short-pulse spallation neutron sources have a number of general advantages [86]. Although they produce far fewer neutrons than in a reactor, a greater number can be made to be useful [74]. We can illustrate this by considering how a powder diffractometer works. In a reactor source, the incident beam must have a fixed wavelength, which is achieved by diffraction of the primary beam from a monochromator crystal. The measurement is then performed as a function of scattering angle, which can be optimised by having detectors covering most scattering angles in the plane of the sample and incoming beam. For a precise wavelength, necessary for good resolution, most of the spectrum of thermal neutrons is discarded. On the other hand, in a pulsed spallation neutron source, the measurement is performed by timing the neutrons as they travel from the moderator to the detector. The flight time for any given scattering angle is proportional to the lattice  $d$ -spacing from which any neutron is diffracted. It is usually possible to cover most of the space around the sample with detectors. But unlike in a reactor, the whole spectrum of neutrons can be used, because in a single pulse all neutrons have a nearly identical starting time. Thus, in spite of the much lower neutron flux within the instrument, a powder diffractometer at a pulsed spallation source can be built with a performance that is competitive with, or even better than, a similar instrument at a reactor source.

For PDF studies, spallation neutron sources have another advantage, which is that the spectrum of neutrons is of higher energy even than from a hot source of a reactor facility. This means that it is easy to measure to higher values of  $Q$ , up to around  $50 \text{ \AA}^{-1}$ , with sufficient statistical accuracy. Thus pulsed spallation neutron sources are ideal for PDF measurements, and PDF instruments were quickly built at the earlier facilities. These include the now-decommissioned diffractometers LAD at ISIS [27], GLAD at IPNS [87], and NPD at LANSCE [88].

The currently available instruments suitable for measurements of the PDF at neutron facilities are listed in Table 2. Some of these instruments are dedicated for PDF measurements, but others represent the fact that some very good powder diffractometers at pulsed spallation neutron facilities can also measure across a sufficient range of  $Q$  that they can be used for PDF measurements to good effect.

As a reflection of the interests and experiences of the authors, we discuss now in more detail the ISIS (the oldest pulsed spallation source in current operation as a user facility) and CSNS (the newest) spallation sources. There are in fact many similarities between the two facilities,

<sup>7</sup> LANSCE, through the Lujan Neutron Scattering Center, currently supports 5 instruments for engineering applications [70], but appears to not support a general user programme. As is often the case, the powder diffraction instrument currently operating at LANSCE, HIPPO, has several application areas and has included PDF studies amongst these.



**Table 2**

PDF instruments at neutron and synchrotron radiation facilities. Where a European country is given but followed by “Europe” in parenthesis, this is a case where the named country is hosting a pan-European facility funded by a number of countries that are members of the facility consortium. Note that not all instruments are dedicated to PDF measurements.

Facility	Country	Beam-line
<i>Neutron facilities</i> [44]		
CSNS	China	MPI [89, 90], GPPD [91]
ISIS	United Kingdom	POLARIS [92, 93], GEM [94, 28, 36], SANDALS [95, 96, 97], NIMROD [98, 99]
ILL	France (Europe)	D4 [53, 54]
ESS	Sweden (Europe)	DREAM [100]
ORNL/SNS	USA	NOMAD [101, 102], POWGEN [103]
JSNS	Japan	NOVA [104]
<i>Synchrotron facilities</i> [105]		
SSRF	China	BL14B1
DIAMOND	United Kingdom	XPfD (115-1)
ESRF	France (Europe)	ID15A, ID22, ID31
Spring-8	Japan	BL08B2, BL22XU
APS	USA	1-ID-B, B, C, E, 6-ID-D, 11-ID-B, 11-ID-C, 16-BM-D, 17-BM-B

reflecting the fact that there has been good cooperation between them since 2014. The partnership will in fact extend into the future, given that ISIS and CSNS signed a new memorandum of understanding on July 1st, 2022 for continued collaboration on aspects of accelerator-based neutron source science and technology up to and beyond 2027 [106]. We believe that such collaborations between leading neutron scattering facilities will give significant value to continued research into exploitation of this technology for scientific applications.

The layout of the ISIS facility [65–69] is shown in Fig. 4. Briefly,  $H^+$  ions are accelerated and then stripped of their electrons. The protons are then accelerated within the synchrotron ring, and shaped into two bunches on opposite sides of the ring. Then the proton beams are released from the synchrotron and directed towards the target stations (targets are made of tungsten). This process happens 50 times each second. For 4 out of 5 pulses the protons are directed at the first target station, and every fifth pulse is sent to the second target station. The neutron beam is produced at the instance the proton pulses reach the target. Currently ISIS has 19 neutron instruments fed from the first target station and 11 from the second target station. Of these, 4 are good for PDF studies.

On the first target station, GEM [28,36,94],<sup>8</sup> and POLARIS [92,93] are standard diffractometers with a large number of detectors that cover a wide range of scattering angles, making them excellent instruments for PDF studies as well as for high-throughput diffraction, and indeed a significant part of the running time of both instruments is dedicated to PDF experiments. SANDALS [95–97] is the third PDF instrument on the first target station, and it is optimised for the study of light elements by having its detectors mostly at forward scattering angles (see the discussion in Section 4.1). The PDF instrument on the second target station, NIMROD [98,99,107], follows the design principle behind the SANDALS instrument but it also has the ability to measure part of the small angle scattering signal.

Fig. 5 gives a user's view of one side of ISIS, showing in the foreground the POLARIS diffractometer. The photograph shows the main target area in which the beams of neutrons are produced. Most instruments and their beam guides are hidden under the floor level, but the photograph gives an idea of the working environment and the scale of the facility.

The CSNS facility [79–82] is broadly similar to how ISIS was prior to

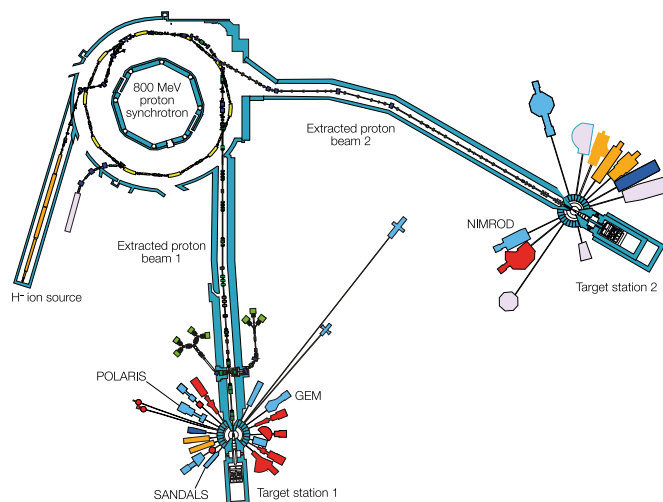


**Fig. 4.** Layout of the ISIS facility. Instruments are colour coded by type: light blue represents diffractometers, including PDF instruments; red represents spectrometers for inelastic scattering; orange represents reflectometers for studies of surfaces and planar interfaces; dark blue represents small-angle scattering instruments; green represents the muon instruments; and pink represents the rest, including irradiation and imaging instruments. The four PDF instruments discussed in the text are identified by name. The figure is used by permission of ISIS/STFC. (For interpretation of the references to colour in this figure legend, the reader is referred to the Web version of this article.)



**Fig. 5.** Photograph of one side of the ISIS pulsed spallation source. The light-blue circular enclosure contains the spallation target, with the proton beam coming from left to right. The motors on the top of the target enclosure control the shutters for the various beams. Most instruments are hidden below the floor, but the red enclosure gives access to the top of the POLARIS diffractometer. Photograph by MTD. (For interpretation of the references to colour in this figure legend, the reader is referred to the Web version of this article.)

the construction of the second target station.<sup>9</sup> The neutron pulse rate is half that of ISIS, at 25 pulses per second. It is anticipated that CSNS will eventually support 20 instruments, one of which is a dedicated PDF instrument, known as MPI (Multi-Physics Instrument) [89,90], and which has recently begun operation. CSNS also has the General Purpose Powder Diffractometer (GPPD) [91], with design characteristics which, we believe, will also be suitable for PDF measurements. Both MPI and GPPD are designed according to the principles behind the GEM and POLARIS instruments at ISIS. Unfortunately there are no plans for an instrument optimised for the study of light elements, namely one that follows the design characteristics of SANDALS and NIMROD at ISIS.

The design of the MPI instrument is shown in Fig. 6. The full design of

<sup>8</sup> The GEM diffractometer replaced the earlier PDF instrument LAD [27], which was optimised for liquids and amorphous materials.

<sup>9</sup> It is envisaged that a second target station will eventually be built at CSNS.

the instrument consists of 7 banks of detectors covering a range of scattering angles from 3 to 170°. The design will give values of  $Q$  between 0.1 and 62 Å<sup>-1</sup>, with resolution  $\Delta Q/Q$  of 6% for Bank 2 (angles 12.5–17.6°) and 0.4% for Bank 7 (angles 157.5–170°). The highest resolution is achieved in part by using a long flight path from moderator to sample of 30 m. The detector banks in the full design specification will consist of a total of 564 linear position-sensitive <sup>3</sup>He detectors. The MPI began operation in January 2021.

The other two pulsed spallation neutron facilities, SNS in USA and JSNS in Japan, also have a single dedicated PDF instrument each, both of which are similar in style to GEM and POLARIS at ISIS. The dedicated PDF instruments at SNS and JSNS are NOMAD [101,102] and NOVA [104] respectively.

We note that at the time of writing, there is no plan to have a dedicated PDF instrument at the ESS. However, the DREAM and HEIMDAL diffractometers will reach both values of  $Q$  up to 25 Å<sup>-1</sup>, which will support some PDF measurements [100]. The DREAM diffractometer may have an advantage over HEIMDAL for PDF studies in that it will go to lower values of  $Q$ , 0.2 versus 0.5 Å<sup>-1</sup>.

### 3.2. Synchrotron radiation

This year, 2022, is the 75th anniversary of the experimental discovery of synchrotron radiation [108,109]. The first observation of synchrotron radiation within a laboratory was in a 70-MeV synchrotron at the General Electric Research Laboratory in Schenectady, New York, in April 1947. In fact, humans had been seeing synchrotron radiation from stars or galaxies for a few centuries, but only with the laboratory discovery was it understood that one important source of radiation from space is from acceleration of particles within large magnetic fields. Since that time, the importance of synchrotron radiation as a scientific tool has been recognised across the World, with more than 60 synchrotron and Free Electron Laser facilities now proving instruments for scientific research [105].

Over the decades synchrotron radiation light sources have increased in power considerably, with three generations of development, of which the second and third are devoted to materials research (diffraction, spectroscopy, etc). Initially radiation beams were taken from the bending magnets in the main electron storage ring, but subsequently insertion devices (two types, wigglers and undulators) are built into the main ring

to give enhanced acceleration of the electrons in order to improve the properties of the extracted beam considerably. Examples of third-generation synchrotron facilities [105] include the European ESRF in Grenoble, France (co-located with the ILL neutron facility), the Diamond Light Source in the UK (co-located with the ISIS spallation neutron source), the Advanced Photon Source (APS) and Advanced Light Source (ALS) in the USA (the APS was co-located with the IPNS until its closure), Super Photon Ring-8 GeV (SPring-8) and the Shanghai Synchrotron Radiation Facility (SSRF).

Many synchrotron facilities have dedicated beam-lines for PDF studies, as listed in Table 2. In truth many instruments at a synchrotron can be configured for PDF measurements, since all that is needed is a beam of small wavelength and an area detector that can measure to sufficiently high scattering angle (which can be achieved by placing the detector close enough to the sample). That said, one advantage of a dedicated PDF instrument is that it can act as a focus for interactions with users, as well as having dedicated staff who can be concerned primarily with optimisation of PDF measurements and data processing. Fig. 7 shows a close view of the main elements on the XPDF beam-line (I15-1) at the Diamond Light Source in the UK [110,111]. One of the benefits of its co-location with ISIS is that users who require both x-ray and neutron PDF data can apply for both using a single proposal.

The next generation of light sources will include free-electron lasers. Several of these are currently in operation, including the Linac Coherent Light Source (LCLS) in USA, and the European XFEL (Germany). Sources currently under construction include the High Energy Photon Source (HEPS) in Beijing, MAX IV in Sweden, and NSLS-II in USA. Free electron lasers tend to have higher wavelengths than in synchrotrons, so their value for PDF work is not yet demonstrated.

### 3.3. Laboratory x-ray sources for PDF measurements

Very briefly, we should point out that some vendors are now marketing laboratory x-ray PDF instruments. Typically these will have silver anodes (wavelength of 0.559 Å), giving a maximum value of  $Q$  of around 22 Å<sup>-1</sup>. This is not dissimilar to what can be achieved in a synchrotron PDF measurement. The x-ray optics and detectors are optimised for PDF studies, recognising that there is not the same need for high angular resolution as in a standard x-ray powder diffractometer.

There are advantages and disadvantages with a laboratory PDF

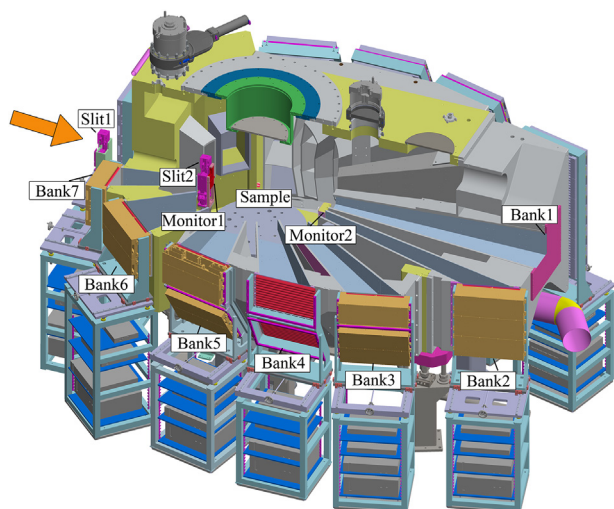


**Fig. 6.** Design of the MPI total scattering instrument at the CSNS facility [89, 90]. The beam enters the instrument from the left (orange arrow). The illustration shows the positions of the seven banks of detectors. (For interpretation of the references to colour in this figure legend, the reader is referred to the Web version of this article.)

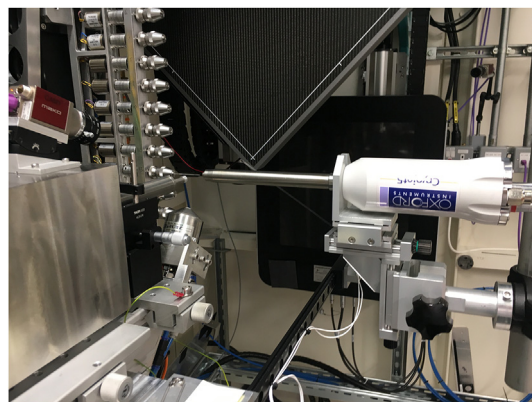


**Fig. 7.** Photograph of the XPDF (I15-1) instrument at the Diamond Light Source in the UK. The radiation enters from the left side of the photograph. The sample is contained within a silica glass capillary tube, which can be seen supported in an automatic sample changer. Temperature is controlled by a gas-stream cryojet which is seen in the centre of the photograph. At the rear are two area detectors, the closest one being used for measurement of the total scattering, and the other one at a further distance for a higher-resolution measurement of the Bragg scattering from crystalline materials. Photograph by MTD.



instrument compared with a synchrotron facility. The first comparison is that the intensity is so much weaker than available on a synchrotron source, such that whereas a synchrotron measurement will only take a few minutes, a measurement on a laboratory x-ray source will take many hours. So a laboratory PDF diffractometer cannot be used for a detailed study as a function of temperature or annealing time, for example.

The second comparison is that the laboratory PDF diffractometer is likely to be available for use at short notice, and particularly for single test runs. Experiments at a synchrotron typically need a proposal with review (and possible rejection), together with waiting time prior to scheduling. This means that synchrotron PDF experiments – like neutron PDF experiments – can only be reserved for planned studies, and do not give the flexibility that researchers often need. This is the major advantage for a research group to have access to a laboratory PDF instrument.

An example of a PDF machine, in the laboratory of one of the authors, is shown in Fig. 8. Confalonieri et al. [112] have presented a comparison of PDF measurements for a nanoparticle, showing little differences between data from a two instruments on a synchrotron radiation (ESRF) and a PANalytical Empyrean PDF diffractometer with a molybdenum anode. Such an instrument, with a silver anode, has been used in studies, for example, of amorphous zinc imidazolate [113], carbonates for CO<sub>2</sub> capture [114], and cadmium sulphide quantum dots and magic size clusters [43,115].

### 3.4. Brief comparison of different types of radiation for user applications

Whilst the focus of this review is on neutron scattering methods, the best choice of radiation from the three we have discussed will depend on the requirements of any particular study. In Table 3 we have summarised several points of comparison between the three types of radiation. As can be seen, neutron and x-ray total scattering data are complementary, and

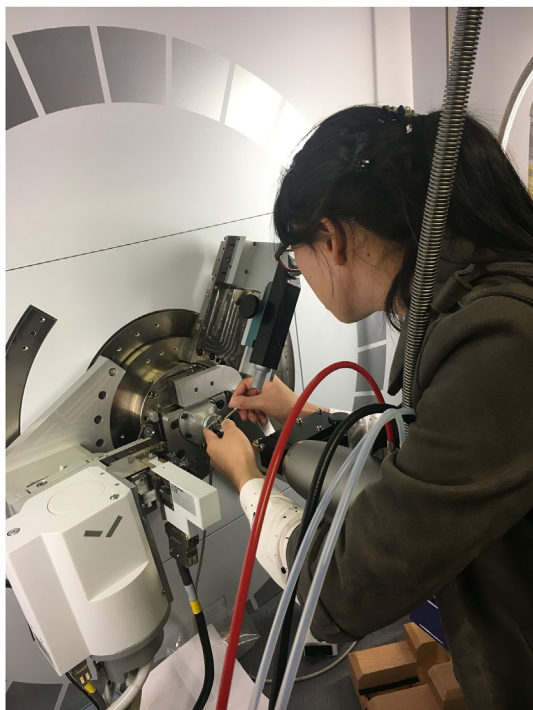


**Fig. 8.** A researcher aligning a sample on a PANalytical Empyrean PDF diffractometer. The photograph shows the x-ray source, but for the alignment procedure the detector has been replaced by optical telescope. The x-ray source and detector operate in a  $\theta$ - $2\theta$  mode in the vertical plane. The sample is contained within a silica capillary tube. Photograph by MTD.

the best case may be to perform similar measurements using both types of radiation in order to exploit this complementarity. However, when choosing the best type of radiation there are several factors to bear in mind, which we have given as explicit points of comparison in Table 3.

The range of values of  $Q$  are likely to extend to both lower and higher values for spallation neutron beams than for either synchrotron or laboratory x-ray sources. As we argued previously, higher values of  $Q_{\max}$  are preferable in extracting a PDF that has high resolution in  $r$  (Section 2.5). The minimum value of  $Q$  is important in establishing the low- $Q$  baseline in  $Qi(Q)$  prior to transformation to form  $D(r)$ . The function  $i(Q)$  has limiting value  $i(Q \rightarrow 0) = -\sum_m c_m b_m^2$  that extends over a range of values of  $Q$  [23]. Reaching this limiting value in the measurement is important in order to be able to extrapolate  $Qi(Q)$  down to  $Q = 0$  prior to Fourier transform. Identifying the limiting behaviour of  $Qi(Q)$  is also important in order to provide a reliable normalisation of the data.

Where synchrotron x-ray methods have a clear advantage over neutron and laboratory x-ray methods is with regards to intensity. Depending on the facility, a high-quality (in terms of statistical accuracy) measurement with reasonable  $Q$ -space resolution can take no longer than a few minutes, whereas a measurement at a neutron facility will take a few hours. A measurement with a laboratory source will likely take a day.<sup>10</sup> This means the PDF measurements with synchrotron radiation are much better for studies where many data sets are required, such as over a wide range of temperatures with small increments between different measurements. Short running times also enable kinetic studies for systems with time constants of the order of an hour or so. On the other hand, a typical neutron total scattering measurement with quality suitable for quantitative analysis may only be given sufficient beam time for a small number of state points (such as temperature). The example of our measurements of negative thermal expansion in ScF<sub>3</sub> [20] that we have cited above (Section 2.3) and will discuss in more detail below (Section 7.2) is a case in point.

We are stressing in this article (see for example Section 6) that the quality of neutron total scattering data to give high-quality PDFs must not be compromised by considerations such as trying to increase the number of measurements by reducing measuring time, or by attempting to perform experiments with low sample volumes.

The resolution in the measurement, what we call “ $Q$ -space resolution”, may not immediately strike the researcher as important. The main effect on the PDF of limited  $Q$ -space resolution is to attenuate the PDF at higher values of  $r$ .<sup>11</sup> One application where an uncharacterised  $Q$ -space resolution can lead to difficulties is in the study of the PDF of a nanoparticle. In this case the finite size of the nanoparticle also leads to an attenuation of the PDF at higher- $r$ . In order to obtain a good estimate of the size of the nanoparticle it is necessary to have a good characterisation of the  $Q$ -space resolution in order to disentangle the two effects.

Where high resolution is important is for when the Bragg scattering needs to be extracted from the total scattering measurement for separate contribution to the quantitative analysis, as in the use of the Reverse Monte Carlo method (Section 5.4) for the study of disordered crystalline materials. This is where neutron and synchrotron x-ray methods have a very clear difference. A modern neutron total scattering instrument will

<sup>10</sup> Although it is tempting to hope that the measurement throughput from a laboratory total scattering instrument can be 2 or 3 times higher, it is important to not sacrifice quality, particularly at higher values of  $Q$  where the scattering signal is weak. Given that laboratories typically only offer unrestricted access for researchers for perhaps 10 h a day at most, one of the authors (MTD) concluded with his own instrument (Fig. 8) that whole-day measurements were not only better for accuracy but also for the well-being of the researchers.

<sup>11</sup> There is a convolution argument; the convolution of data with a resolution function in  $Q$ -space leads to multiplication of the PDF by the Fourier transform of the experimental resolution function in  $r$ -space. If the resolution leads to only small broadening of the features of the scattering function in  $Q$ -space, the Fourier transform will vary only slowly in  $r$ -space. This effect can be accounted for in the analysis of the PDF, for example in the real-space fitting performed by programs such as PDFfit [116].

**Table 3**

Practical comparison of radiation sources for total scattering/PDF measurements.

	Spallation neutron beams	Synchrotron x-ray beams	Laboratory x-ray beams
Maximum $Q$	Measurements can be obtained up to $Q = 50 \text{ \AA}^{-1}$ . Beyond this limit, signal intensities are typically too low and derived values of $Q_i(Q)$ are too noisy.	Maximum $Q$ of around $25 \text{ \AA}^{-1}$ or lower, depending on wavelength and experimental configuration.	Maximum $Q$ of around $22 \text{ \AA}^{-1}$ with Ag $K\alpha$ radiation ( $\lambda = 0.56 \text{ \AA}$ ), or $17 \text{ \AA}^{-1}$ with Mo $K\alpha$ radiation ( $\lambda = 0.71 \text{ \AA}$ ).
Minimum $Q$	Can be quite low, depending on detector configuration: $0.02 \text{ \AA}^{-1}$ on NIMROD [99], and $0.04 \text{ \AA}^{-1}$ on GEM [28] and NOMAD [102].	Higher than for neutrons, because of the small range of scattering angles. Typical values may be around $0.5 \text{ \AA}^{-1}$ , but may be as high as $1 \text{ \AA}^{-1}$ in unfavourable cases.	Similar to synchrotron radiation.
Beam intensity	Depending on the facility, measurements may take between 2 and 8 h. Shorter runs will lead to lower statistical accuracy of $Q_i(Q)$ at higher $Q$ . Users are recommended to have samples of $\text{cm}^3$ volume.	Incident beam on the sample has much higher intensity than other sources, allowing high-quality measurements of the PDF to be obtained in minutes. This enables many measurements can be obtained in a single study, including for kinetic PDF measurements. Samples are much smaller than for neutron scattering experiments.	This is the weakest of the three sources. Whilst measurements can be performed in a few hours, for higher statistical accuracy (and for the practical reason to avoid dead time at night) it is better to use this source for one measurement per day.
$Q$ -space resolution	Depends on detector angle; lowest $\Delta Q/Q$ for the back-scattering detectors is around 0.35% on GEM [28] and 0.8% on NOMAD [102] as typical values.	Will be lower (higher $\Delta Q/Q$ ) than for neutrons because the scattering is always with forward angles.	Depends on instrument setting, but is unlikely to be better than for synchrotron radiation given that high resolution will lead to lower intensity.
Scattering factor	Neutron scattering length, which is independent of $Q$ . Sensitive to light elements, with different scattering for hydrogen and deuterium. Sensitive to magnetic atoms.	Proportional to atomic number, hence less sensitive to light elements. Decreases with increasing $Q$ , meaning that scattering intensity is lower at higher $Q$ and hence effectively limiting the practical maximum value of $Q$ . Prevents a pure PDF being extracted for materials with more than one element.	As for synchrotron radiation.
Availability	Relatively few neutron sources with capabilities for measuring PDFs	Most advanced countries have one or more synchrotrons, and many have dedicated instruments or instruments on which PDF measurements can be accommodated	These instruments have similar costs to standard powder diffractometers and are becoming increasingly common within the university community.

have detectors at all scattering angles (see Fig. 6 for an example), whereas a typical synchrotron PDF instrument will have scattering only in the forward direction (see Fig. 7 for an example). The scattering angle will have a contribution to the  $Q$ -space resolution that varies as  $\cot(\phi/2)$ , where  $\phi$  is the scattering angle. This will fall to zero as  $\phi \rightarrow 180^\circ$ , which is why diffractometers at spallation neutron sources have significant arrays of detectors at high scattering angle.<sup>12</sup> A diffractometer at a modern spallation neutron facility that can be used for both total scattering and powder diffraction measurements, such as GEM [36] and POLARIS [93] at ISIS, will have good resolution even at  $\phi = 90^\circ$ , and will be able to collect high-quality Bragg diffraction data in addition to total scattering data. Many synchrotron x-ray instruments optimised for total scattering measurements will not match the  $Q$ -space resolution of instruments optimised for powder Bragg diffraction at the same facility. The XPDF instrument at Diamond [111] (Fig. 7) has a separate detector for measurement of the Bragg diffraction pattern with a greater distance from the sample than that of the detector for collecting the total scattering data, but the quality of the Bragg diffraction data is not comparable with that of the main powder diffractometer at the same facility.

These factors are technical, but the final consideration here is also concerned with the scientific questions faced by a researcher. This consideration relates to the origin of the scattering, which is from the neutron-nucleus interaction in the case of neutron scattering, and from the electromagnetic interaction between photons and electrons in the case of x-ray scattering. In the latter case, the scattering scales as the number of electrons in the atom (usually close to the atomic number), and decreases with  $Q$  in a way that reflects the Fourier transform of the atomic electron density. There are two technical points regarding this

effect. The first is that the decrease in the x-ray scattering factor attenuates the scattering signal at high  $Q$ , which provides a practical limit to the maximum value of  $Q$  that can be achieved in an x-ray total scattering measurement (but this is offset to some extent for synchrotron x-ray radiation by the high intensity leading to low statistical noise). The second is a point that will be discussed in more detail in Section 4.2 regarding the deconvolution of the atom size from the PDF. In practice these two factors need not limit quantitative analysis of x-ray PDF data, but users need to be aware of the issues.

The scientific factor concerns the fact that the contrast in scattering between different elements is quite different in neutron and x-ray scattering. This difference can be exploited by performing complementary measurements using both sources, as will be seen in two of the case studies described later (Sections 7.3 and 7.5). The Appendix (Section 10) contains a more-detailed discussion of the contrast between neutron scattering lengths for different elements (Section 10.1 and Fig. 20), a discussion of the special case of hydrogen (Section 10.2), and a discussion of neutron absorption (Section 10.3). The researcher wishing to measure the PDF of a given material is advised to consider carefully the issue of elemental contrast in both neutron and x-ray scattering before embarking on a detailed study.

We can give one example to illustrate the point, namely a study of a material containing hydrogen. Light and heavy hydrogen,  $^1\text{H}$  and  $^2\text{H}$  (deuterium) respectively, have very different interactions with neutron beams. Light H has a very high incoherent cross section, and a negative scattering length. The first property is a potential problem, whereas the second gives very high contrast with other elements. Deuterium has much lower incoherent scattering and is often to be preferred in a neutron scattering experiment. However, there are many systems for which deuteration is extremely difficult, and if the locations of the hydrogen atoms are not interesting it may be preferable to perform an x-ray PDF experiment where problems of incoherent scattering do not occur. On the other hand, due to hydrogen having the lowest atomic number, it is virtually invisible in x-ray scattering experiments, so if the

<sup>12</sup> There is another contribution to  $\Delta Q/Q$  from the uncertainty of the neutron flight path  $L$ , that scales as  $\Delta L/L$ , where  $\Delta L$  arises from the size of the neutron moderator. This effect is reduced by having long flight path between the source and sample.



location of the hydrogen atom is important and deuteration is difficult, then a neutron scattering experiment is still possible. As will be discussed below (Section 4.1), for light elements specialised instruments such as SANDALS [97] and NIMROD [98,99] at ISIS, where the detectors are in the forward direction, are the most suitable instruments. The difference in scattering between light hydrogen and deuterium can be exploited, as described in two of our later case studies (Sections 7.1 and 7.4). Mixtures of light H, with its negative scattering length, and deuterium can give effective coherent scattering lengths that span the two limits, including the average of zero. This can be exploited to give contrast between the two end cases and between H/D and the other elements in the system. This is simply not possible with x-ray scattering.

Finally we comment that it is currently the case that there are many more synchrotron facilities than spallation neutron facilities. Hence there are many more instruments at synchrotron facilities than at neutron facilities that are dedicated to, or capable of being used for, PDF measurements. Availability of access to facilities may prove to be the decisive factor when planning a new study.

#### 4. Brief discussion of data treatment

##### 4.1. Neutron total scattering

One very practical question facing users of the PDF method is how to go from the raw scattering data to the PDF. There are many publications and software manuals that describe this task in more detail than we can manage here, but for completeness we give a brief overview of the steps that are required. Because this paper is written for a journal mostly interested in nuclear processes, we will restrict our discussion to the processing of neutron scattering data. Many of the issues will apply directly to x-ray studies, and we will indicate some extensions for the case of x-rays. In any case, we do not wish to deal with fine detail here beyond the overview and principles. More extensive details how processing neutron and x-ray scattering data are given in a number of technical papers [22,117–119].

##### 4.1.1. Data corrections

A neutron measurement is not performed in an isolated environment. Instead, the incident and scattered neutron beams will pass through the walls of the sample environment (equipment to maintain a chosen temperature), and the walls of the sample container (usually a cylindrical can of thin walls made of vanadium<sup>13</sup>). These will give rise to both sources of scattering and of attenuation of the beam. In spite of best efforts to collimate the incoming neutron beam and to shield the walls of the container with absorbing material, there will also be additional scattering from the instrument itself (note that modern neutron diffractometers at spallation sources are often designed with a vacuum inside the sample tank in order to reduce scattering from air).

A typical neutron scattering experiment will begin with a measurement of an empty instrument in order to obtain an estimate of the scattering from within the instrument, a measurement of the empty sample environment equipment (usually a furnace, cryostat or refrigerator), and a measurement of the sample environment equipment containing an empty

sample container (thin-walled vanadium can).<sup>14</sup> To get a sense of what is involved, we consider the set of equations that are involved in the data corrections. Following Howe et al. [117] we can consider the measurement  $I'$  and the actual scattering  $I$  for different components, namely from the sample  $S$ , sample container  $C$ , sample environment equipment  $E$ , and background from the instrument  $B$ . We assume that for the background we have  $I_B = I'_B$ , where the subscript  $B$  denotes scattering from the background (mostly from the walls of the empty instrument, assuming that the instrument is evacuated). We now consider the measurement taken with an empty sample environment,

$$I'_E = \alpha_{E,E}^E I_E + I_B \quad (22)$$

where  $I'_E$  and  $I_E$  are, respectively, the measured and unattenuated scattering from the sample environment, and the coefficient  $\alpha_{E,E}^E$  represents the effect of attenuation of the scattering from the sample environment by the sample environment. The measurement of scattering from an empty container inside the sample environment equipment is then written as

$$I'_C = \alpha_{C,E}^C I_C + \alpha_{C,E}^E I_E + I_B \quad (23)$$

Here  $I_C$  is the unattenuated scattering from the sample container,  $\alpha_{C,E}^E$  represents the effect of attenuation of scattering from the sample environment by both the sample environment and sample container, and  $\alpha_{C,E}^C$  represents the effect of attenuation of scattering from the sample container by both the sample environment and sample container.

Finally we have a corresponding equation for the measured scattering from the sample,  $I'_S$ :

$$I'_S = \alpha_{S,C,E}^S I_S + \alpha_{S,C,E}^C I_C + \alpha_{S,C,E}^E I_E + I_B \quad (24)$$

where  $I_S$  is the unattenuated scattering from the sample – the quantity that is the ultimate goal of the experiment – and the coefficients  $\alpha_{S,C,E}^S$  etc, that account for attenuation of the different scattering signals by the sample, container and sample environment, have definitions that follow as in the previous equations.

It is assumed that coefficients  $\alpha$  will be proportional to the neutron wavelength  $\lambda$  following the famous  $1/\text{velocity}$  law, which is a good approximation except for when the neutron energy is close to that for resonance absorption of one of the nuclei. These coefficients can be calculated from the known absorption coefficients of the constituent materials and their known geometry.

It follows that a measurement of  $I'_E$ , combined with the measurement of  $I'_B$ , can yield the value of  $I_E$  from equation (22). From the values of  $I_B$  and  $I_E$  it is then possible to determine a value of  $I_C$  from a measurement of  $I'_C$  using equation (23). Ultimately the required value of  $I_S$  can be determined from a measurement of  $I'_S$  via equation (24), with attention coefficients obtained from the known properties of the atomic components of the sample.

In many cases it is sufficient to be able to perform measurements of  $I'_B$ ,  $I'_E$  and  $I'_C$  at ambient temperature and use them for measurements at all temperatures, but there may be cases where these measurements need to be repeated for each temperature used in the scientific study. These measurements can then be combined to give good estimates of the scattering from and attenuation due to the various components in the experimental measurements in order to extract the pure signal of the total scattering from the sample [22,122]. Within this process account is also taken of absorption of the neutron beam by the sample, using an estimate of the powder density of the sample together with known elemental absorption cross sections and any incoherent

<sup>13</sup> Vanadium is frequently used because the cross section for coherent scattering of neutrons is virtually zero, so the Bragg peaks will be extremely weak and most of the scattering is incoherent. Vanadium also has a relatively weak neutron absorbance [120,121], and is a material that usually performs well at high temperatures.

<sup>14</sup> Whilst these measurements are time consuming, they need not take as long as measurements of the sample. The main requirement is that the statistical errors on the measurements should be comparable to – that is, not larger than, but not necessarily significantly smaller than – the statistical errors from measurements of the sample. Since scattering from the components of the experiment will ideally be much weaker than scattering from the sample, the corresponding statistical errors will be much smaller and thus measurement times can be shorter.

scattering<sup>15</sup> [120,121].

#### 4.1.2. Data normalisation

A neutron total scattering experiment also requires absolute normalisation. This is achieved by measurement of a cylindrical rod of vanadium of the same diameter as the sample can. All modern instruments contain many detectors, and thus this measurement provides a calibration of each detector against each other. Furthermore, since the cross section for incoherent scattering from vanadium is well known, it also gives the absolute scale for the measurement and hence an absolute rather than relative normalisation of all data [22].

At this stage, for data obtained on a spallation neutron source, the data are presented as a function of flight time. Assuming elastic scattering, if the flight time is represented as  $t$  and the total distance from source to detector via the sample is  $L$ , the velocity of the neutron is given as  $v = L/t$ . This gives the momentum  $p = mv = mL/t$ . The de Broglie wavelength,  $\lambda$ , is obtained from the momentum as  $p = h/\lambda$ , where  $h$  is Planck's constant. We also have the relationship for elastic scattering

$$Q = 4\pi \sin(\phi/2)/\lambda \quad (25)$$

where  $\phi$  is the scattering angle for any given detector as defined previously. It thus follows that  $Q = 4\pi mL \sin(\phi/2)/ht$ . It is common at this stage to convert the data from a function of  $t$  into a function of  $Q$ .

It is at this stage that the effects of multiple scattering, mostly from within the sample, are removed from the data, typically using standard formulae based on the sample density. It is assumed that the sample container is sufficiently thin to not contribute significantly to multiple scattering processes.

With normalised data, it is then possible to subtract the self-scattering term (equation (9)) to obtain the scattering function  $i(Q)$  through equation (11). It is from  $Qi(Q)$  that the PDF  $D(r)$  can be obtained via equation (16), but before this stage we need to take account of the effects of inelastic processes, which we briefly now discuss.

#### 4.1.3. Corrections for inelastic effects

The biggest challenge for analysis of neutron total scattering measurements is taking account of inelastic effects, namely where there is a change of neutron energy during the scattering process. In a total scattering experiment, as in a standard diffraction experiment, we do not measure the energies of the incoming and scattered beams. In a measurement with a fixed incoming wavelength, as in an instrument at a reactor neutron source using a beam that is reflected from a monochromator crystal, the scattering vector is 'determined' from equation (25). If there is a change in wavelength after scattering, this determination of  $Q$  is no longer correct. In the case of a pulsed white beam of radiation, as at a short-pulse spallation neutron source, the measurement is made of the scattering angle and flight time, from which  $Q$  can be determined as being proportional to the inverse of the neutron flight time (with proportionality constants related to parameters of the flight path from the origin of the beam to the sample and from the sample to detector, and taking account of the scattering angle). Not only do we need to account for the effects of the change of  $Q$ , but also the fact that the efficiency of the detector depends on energy, so the absolute intensity will be affected by change in energy of the scattered beam. A complete solution to this problem requires, in principle, a knowledge of the dynamical scattering function  $S(Q, \omega)$ , but as Howe et al. [117]

<sup>15</sup> In the presentation of the relevant equations in this paper we have avoided the complicating factor of accounting for both coherent and incoherent scattering, in order to enhance transparency for new users seeking a straightforward account of the methods. Where some elements have strong incoherent scattering – and hydrogen is likely to be the case most commonly encountered – users should make efforts to replace the element by an isotope without a significant incoherent cross section. In the case of hydrogen, deuterium should be used in sample synthesis wherever possible.

pointed out, if we knew  $S(Q, \omega)$  we would already know  $S(Q)$ !

There have been several attempts to address these problems, beginning with the work of Placzek – after whom the necessary corrections are named – in 1952 [123]. Further work on dealing with this problem has continued since then, as reviewed for example by Guarini [124], Salmon et al. [125], Fischer et al. [126] and Egami and Billinge [16], as developed further by Soper [127], and as presented in technical papers regarding data analysis [22,117,118]. The situation faced by the user is that these corrections are sufficiently complicated, and probably imprecisely known for the user's case, that the best action by the user is to follow the software commonly used on that instrument and the advice of the instrument scientist.

Users should be aware of two points. The *first* is that the major corrections are usually to the self-scattering term in the equations for  $S(Q)$ , and the *second* is that the corrections for inelastic effects are larger for lighter elements and for larger scattering angles. Thus for total scattering studies of light elements, it is better to use instruments optimised for scattering in the forward direction rather than in all directions, accepting the loss of  $Q$ -space resolution as a reasonable compromise to give better corrections for inelastic effects.<sup>16</sup> ISIS has commendably recognised this by building two instruments specifically to handle light elements, SANDALS [95–97] and NIMROD [98,99,107]. In view of the importance of light elements in modern life – hydrogen is a primary constituent of organic materials, including pharmaceuticals and plastics, and lithium is a primary constituent of battery materials<sup>17</sup> – it is to be hoped that plans for expansion of other spallation neutron sources will also include building new instruments optimised for total scattering studies of materials containing light elements.

We illustrate the problems of accounting for inelastic corrections by considering our own recent data in  $\text{ScF}_3$  [20], shown in Fig. 9. The data were obtained on the POLARIS diffractometer at ISIS [92,93], with detector banks across a wide range of scattering angles. The low-angle banks will measure the low- $Q$  part of the total scattering, and the higher-angle banks will measure the higher- $Q$  part of the total scattering, and with higher  $\Delta Q/Q$  resolution. The different resolution of the range of data banks with different scattering angles is evident in Fig. 9a, where, apart from the effects of resolution, the data appear to be highly consistent. Of more significance for this discussion are the data for higher values of  $Q$ , compared for different data banks in Fig. 9b. At higher values of  $Q$ , where we no longer can discern the Bragg peaks, the levels in the scattering function – after all corrections, including the Placzek corrections, had been applied – are seen to not have the same values, which can be attributed to inconsistencies in the corrections for the effects of inelastic scattering.

The differences in absolute values can be dealt with by software that

<sup>16</sup> Note that the resolution in  $Q$ -space in a spallation neutron source scales as  $\cot(\phi/2)$ , falling towards zero as  $\phi \rightarrow 360^\circ$ , which is why the highest-resolution diffraction measured on an instrument on a spallation neutron source is for the back-scattering detectors.

<sup>17</sup> It should be understood that lithium presents other difficulties for total scattering studies. First, it is really important to use samples enriched with the isotope  $^7\text{Li}$  rather than natural lithium, to avoid effects of absorption of neutrons by the isotope  $^6\text{Li}$ . Second, whilst the negative value of the neutron scattering length for  $^7\text{Li}$  gives a nice contrast to the positive scattering length of most other elements to be found in the battery materials, the product  $b_{\text{Li}}^2$  is much smaller than other products of scattering lengths. For example, in a recent PDF study of the ionic conductor  $\text{Li}_7\text{La}_3\text{Zr}_2\text{O}_{12}$  undertaken by MTD together with Haolai Tian (China Spallation Neutron Source) and Xiang Yang Kong (Shanghai Jiao Tong University) (manuscript in preparation) it was noticed that in spite of a relatively high elemental concentration of lithium – 29% – the product  $c_{\text{Li}}b_{\text{Li}}$  for Li–Li pairs is around 2% of the total  $\sum c_{\text{Li}}b_{\text{Li}}$  for the material, meaning there is insufficient sensitivity in  $D(r)$  (equations (14) and (18)) for the Li–Li  $g(r)$  to be determined, even when using the Reverse Monte Carlo method. The situation is even worse for x-ray total scattering, where the corresponding weighting is only 0.3%.

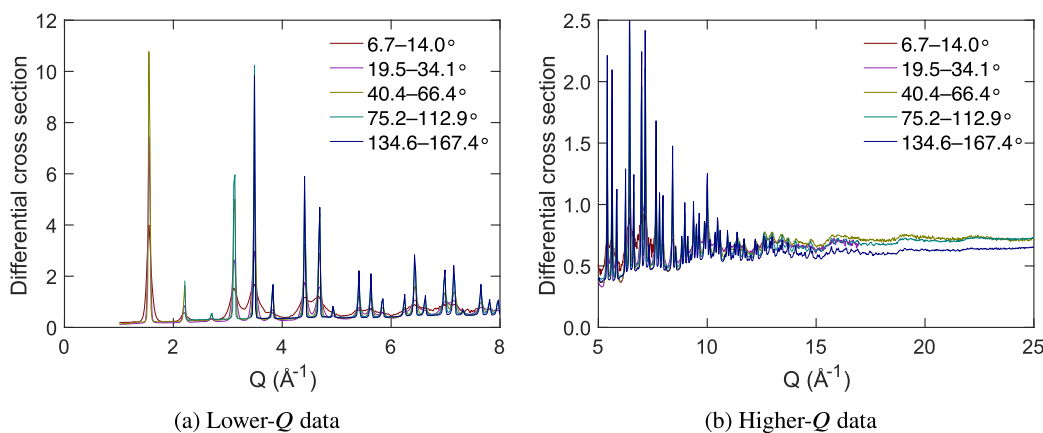


**Fig. 9.** Neutron total scattering data for crystalline  $\text{ScF}_3$ , obtained at a temperature of 500 K [20] on the POLARIS diffractometer at ISIS [92,93]. The legend indicates the angular ranges of different banks of detectors. The two plots show data over different ranges of  $Q$ . In (a) the effects of resolution are clearly seen, with data from the detectors at lower angles having much broader peaks. In (b) the effects of inelastic processes are seen in the data being corrected to different levels at higher values of  $Q$ .

merges the data from different banks, such as the GUDRUN software [118] used in this analysis, and one demonstration of this is the data from the same experiment shown in Fig. 2. However, we want to make several remarks from this example.

The *first* remark is that the extent of the differences between data from different banks of detectors seen in Fig. 9b is not untypical. Fluorine is a relatively light nucleus, but similar in nuclear mass to the very common element oxygen. Thus it is quite likely that similar differences will be seen in many oxide materials. *Secondly*, we have seen much worse cases, particularly for materials containing deuterium with measurements obtained on a similar diffractometer with scattering into detectors at high angles. *Thirdly*, when comparing data from different banks, we should focus on the higher- $Q$  data. If different banks are compared at lower values of  $Q$ , the fact that the scattering signal is stronger at lower  $Q$  (particularly if there are Bragg peaks) means that any differences in levels can be easily hidden from the eye. The consistency (albeit with different peak resolution) at lower values of  $Q$  can therefore be misleading. *Fourthly*, merging data from different banks of detectors is arbitrary to some extent, which is why we advocate in the next section (Section 5) that where possible the PDF should be analysed using quantitative modelling.

#### 4.1.4. User experience and user responsibility

The key message here is that analysis of total scattering data to eventually obtain the PDF is neither trivial nor entirely satisfactory. There are several levels of uncertainty and several potential pitfalls. In Section 6 we will make some further comments about this point, but here we want to stress one thing. Whilst it is quite reasonable that users cannot be expected to have the expertise accumulated by those whose research is focussed on the application of PDF methods, the user nevertheless has responsibility to check the quality of their data. In our opinion, it is scientifically reckless to take receipt of PDF data and automatically assume these are of suitable quality for further analysis. Instead, we would urge all users of PDF methods to do two things.

The *first* is to look critically at the diffraction data after all corrections have been made but before data from different banks of detectors have been merged. Are levels from different banks of detectors consistent (or can be made consistent), and is the statistical accuracy of data at higher values of  $Q$  good enough (this trivial point is often overlooked by users)?<sup>18</sup> Users may need to specifically ask for these data if a facility normally provides only the PDF.

*Secondly*, ensure data are on an absolute scale rather than on a normalised or arbitrary scale, and then compare the data with a PDF

obtained from model that you believe has the correct coordination numbers (this is easy for a crystal; such a model PDF can be generated by a number of methods, including the lattice dynamical calculation discussed in Section 2.6). The easiest thing is to perform an integration of the PDF to derive the function

$$n(r) = \int_0^r r' T(r') dr' \quad (26)$$

Plateau values of  $n(r)$  will correspond to the spatial intervals between subsequent shells of neighbours. If the PDF has proper normalisation and without spurious heights of peaks, the experimental data will have plateau values that match those of a model, even if the widths of the peaks in the PDF from the model do not match those in the PDF (comparing with a model has the advantage of removing the need for any calculations!). If the plateau values of  $n(r)$  do not match the model, the experimental PDF contains errors. Of course the match is unlikely to be perfect, not least in view of the issues we have discussed here, but whether the match is good enough must only be decided by the critical judgement of the user. An example of a reasonable match is shown in Fig. 10, where again we show data for  $\text{ScF}_3$  [20].

#### 4.1.5. Software

To conclude on a practical note, the two major software products for

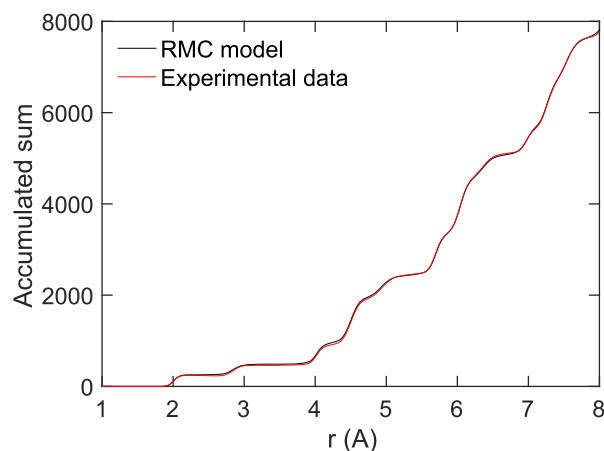


**Fig. 10.** Example of comparing the cumulative integral of the function  $rT(r)$  (equation (26)) for PDF data for  $\text{ScF}_3$  at 10 K (red curve, see Fig. 2) with the results from a reasonable model (black curve; in this case, the model was from the Reverse Monte Carlo model) [20]. The close agreement between the two curves shows that the integrated area of each peak in the PDF is reasonable. (For interpretation of the references to colour in this figure legend, the reader is referred to the Web version of this article.)

<sup>18</sup> Even more trivial, but easily overlooked, is the need for researchers to check that the scattering data are not contaminated by Bragg peaks from unexpected impurity phases.

analysis of neutron total scattering are GUDRUN [118] and PDFgetN [128,129]. Which software you use is likely to depend on the preferences of the support scientists at the neutron facility you use. It is, however, worth understanding that there are some differences between the two, and researchers should ensure that they collect the necessary correction data expected by both data reduction codes.

GUDRUN was developed at ISIS by Alan Soper [118], and it follows in the footsteps of several earlier efforts associated with the ISIS facility, including the ATLAS suite of tools [22], with some of the developments discussed separately by Howe et al. [117]. GUDRUN includes a number of later developments in understanding the treatment of total scattering data, including for the inelastic corrections for light elements [127]. The original PDFgetN software followed a similar approach, based in part on projects associated with data analysis at the LANSCE facility [128]. More recently Simon Billinge and Christopher Farrow argued in favour of using ad hoc data correction procedures, based on the general form of the relevant equations and knowing the limiting values of the important functions [130]. This approach was shown to be reliable and accurate through comparisons of treating data both with the more formal correction methods and the ad hoc method, and thus this approach is now adopted in the more recent PDFgetN3 software [129]. The principle difference regarding the primary outcome, namely a corrected scattering function and associated PDF, is that the ad hoc method does not yield an absolute normalisation. Billinge and Farrow argued [130] that when the data are fitted with a model atomic structure the absolute normalisation can be treated as a fitting variable and hence is not so important. However, the view of the current authors, as expressed elsewhere in this paper, is that that absolute normalisation at some stage is important as a test of data quality.

GUDRUN makes use of a method called the ‘top hat’ function to remove unknown sources of scattering from the scattering function based on the constraint that the PDF should be featureless at low distances [127]. This cleans up much of the low- $r$  noise in the extracted  $D(r)$  and removes the corresponding noise from the scattering function (typically with long period in  $Q$ ).

GUDRUN also includes the use of a more sophisticated form of the modification function presented in equation (21) [119,131]. This allows for a broadening of the peaks in the PDF that varies with  $r$ , in contrast to the constant broadening given by equation (21). It has been shown that the primary effect of this is to better suppress the effects of noise at higher values of  $Q$  in the scattering function [131].

One consideration for the user is that although some analysis methods, as discussed in the first three parts of Section 5, only make use of the PDF, other methods may require an accurate scattering function too. The Reverse Monte Carlo method, Section 5.4, is better performed using both total scattering data and corresponding pair distribution function, and the Empirical Potential Structure Refinement method, Section 5.5, only uses the total scattering data. The ability of software to generate both PDF and properly corrected and normalised scattering data is likely to be an important consideration for the researcher.

## 4.2. X-ray total scattering

The situation for x-ray total scattering has some advantages and some disadvantages compared to the situation for neutron total scattering. The primary advantage of x-ray total scattering is that the energy of the beam is so much higher than the excitations in the sample that there is no need for a Placzek correction, which is the major cause of uncertainty when extracting the PDF from neutron total scattering data.

Analysis of x-ray total scattering data has been discussed in great detail by Soper and Barney [119], and the reader is referred to their paper for more information than is appropriate here. Although a second advantage of x-ray over neutron total scattering methods is the absence of incoherent scattering, there are additional contributions to the measurement from both fluorescence and Compton scattering, which must be taken into account within the data processing.

What is often not fully appreciated is that the PDF obtained by x-ray total scattering for a material containing more than one element is not quite a true PDF. Central to the discussion in Section 2 is the idea that an atom can be defined as having a position at a point in space. Given that the size of an atomic nucleus is 4–5 orders of magnitude smaller than the wavelength of a neutron beam, neutron scattering is effectively from point particles as far as the precision of the measurement is concerned. If all atoms are at rest, the atomic density  $\rho(\mathbf{r})$  can be described as a set of Dirac  $\delta$ -functions at positions  $\mathbf{r}_j$ . The PDF actually corresponds to the convolution  $\rho(\mathbf{r}) \otimes \rho(-\mathbf{r})$ , and if all atoms are at rest the neutron PDF will be given by a set of  $\delta$ -functions at positions  $\mathbf{r} = \mathbf{r}_i - \mathbf{r}_j$  collapsed onto one dimension. In fact atoms are not at rest, so the peaks are convolved with a function describing the correlated motions of both atoms in a given pair (at large distances, the motions of any two atoms are no longer correlated so the peaks in the PDF are the convolution of the single-atom distribution function). In the case of x-ray total scattering, we need to think of an atom as a position of its centre (defined as for the case of neutron scattering as a  $\delta$ -function) convolved with the atomic electron density (since the x-rays are scattered by the electrons). Thus the peaks in the x-ray PDF will be the  $\delta$ -functions as in the neutron PDF convolved with a function describing the thermal motion and then convolved by the functions describing the electron densities of the two atoms. What this means in practice can be appreciated by considering the first peak in the PDF, which will correspond to the shortest ‘chemical bond’ in the material. Since in this case the outer electrons of both atoms will be touching, the peak in the x-ray PDF at position  $r = r_0$  will extend from  $r = 0$  to  $r = 2r_0$ . Clearly this first peak will overlap with the second and third peaks, and there is likely to be a large peak centred on  $r = 0$  extending to around  $r = r_0$  which will significantly overlap the low- $r$  tail of the first peak.<sup>19</sup>

The solution to this problem is relatively simple. The convolution with electron density in real space will correspond to multiplication by the Fourier transform of the electron density in  $Q$ -space. This is nothing other than the atomic x-ray scattering function  $f(Q)$ . Thus by dividing  $i(Q)$  – which in turn has the self scattering removed in  $Q$ -space using the sum of the products  $f_m(Q)f_n(Q)$  – by either  $\langle f^2(Q) \rangle$  or  $\langle f(Q) \rangle^2$  we can approximately perform the deconvolution of the atomic electronic density out of the x-ray PDF. Because different parts of the x-ray PDF will depend on different pairs of atoms, and because we do not have access to the set of partial PDFs  $g_{mn}(r)$ , this procedure is necessarily approximate. This is why we are free to choose from either of the two scalings we have given. But it also means that the x-ray PDF is not quite as quantitative in a peak-by-peak way as the neutron PDF. Any quantitative analysis of the x-ray PDF will need to take this point into account.

As discussed in the previous part, there are two major software products for the treatment of x-ray total scattering data, coming from the same two groups as before. These are GUDRUNX [118,119] and PDFgetX [132]. Again, which software you use will depend on your local support scientists. Similarly, which additional correction measurements made may depend on the local custom. For example, measurement of an empty instrument is essential for GUDRUNX but not for PDFgetX.

## 5. Analysis of the PDF

### 5.1. Fingerprint-type analysis

Fingerprint analysis is common in many sciences. An unknown sample will be composed of one or more constituents, and the task is to identify these constituents by comparing experimental data with a database of results for many pure phases. There may be many different types of experimental ‘spectra’ that can be used to identify constituent parts, such as vibrational spectra or x-ray powder diffraction patterns. The task is to match the spectrum from the sample with entries in a

<sup>19</sup> This peak is a rigorous  $\delta$ -function in the neutron PDF and thus was easy to exclude by the removal of the self-scattering term.



database containing the spectra of pure materials. If vibrational spectroscopy is used, it can be possible to identify specific structural elements such as stretching of a particular type of chemical bond or flexing of a bond angle. If x-ray powder diffraction is used, the angles and intensities of sharp Bragg peaks can be used to identify specific materials within the sample.

It is possible to use the PDF of a sample as a type of fingerprint. The main caveat is that the PDF only contains a few sharp peaks, and so phase matching of the sort done using Bragg scattering may be much harder. On the other hand, fingerprinting methods have the potential to provide unique information in studies of the transformation of a material, because they can show the presence of new chemical bonds. Thus in a chemical reaction, the PDF may reveal the presence of specific intermediate states from the appearance of new peaks with characteristic bond lengths.

## 5.2. Peak fitting

In many cases the first 2–3 peaks in a PDF are in the region of the PDF where the baseline can be seen clearly, and are not overlapping other peaks. These peaks can be identified with specific chemical bonds or close atomic contacts. Typically the peaks in  $T(r)$  can be fitted by Gaussians, giving numerical values for mean position, overall peak area, and peak width. The mean position can identify specific chemical bonds and connectivities.

One example is a study of the PDF of amorphous silica [21]. From the first peak in the PDF it was found that the Si–O bond has a mean distance of 1.608(4) Å, and the O–O distance is 2.626(6) Å. Since the O–O distance is equal to  $\sqrt{8/3}$  times the Si–O distance, this configuration appears to represent the existence of SiO<sub>4</sub> tetrahedra as in crystalline forms of silica. The third peak represents the Si–Si distance, at distance of 3.077 Å [133]. Combined with the Si–O distance, this value implies that the mean Si–O–Si angle is 146°. This is consistent with subsequent structural studies of amorphous silica [32].

This example demonstrates how analysis of the positions of the first few peaks in the PDF can give information about the geometry of the local atomic structure, but this picture can be confirmed (or refuted) by analysis of the integrated intensities of the peaks. From the definition of the function  $g_{mn}(r)$ , if the peak exists between limits  $r_0 \pm \Delta r$ , the number of neighbours will be equal to

$$\begin{aligned} N_{mn}(r_0) &= 4\pi\rho c_n \int_{r_0-\Delta r}^{r_0+\Delta r} r^2 g_{mn}(r) dr \\ &= \frac{4\pi\rho}{c_m b_m b_n} \int_{r_0-\Delta r}^{r_0+\Delta r} r T(r) dr \end{aligned} \quad (27)$$

The same study of silica showed that on average the Si atoms have 3.85(16) O neighbours, and each O atom has 5.94(23) O neighbours. These results are within error of the ideal values of 4 and 6 respectively for a network of connected SiO<sub>4</sub> tetrahedra.

Fitting to the peaks of the PDF relies on the accuracy of the first 2–3 peaks. Unfortunately, experience shows that these are the hardest peaks to obtain with accuracy from transformation of the total scattering data, in part because they are most susceptible to systematic errors (often unknown) in the scattering data, and because they are the peaks that are most susceptible to the effects of termination ripples. We want to stress that no researcher should ever assume that the PDF they have obtained from total scattering data are sufficiently reliable for peak-fitting analysis.

In this regard we cite a recent paper [134], studying the PDF of ScF<sub>3</sub> as a function of temperature, where the authors report the results of a peak-fitting exercise on the first three peaks. The results show a variation of peak intensity with temperature for each peak, and for one peak the intensity decreases by as much as 50%. Since this is a crystalline material,

with no diffusional motions, the coordination numbers cannot change with temperature. The authors “explained” these changes of peak intensity using phrases such as “loss of the coherent fluorine contribution”. Our own data [20], shown in Fig. 2 does not show the same effect. Application of Occam’s razor suggests to us that the cause of unexpected results from an analysis of PDF data is more likely to be from systematic errors in the data rather than from some “new physics”. In this regard we note that the PDF data these authors were working with were not placed on an absolute scale or on a normalised scale, so the peak intensities could not be converted into coordination numbers. Conversion to an absolute scale would have given a clearer check of the plausibility of the values of the peak integrations.

Because it is possible that the first peaks in the PDF are vulnerable to the effects of unknown systematic errors, we consider that it is essential whenever possible to test a PDF by using any of the methods discussed in the next parts of this section. This is what is displayed in Fig. 2, where the experimental PDF is compared with the results of a Reverse Monte Carlo simulation (discussed below). Because the simulation model is for a crystal, it necessarily has fixed values for all coordination numbers and hence for peak intensities. If the experiment and simulation disagree regarding the intensities of peaks, it is most probably the data that are at fault. In this case, the simulation method is able to give a direct indication of the quality of the PDF. Of course, for a fluid or glass we do not have the same opportunity, but the experience with crystalline materials should warn researchers against a simple trust of the data. Instead, we urge a critical analysis of the raw data, as was exemplified in early work on amorphous silica and other examples [21,25,26,135].

## 5.3. Fitting the whole PDF

One of the great successes of powder diffraction, whether with neutrons or x-rays, is the Rietveld method. In this approach, the whole powder diffraction pattern is fitted with a model that includes the details of the crystal structure (lattice parameters, atomic coordinates, atomic displacement parameters, site occupancies), parameters for the functions describing the shapes of the diffraction peaks (both intrinsic to the instrument, including the instrument resolution, and to the sample, including particle size effects, and internal stresses), and functions to describe the background [136]. This has inspired the development of methods to fit the whole PDF in a similar way, fitting the details of a crystal structure which determine the positions and intensities of the peaks in the PDF, parameters describing the widths of the PDF peaks, together with some parameters associated with the sample (such as particle size) and instrument (such as the effects from maximum Q) [116].

Merely fitting a known crystal structure to a PDF has limited value, particularly if the crystal structure is ordered. In such cases normal Rietveld analysis from powder diffraction data will be both faster in terms of data collection and more accurate in the analysis. However, there are two clear cases where there is considerable value in fitting a model to the PDF.

The first case is when the local structure is different from the average crystal structure. In that case it is possible to fit the short-distance part of the PDF with one model and the longer-distance part with an average crystal structure, showing how the local structure deviates from the average structure. ScF<sub>3</sub> provides a clear example of this, where the Sc–F distance in the PDF will be longer than that deduced from the crystal structure [20,81].

One example using fitting to the neutron PDF is in the study of the Jahn-Teller-driven phase transition in LaMnO<sub>3</sub> [137] and the doped material La<sub>1-x</sub>Ca<sub>x</sub>MnO<sub>3</sub> [138]. The Jahn-Teller effect causes distortion of the MnO<sub>6</sub> octahedra, giving rise to different bond lengths that can be seen in diffraction results, with the crystal having orthorhombic symmetry. At  $T_{JT} \sim 750$  K there is disordering of these distortions with a first-order transition, and although the crystal retains the same symmetry it is much closer to the parent cubic phase with near-perfect octahedra. In

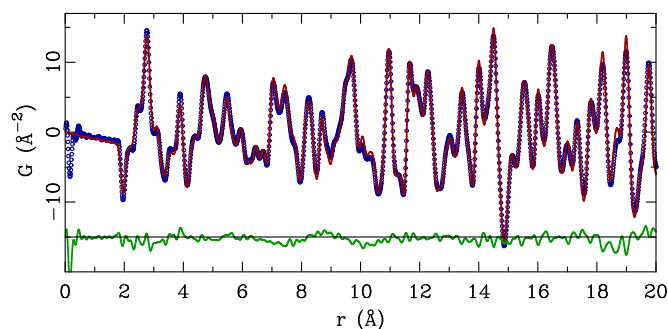


**Fig. 11.** Fitted PDF of  $\text{La}_{1-x}\text{Ca}_x\text{MnO}_3$ , with  $x = 0.22$  [138]. The circles represent the data, and the red curve is the calculated PDF. The green curve shows the difference between model and data. The authors have correctly shown the data down to  $r = 0$ , as recommended by Adrian Wright [21] and as discussed in Section 2.3. Note that what these authors have called  $G(r)$  is what we and others call  $D(r)$  [23]; see our discussion of nomenclature in Section 2.4. (For interpretation of the references to colour in this figure legend, the reader is referred to the Web version of this article.)

order to model the PDF data, the analysis fitted different models to the PDF over different ranges of distance. The longer-distance part of the PDF reflected the long-range atom–atom correlations in the average structure. However, at short distances the Jahn-Teller distortions are clearly seen in the local structure but without long-range ordering, and thus the short-range part of the PDF was fitted with a model that represented clustering of local distortions. Clusters of short-range ordering of the distorted  $\text{MnO}_6$  octahedra were found to extend in size to the distance of 4 octahedra, and to temperatures significantly above  $T_{JT}$ . The effects of substitution of some lanthanum cations by calcium showed a changing size of the Jahn-Teller distortion with composition. One example of the PDF fitting in the latter case [138] is shown in Fig. 11, illustrating the quality of fit that can be achieved.

The second important use in fitting the whole PDF is in the study of nanoscale clusters. On one hand, this approach can confirm any link between the atomic structure of the cluster to that of known crystal phases. On the other hand, it is possible to extract a good estimate of the size of the nanoscale cluster directly from the fitting procedure [139].

The main software for fitting a crystal structure to the PDF has for a long time been PDFfit [116,140], which is available as part of the PDFgui suite of software [116,141]. The software is developed using Python, and the user will install a basic layer of this language to enable PDFfit to run. The software is accessed through a graphical user interface. More recent versions of the crystallographic software Topas [142] now offer the opportunity to fit an atomic structure to a PDF. Topas is a commercial product. It offers the user the capability of creating custom scripts rather than providing all functionality through a user interface. Communities of researchers, typically based around a facility and its users, may develop scripts that can provide a wide range of functionalities within Topas.

Recently a new approach to the fitting of the PDF for a crystalline material has been developed based on fitting patterns of atomic displacements associated with symmetry-adapted normal modes [143], rather than fitting a set of atomic positions. This has been tested on some materials showing negative thermal expansion [144,145], and on the ferroelectric  $\text{BaTiO}_3$  under pressure [146]. We understand that will be developed as a general user tool.

#### 5.4. The reverse Monte Carlo method

The objective of the *Reverse Monte Carlo* (RMC) method is to generate one or more large-scale atomic configurations that are consistent with the experimental data [147–150]. For fluids and amorphous materials, the data sets consist of total scattering data – neutron or x-ray – and

associated PDF data.<sup>20</sup> For the study of crystalline materials it has been found to be useful to include the Bragg diffraction data too, so that the RMC has data both about local structure and long-range average structure [122,151,152]. The simulation engine is the Monte Carlo method, selecting atoms for random displacements, with the move accepted or rejected according to whether the move improves or diminishes the agreement between experiment and calculated functions. In this sense the level of agreement, defined as a mean-square difference between experiment and calculation, plays the role of energy in a more conventional Monte Carlo simulation of condensed matter, with a standard probability test being used to determine whether to accept or reject moves that lessen the level of agreement.

One popular ‘complaint’ against the RMC method is that there are more variables than data points. In general, a system in this state has too much freedom, and experimental data can be accurately fitted without the model being realistic. An equally valid, but less-often mentioned, criticism concerns the fact that the PDF gives *average* quantities. Consider a simulation of a tetrahedral system where the average coordination number given by the first peak in the PDF is 4. Usually we assume that this average coordination number applies to all sites, whereas in truth this assumption is derived from chemical insights that are not contained within the data. Thus the Monte Carlo engine can equally well create sites of coordination numbers 3 and 5. For this reason, and in the light of the first criticism, it is often useful to add a number of constraints to the RMC simulation, such as minimum distances, penalty functions for the creation of local atomic clusters with ‘wrong’ coordination numbers, and effective short-range potential energy functions to give reasonable bond distances and angles. Of course, these are often more easily applied for RMC studies of crystalline materials.

The most significant drawback of the RMC method compared to fitting the PDF is the time required. Fitting a PDF can take seconds, whereas an RMC simulation will take from hours to days. On the other hand, the main advantage of the RMC simulation is that the use of a large configuration gives freedom from any constraints imposed by using a small configuration in the PDF fitting method. Thus it is possible to study high degrees of disorder.

One other criticism levelled at the RMC method is that as a method based on statistical mechanics it will naturally increase the degree of disorder. This criticism is not without merit, but in practice it may not be important. We are encouraged by the results of studies over a wide range of temperature, such as that of  $\text{ScF}_3$  [20] from which the data in Fig. 2 are obtained. On varying temperature, it is found that the variances of various fluctuations increase linearly with temperature, consistent with a solid for which the primary interactions are harmonic-like (including the case where anharmonic interactions lead to a renormalised harmonic model). Some results will be shown later in Section 7.2. This consistent behaviour found for independent data sets at different temperatures

<sup>20</sup> One technical point to note is that the PDF can only extend to a maximum distance,  $r_{\text{max}}$ , equal to half the shortest period distance in the configuration supercell, which often will be the shortest configuration dimension. The calculated scattering function to be used in the RMC, typically  $i(Q)$ , will be obtained from the Fourier transform of the  $D(r)$  obtained from the RMC configuration. Because  $r_{\text{max}}$  will be relatively small, perhaps around 25 Å, the Fourier transform to generate the calculated scattering function will show truncation ripples similar to those produced in the inverse transform to generate the PDF from experiment  $Q_i(Q)$  data available only for  $Q < Q_{\text{max}}$ . Thus within the RMC method the experimental scattering data will be convolved with a sinc function based on the size of  $r_{\text{max}}$  to enable accurate comparison between the calculated and experimental scattering function. Specifically this convolution is given by the equation

$$i(Q) = \frac{1}{\pi} \int i(Q') \frac{\sin(r_{\text{max}}(Q - Q')/2)}{Q - Q'} dQ'.$$

gives confidence that the RMC method is giving realistic atomic configurations.

Although the RMC method was initially developed as a tool to give better quantitative information about the atomic structures of fluids and glasses [147–150] – and indeed there are many successful applications of the RMC for these cases – it is our contention that disordered crystalline materials are actually the ‘sweet spot’ for the RMC method. For crystals we can explicitly include the Bragg scattering data in the data set along with the PDF and total scattering data. Whereas the PDF and total scattering data provide information about the local structure, the Bragg scattering data fitted by calculations of the crystallographic structure factor also give information to the RMC simulation about the average spatial atomic density. Through the indexing of diffraction peaks by the Miller indices, which reflect the three-dimensional lattice planes from which the Bragg peaks are diffracted, the use of the Bragg scattering data gives some three-dimensional information to the RMC simulation. Furthermore, the existence of the crystal structure imposes a number of constraints on the simulation, leaving the RMC method free to generate information about fluctuations from the average structure rather than finding an overall atomic structure from a situation with limited prior information.

As with any data-modelling tool, it is essential that the researcher applies some critical analysis to the results. This is perhaps more important with RMC modelling than for PDF fitting in one respect: the fact that there are pitfalls associated with the large number of variables in the modelling means that it is always essential that the models are checked for reasonable behaviour and consistency. All four of the modelling methods discussed in this section are highly susceptible to errors in the data, and as we stress several times in this article we strongly urge researchers to be aware of the quality of their data. In the case of fitting to the PDF, errors in the data are most likely to be reflected in significant differences between the experimental and calculated PDFs, but in the case of RMC errors in the data are likely to be fitted because of the large number of degrees of freedom if the weighting of the constraints is not sufficiently large.

The original RMC programs [153,154] have been superseded by two that are under continuous development. RMC++ is the natural successor software [155], and there have been several additional developments [156,157]. RMCprofile was developed independently from the original RMC program with the specific intention to have applications to crystalline materials by explicitly including the information contained within Bragg scattering data [152]. This too has benefitted from ongoing development.

### 5.5. Empirical Potential Structure Refinement method

The *Empirical Potential Structure Refinement* (EPSR) method is conceptually similar to the RMC method, using a Monte Carlo engine to drive a configuration of atoms towards best agreement with experimental data, but it makes much more use of interatomic potentials than does the RMC method [158–160]. There are two types of potential energy functions. One, the *reference potential*, includes a set of standard potentials suitable for the problem under study, and can include models from the wider scientific community that have been shown to be reliable for the system under study. The other is the *empirical potential*, which is a function that is adjusted within the EPSR simulation to help guide the atomic or molecular configuration to give results that are in best agreement with experimental data. The use of the empirical potential accounts for differences between the predictions of the reference potential and the experimental data.

Where the EPSR method has a distinct advantage over a more general RMC approach is for the study of molecular fluids [161]. This is a particularly challenging problem for data-driven simulations of highly disordered materials. The main problem with data-driven simulations is that there is nothing in the data per se that can directly match features in the data to specific aspects of the atomic structure. For example, in a fluid of a molecular hydrocarbon molecule, the data do not come labelled with

the information that the first two peaks in the PDF correspond to the C–H and C–C bonds respectively, and trying to label the peaks in the PDF of a fluid is practically impossible.<sup>21</sup> If the constraints of the simulation allow atoms to move far enough to give large changes in the structure, they can be re-arranged in any manner that may match the PDF data but with inappropriate bonds. Thus it is essential to provide some significant chemical knowledge to work in tandem with the data to guide the evolution of the simulation towards the a realistic configuration. The EPSR method achieves this through its significant use of realistic intramolecular and intermolecular potentials. The potentials guide the evolution of the simulation whilst ensuring that the molecules retain integrity, and ensuring that they are able to move during the simulation beyond merely fluctuating about the starting state. In this sense the EPSR method achieves the best of both worlds: it takes the advantages of simulation methods based on potentials with the drive towards generating configurations that are in good agreement with experiment.

Interestingly the EPSR method primarily uses the total scattering data and not the corresponding PDF. Indeed, the philosophy is that with best agreement with the total scattering, the PDF from the configuration is the best estimate of the true PDF. In our opinion this is not an unreasonable philosophy, and has the benefit that the PDF will be free of many of the artefacts identified in Section 4.1. In this sense, the EPSR model is exactly the opposite of PDF-fitting methods (Section 5.3).

The EPSR method is capable of giving information about quite complex systems. One example will be discussed in more detail in Section 7.4, which describes a study of a solution of *four* different molecules. In addition to being used to analyse data from complex fluids, the EPSR method has also been used for the challenging study of fluids (liquids and gases) in confinement within porous media [162,163], and for understanding the structures of micelles in solutions [164,165].

For a long time the main software for the EPSR method was an eponymously-named program written and maintained by Alan Soper [159]. More recently, Tristan Youngs has developed a new version called Dissolve [166], and Changli Ma et al. have developed a version called NeuDATool [167].

### 5.6. Comparison and guidance

It is worth comparing these different approaches in terms of which approach might be appropriate for different applications.

In truth the finger-print analysis may generally be more useful with synchrotron radiation, simply because the much shorter measurement times make synchrotron radiation better for studying processes that change with time. That said, there is a sense in which our example described in Section 7.1 can be said to be a finger-print analysis, where we compared calculated and measured total scattering data to assess the ‘correctness’ of a proposed model, where fitting turned out to be too difficult.

Peak fitting is a natural first step in quantitative analysis, but as we stressed it needs the highest quality data. It makes most sense to fit the  $T(r)$  function, but this means that the extracted  $D(r)$  function needs to be accurately known (by which we mean that the low- $r$  part should have a recognisable baseline, and the data not be on an unknown scale). For some investigations, where to know the distances between neighbouring atoms is the primary objective, careful peak fitting is the good approach. For example, author MTD’s first experience using PDF methods [168] was to show that the mean instantaneous Si–O bond length in the

<sup>21</sup> This is primarily a problem for fluids and glasses, and less of a problem for crystalline materials. We note that RMCprofile [152] does in fact attempt to link features of the short-distance part of the PDF with specific pairs of atoms through the use of the ‘distance window’ constraint, by allowing preassigned pairs of atoms to only move within a given range of separations. RMCprofile, and the program RMC\_POT [157] developed for molecular fluids, also allow the use of molecular potentials within individual molecules of small atomic clusters to help the RMC simulation preserve the shape of the molecules.



high-temperature cubic phase of cristobalite (a polymorph of  $\text{SiO}_2$ ) is longer than indicated by the ordered crystal structure, demonstrating that the local structure must have disorder. Using a fingerprint approach, it was also clearly seen that the disordered phase does not consist of small dynamic domains with the structure of the low-temperature tetragonal phase or of another hypothetical phase [41]. Similarly, using peak-fitting methods Hu et al. [169] showed that the mean instantaneous Sc–F bond length in  $\text{ScF}_3$  is longer than would be indicated by the average crystal structure, and that the negative thermal expansion in this material must show rotations of the bond.

By far the most popular quantitative approach to analysing the PDF in recent years has been to fit the PDF with a model crystal structure using a least squares method. For modest degrees of disorder, this approach can show fluctuations of the local structure from the mean. Perhaps the most widespread application has been in the study of nano-materials, where the key application is to identify the atomic structure within the nanoparticle and the size. This is to our mind the key application of the method, and is unrivalled by any of the other methods.

PDF fitting methods have become colloquially known by the name *small box methods*, because the simulation sample is the size of one or two unit cells. The RMC and EPSR methods are then given the colloquial name *large box methods*, because they contain many more atoms within their configurations. In small box modelling, least squares fitting methods are appropriate for the small number of variables, but for the two large box methods there are simply too many variables for robust refinements of the configurations, and so Monte Carlo methods are a more appropriate minimisation method.

The primary reason for choosing one of the large box methods is to be able to use PDF methods to study systems containing a high degree of disorder. Examples range from fluids to crystals in which some components are highly disordered. This case can also include vibrational disorder in crystals. Consider that in the case of a crystal system where the primary atomic fluctuations are due to harmonic-like waves, in order to properly simulate a system it is necessary to have a configuration that is large enough to support a sufficient number of waves. For a cubic crystal with a configuration generated as a  $N \times N \times N$  supercell of unit cells, there will be  $N^3$  wave vectors in the first Brillouin zone of the simulation configuration arranged in a regular grid, with separation of size  $a^*/N$ . As in a molecular dynamics simulation, a small sample will lead to insufficient sampling of wave vectors in reciprocal space.<sup>22</sup>

The question of whether to use RMC or EPSR methods hinges on the problem being studied. For a molecular fluid, the constraints imposed by the use of robust interatomic potentials may point to the use of EPSR methods being most appropriate. On the other hand, for studies of crystalline materials, RMC methods that explicitly include the information contained within the Bragg peaks give the most sensible approach, not least because these methods also contain constraints that overcome some of the potential problems with RMC-based methods.

## 6. PDF studies in the 2020s

Before we give a number of examples of various uses of PDF methods, it is useful at this point to reflect on the background information presented so far and to make some points about contemporary PDF studies.

PDF methods are not easy, and some would say they are hard. In principle the task sounds straightforward: collect total scattering data, remove backgrounds and account for attenuations from the various components of the instrumentation and aspects of the experimental setup, normalise all the individual detectors, take account of factors such as incoherent scattering, attenuation by the sample, multiple scattering and some effects associated with inelastic scattering, subtract the self scattering, and then perform the Fourier transform to give the PDF.

<sup>22</sup> If the value of  $N$  is chosen badly, such as an odd number, the sampling of reciprocal space may be badly biased.

However, the fact that we have already pointed out a number of problems, including the existence of systematic errors of unknown origin, should have sent a warning that PDF methods are far from automatic and straightforward.

The problem is not helped by the pressure users feel to maximise the number of measurements that they can perform in an allocated period of time on the neutron beam. Originally it was expected that a careful experiment would have long running time, and be performed usually only at ambient temperature. Now there is pressure on users to reduce running time in order to secure more measurements, and there is similarly pressure on neutron facilities to promote the speed at which a PDF can be measured. This pressure partly comes from the very fast running times that can be achieved at synchrotron radiation facilities.

In short, there was once a time when PDF measurements were the preserve of a select group of professionals. Now it is right that PDF methods should be *de-professionalised*. However, the problems do not evaporate simply because we say the method has become de-professionalised. Total scattering data that are obtained in too short a time, and then poorly normalised and transformed to the PDF without sufficient care, may not be fit for purpose.

We recommend the reader to look back at some of the earlier work by Adrian Wright, one of the pioneers of modern neutron PDF methods [21, 25, 26, 135, 170]. His work straddled across the transition from reactor-based instrumentation to the use of spallation neutron sources. It is an exemplar of how to obtain PDFs of high quantitative value, and to our minds this work provides the benchmark for the standard of work that should be obtained in modern experiments.

## 7. Examples of PDF studies

### 7.1. Atomic structure of an organic amorphous network

There is great interest in finding new porous materials, and one class of such materials is based on networks of points with tetrahedral connections. Crystalline examples are silicon and diamond, and the various phases of  $\text{SiO}_2$  at ambient pressure.  $\text{SiO}_2$  has a higher degree of porosity than elemental silicon because the Si–Si distances – the distances between the tetrahedral points – are stretched by including the intermediate oxygen atom to create Si–O–Si linkages. If the single oxygen atom is replaced by a molecular anion, as in  $\text{Si}(\text{NCN})_2$  [172–175],  $\text{Zn}(\text{CN})_2$  [176] and  $\text{Zn}(\text{C}_3\text{N}_2\text{H}_3)_2$  [177], even greater porosity is created. However, in the crystalline networks such as  $\text{Si}(\text{NCN})_2$  and  $\text{Zn}(\text{CN})_2$  the large voids are filled by a second identical sublattice to create structures with two interpenetrating networks. In that case, amorphous networks of such systems may be more promising, because the long-range disorder of the atomic structure prohibits the co-existence of interpenetrating networks.

We recently showed that the amorphous phase of zinc imidazolate,  $\text{Zn}(\text{C}_3\text{N}_2\text{H}_3)_2$ , gives total scattering and associated PDFs that are consistent with a continuous random network of tetrahedral Zn sites that are connected via the molecular ligands [113], exactly as in amorphous  $\text{SiO}_2$  [32]. The atomic structure of this phase was refined using the RMC method. More recently a new highly-porous amorphous material has been created, in which carbon atoms on tetrahedral sites are connected via biphenyl moieties [178]. Whilst many aspects of such materials can be characterised by methods that can measure porosity and inner surface areas, the best that standard x-ray diffraction can do is point to the absence of Bragg peaks and hence demonstrate that the material is amorphous.

We have recently tackled the challenge of identifying the atomic structure of this new network – called PAF-1 (Porous Aromatic Framework (PAF) number 1) [178] – using a combination of neutron total scattering and molecular dynamics simulations [171]. For this work we exploited the fact that the neutron scattering lengths of the two isotopes



of hydrogen,  $^1\text{H}$  and  $^2\text{H}$ , have different signs of their scattering lengths  $b$  (recall the role of this parameter in equations in Section 2).<sup>23</sup> Thus samples containing different amounts of  $^1\text{H}$  and  $^2\text{H}$  were prepared, and total scattering was measured using the NIMROD diffractometer at ISIS [98,99,107]. Recall that this instrument is optimised for total scattering from light elements (Section 4.1).

Ideally the structure of PAF-1 would have been refined using the RMC method, but it was found in the experiments that there was significant small-angle scattering varying as  $Q^{-4}$  and overlapping too much with the low- $Q$  part of the total scattering signal. It was not possible to remove the small angle scattering with sufficient accuracy to enable transformation of the total scattering data to give the PDFs. Thus the approach taken was to use the total scattering data for different  $^1\text{H}/^2\text{H}$  ratios to confirm the validity of a model for the atomic structure.

The atomic configurations were generated by first decorating a set of continuous random networks of tetrahedral sites with the connecting biphenyl moieties, using a simple Monte Carlo algorithm to avoid close H-H contacts, and then relaxing the structure with the molecular dynamics (MD) method with well-tested force fields. Full details are given by Cai et al. [171]. An example of one atomic configuration is given in Fig. 12a. The atomic structures were then used to calculate the partial  $d(r)$  functions for all three atom pairs (as defined in the discussion leading to equations (17) and (18)), as shown in Fig. 12b. These were combined using equation (18) with appropriate values of the neutron scattering lengths for the different samples, and transformed to give  $Qi(Q)$  for each sample. The calculated  $Qi(Q)$  functions were then compared with the neutron total scattering measurements; one example is given in Fig. 12c. The consistent agreement between calculation and experiment for different  $^1\text{H}/^2\text{H}$  ratios confirmed that the configurations generated by the MD simulations are a good representation of the atomic structure. On this basis, it was then possible to analyse various aspects of the atomic structure with some degree of confidence.

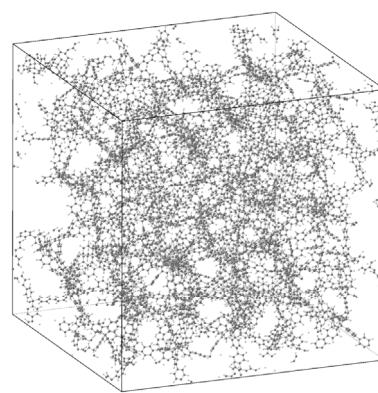
One interesting feature of the partial  $d(r)$  functions shown in Fig. 12b are the long-wavelength oscillations extending to high values of  $r$ . Their Fourier transform gives a sharp peak at a low value of  $Q$ , approximately  $0.45 \text{ \AA}^{-1}$ . This is seen in the calculated  $Qi(Q)$  functions, Fig. 12c, and is seen in the experimental data as a peak superimposed on the rising small angle scattering. Cai et al. [171] pointed out that this peak is directly analogous to the first sharp diffraction peak seen in amorphous silica, which has attracted considerable interest, as well as controversy, over many years [179–184].

There is of course a long history of using PDF methods for studying amorphous materials. We can cite the example of silica glass [21]. The first serious study, using x-ray PDF methods with a combination of radiation from copper and molybdenum targets, was performed as early as the 1930s [185,186]. This work led to an understanding that the atomic structure of silica glass consists of  $\text{SiO}_4$  tetrahedra as discussed in Section 5.2. Many other amorphous systems have been studied by PDF analysis, including oxides, chalcogenides, and hybrid metal-organic frameworks [113].

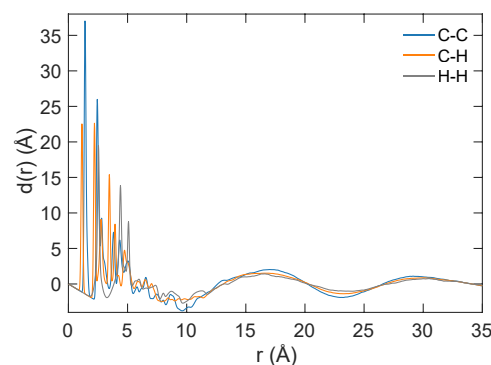
## 7.2. Negative thermal expansion in scandium trifluoride

Having several times in this paper cited data from our study of  $\text{ScF}_3$  [20], and shown some examples (Figs. 2, 9 and 10), it is fitting to tell the scientific story that prompted this work.  $\text{ScF}_3$ , whose crystal structure is shown at the top of Fig. 2, is one of the more-important materials that shows the anomalous property of negative thermal expansion (NTE) [187]. Its importance comes from two features: one is that its crystal

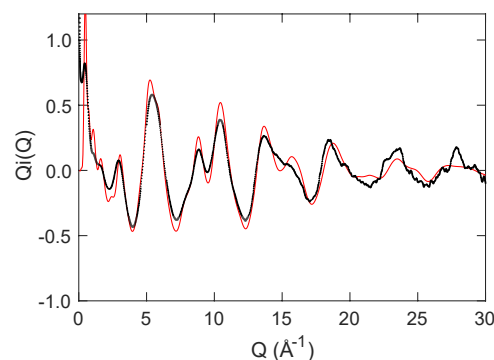
<sup>23</sup> It is one of the interesting, and sometimes useful, features of neutron scattering that for some atomic isotopes the scattering length  $b$  has a negative value [120,121]. This reflects a change in the sign of the wave function during the scattering process. Other examples are  $^7\text{Li}$ , and the standard isotopes of titanium and manganese. This is discussed in the Appendix.



(a) Atomic structure of PAF-1 from MD



(b) Partial  $d(r)$  functions from MD configuration



(c)  $Qi(Q)$  function for one sample

**Fig. 12.** a) One atomic configuration of PAF-1 obtained from MD simulation. b) Partial  $d(r)$  functions for all three atomic pairs in PAF-1, calculated from the atomic configurations obtained from MD simulation. c) Calculated  $Qi(Q)$  function for one  $^1\text{H}/^2\text{H}$  configuration (red curve) compared with corresponding experimental neutron total scattering data (black points). Data are from the paper of Cai et al. [171]. (For interpretation of the references to colour in this figure legend, the reader is referred to the Web version of this article.)

structure is relatively simple and isotropic, and the other is that the negative thermal expansion exists for a wide range of temperatures.

Total scattering data for  $\text{ScF}_3$  were obtained across a wide range of temperatures using the POLARIS diffractometer at ISIS [92,93], from which the PDFs were extracted. The full set of total scattering data, PDFs and Bragg diffraction patterns were used as the data in RMC refinements. The quality of the agreement between the RMC results and data is indicated in Fig. 2. The configurations obtained from the RMC were analysed

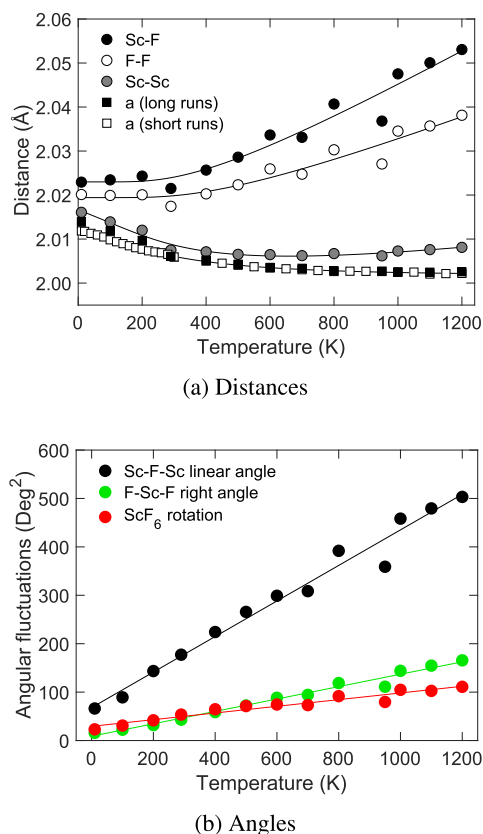


**Fig. 13.** a) Comparison of mean instantaneous nearest Sc-F, F-F and Sc-Sc distances, and lattice parameter *a*, scaled by 1,  $\sqrt{2}$ , 2 and 2 respectively for easy comparison. b) Comparison of the mean square fluctuations of the instantaneous Sc-F-Sc angles, F-Sc-F angles, and ScF<sub>6</sub> orientations. Data are from the paper of Dove et al. [20].

to give information supporting our quest to understand the NTE in ScF<sub>3</sub>.

Fig. 13a shows a comparison of the temperature-dependence of various short-range distances in ScF<sub>3</sub>. The interesting point is that the Sc-F bond length is seen to have normal positive thermal expansion for all temperatures in spite of the NTE seen in the lattice parameter and Sc-Sc closest distance. This result has been seen in independent studies using both neutron [134] and x-ray [144,169] total scattering methods. The most obvious point to be drawn from these data is that the NTE arises from rotations of the Sc-F bonds. Given that the crystal structure contains linear Sc-F-Sc linkages, rotations of the Sc-F bonds leads to large transverse displacements of the fluorine atoms (as displayed in the representation of the crystal structure shown in Fig. 2), and since the Sc-F bonds are relatively stiff, these motions pull the two Sc atoms towards each other. Since the amplitudes increase with temperature, this inward pull also increases with temperature, and hence we have a simple understanding of NTE.

To stop at this point is too soon. As we argued in our paper [20], whilst this idea contains some elements of the truth, there are also prevailing objections that need to be dealt with. In particular, it is usually the case that the motions of any one atom is correlated with the motions of its neighbours, and this correlation is seen in the shape of the phonon dispersion curves. The argument we have given is that NTE is enabled by the possibility for the ScF<sub>6</sub> octahedra to rotate in concert with their neighbours without distortion in the set of vibrations we have called ‘Rigid Unit Modes’ (RUMs) [188,189]. These modes, which provide the rotations of the Sc-F bonds in this mechanism for NTE [190], will have low frequency and hence large amplitude. This is essential; if the vibrational modes for rotations of the Sc-F bonds are high frequency, they will not have sufficient impact to give an overall NTE given that the Sc-F

bond has normal positive thermal expansion.

Fig. 13b presents the more important results from the study. In this figure we compare the fluctuations of three angles, namely the linear Sc-F-Sc angle, the octahedral F-Sc-F right angle, and the overall rotation of the ScF<sub>6</sub> octahedra. The largest fluctuation is for the Sc-F-Sc angle, which reflects the mechanism for the NTE in terms of transverse motions of the fluorine atoms. The other two fluctuations are of similar size, indicating that the whole body rotations and bond-bending distortions of the ScF<sub>6</sub> octahedra are of similar amplitude.

The important point of this work was to understand the nature of the fluctuations that provide the mechanism for NTE in ScF<sub>3</sub>, given that NTE is not observed in cubic perovskite oxides which have essentially the same crystal structure, albeit with an additional cation located in the centre of the unit cell (defined with Sc atoms on the corners). The key outcome of this study, particularly when combined with molecular dynamics simulations on a simple model and calculations of phonon dispersion curves using Density Functional Theory methods [191], was that the origin of the NTE is associated with the RUMs involving rotations of the ScF<sub>6</sub> octahedra, but for this to be significant it is a necessary condition that the ScF<sub>6</sub> octahedra are more flexible than their oxide counterparts. In this way the effects associated with the RUMs can also be enacted by the set of phonons that have wave vectors close to those of the RUMs and atomic motions that are RUM-like but involving some polyhedral bond-bending.

This example shows how PDF studies, in this case coupled with RMC modelling, can give unique information about anomalous material properties, particularly the links with fluctuations in the local atomic structure. Other examples where PDF studies have been used to give insights into NTE materials include Zn(CN)<sub>2</sub> [192,193] and some other cyanide compounds [192–197], Cu<sub>2</sub>O and Ag<sub>2</sub>O [198,199], and ZrW<sub>2</sub>O<sub>8</sub> [200–202].

### 7.3. Local order in high-entropy alloys

High-entropy alloys (HEA) are metallic alloys containing a few principal elements in more-or-less equal quantities [203]. These form with full disorder of the atoms across a simple crystal structure (body-centred or face-centred cubic) without the formation of ordered regions. It has been found that HEAs may have some advantages over conventional alloys in terms of their mechanical properties, such as having greater resilience against fracture with higher tensile strengths, and higher strength-to-weight ratios. It has also been suggested that it is the entropy arising from distributing equal numbers of different atoms over the crystallographic sites that gives these alloys their thermodynamic stability.

Nygård et al. have recently reported a study of the HEAs TiVNb, TiVZrNb and TiVZrNbHf (3–5 components) using both neutron and x-ray PDF methods, with analysis by the RMC method [24]. These compositions were chosen so that the range of size differences varies from just over 4% to nearly 7%. This is actually an excellent example of the complementary use of the two types of radiation. As noted before, the x-ray scattering factor is proportional to the atomic number, so in the 5-component alloy the Ti and V (21, 22) have almost the same scattering factors, as do Zr and Nb (40, 41), with Hf having substantially larger scattering factor (72). Neutron scattering provides some contrast. Ti has a negative scattering length, and the scattering length of V is virtually zero. On the other hand, the other three elements have nearly the same neutron scattering length. This means that contrast between Hf and other elements is given in the x-ray PDF, whereas neither x-rays nor neutrons will distinguish between Zr and Nb. These alloys all have body-centred cubic structures. Samples were also made that contain absorbed deuterium, with approximately twice as many deuterium atoms as metal atoms, and these materials have a face-centred cubic crystal structure.

The RMC results showed that the distributions of the metal atoms in each sample of HEA was almost completely random, with only a small and subtle degree of neighbour correlations for distance neighbours. The

results also gave indications of the local strains. In the deuterides, the deuterium atoms occupy the tetrahedral sites of the cubic close-packed alloy structure, to form a  $\text{CaF}_2$ -type structure. A slightly higher degree of metal site ordering was found, particularly with regard to favoured neighbours for the deuterium atoms.

The same group also conducted a similar study of the deuterium-containing alloy  $\text{Ti}_{0.63}\text{V}_{0.27}\text{Fe}_{0.10}\text{D}_{1.73}$  in an investigation of the use of alloys for storage of hydrogen [204]. In this case the question they were investigating concerned the role of iron content in limiting hydrogen uptake into Ti–V alloys. The RMC modelling showed the presence of Fe-rich clusters, and that the majority of the vacant interstitial sites were within these clusters.

There is also interest in an analogous HEA effect in oxides. A recent paper by Bo et al. [205] has used neutron PDF analysis with the RMC method to study disorder in the cubic pyrochlore  $\text{Nd}_2\text{M}_2\text{O}_7$ . In this material  $M$  is occupied in equal amounts by tantalum, scandium, tin, hafnium and zirconium. A second measurement was performed on an oxide in which tantalum was replaced by titanium together with a charge-balancing addition of oxygen. Experiments were performed on the NOMAD diffractometer at the SNS [101,102]. The first oxide showed random arrangements of the  $M$ -site cations, whereas the second showed some ordering of Ti with local octahedral distortions.

#### 7.4. Deep eutectic organic mixtures with water

The use of PDF methods to study molecular crystals and fluids has been one of the major areas of application [206]. In this case we face the requirement to understand information regarding the orientations of molecules. In the case of crystalline molecular crystals, particularly disordered crystals, there is interest in understanding the orientations of molecules within the absolute spatial reference of the crystal lattice. Our own RMC work on disordered molecular crystals [207–213] has shown that this application can be very fruitful. On the other hand, work on molecular fluids faces the harder challenge of describing relative orientations of neighbouring molecules without any absolute spatial reference. The PDF does not directly contain this information – technically the PDF only contains information regarding the distances between pairs of atoms – but modelling allows the incorporation of constraints, implicit or explicit, that will help the development of realistic configurations. The local structure within these configurations can then be analysed, particularly in terms of the correlations involving orientational relationships between groups of atoms and molecules. This is the subject of this example.

The question of how to describe the relative orientations of molecules was discussed in detail by Svishchev and Kusalik [214,215] in the context of simulations of water molecules, with similar developments being made at the same time by Alan Soper in the context of analysis of the PDF [216,217]. This led to the introduction of the Spatial Distribution Function (SDF) as a way to represent the angular distribution of atoms in one molecule around a central molecule. In the context of PDF work, this problem led to the ongoing development and refinement of the EPSR method (Section 5.5) for the analysis of PDF data for molecular fluids.

There is a lot of current interest in solutions of molecules. Much interest concerns a new class of organic solutions called *deep eutectic solvents* (DESs) [218–221]. These are eutectic mixtures of a salt, such as choline chloride,  $[(\text{CH}_3)_3\text{NCH}_2\text{CH}_2\text{OH}]\text{Cl}$ , which is discussed below, and an organic component that is capable of hydrogen bonding, such as urea [222]. Eutectics give the opportunity to have molecules in the solution state at temperatures well below the melting points of the pure end member systems. These eutectic mixtures of salts and organic molecules have the potential to act as industrial solvents across a range of application areas with much less environmental risk than with current solvents. Furthermore, the properties of these DESs can be modified by addition of water, and there is the possibility to fine-tune any DES for a specific application.

One important organic eutectic system is the solution of choline chloride and malic acid,  $\text{C}_4\text{H}_6\text{O}_5$ , not least because both components can

be naturally sourced. Hammond et al. [224] reported a study of the atomic structure of this solution, with and without water, using neutron total scattering data analysed using the EPSR method [158–160]. Experiments were performed with different types of hydrogen/deuterium substitutions to give different shades of contrast in the data, similar to the way that H/D substitution was used in the first example here (Section 7.1). The same group has recently studied the local atomic structure around the hydrophobic aromatic molecule indole,  $\text{C}_8\text{H}_7\text{N}$ , dissolved into this DES in both anhydrous and hydrated states [223], using the same H/D substitutions, and with experiments performed on the NIMROD diffractometer at ISIS [98,99,107]. The core results are summarised visually in Fig. 14, which we now discuss.

Fig. 14 shows a representation of the SDF for several cases, with a comparison of both nominally anhydrous (0.1 wt%  $\text{H}_2\text{O}$ ) and hydrated (11.6 wt%  $\text{H}_2\text{O}$ ) solvents. The figure shows the isosurfaces for different species having different orientations with respect to the molecule of interest. The top row in Fig. 14, which considers the average environment around the choline molecules, shows how the chloride ions associate with both the  $-\text{OH}$  group and the part of the molecule with positive charge. The molecules of malic acid then arrange to form hydrogen bonds with each other, with the chloride ions, and with the choline molecules. It appears that hydration has little effect on this local structure.

The second and third rows of Fig. 14 show the solvation of the indole molecules by cholinium (yellow) and chloride (green) ions, and by the malic acid (orange) and water (blue) molecules, respectively. The second line shows that the chloride ions have a clear interaction with the  $-\text{NH}$  groups of the indole molecules, and a second interaction with an acid site at the opposite side of the molecule. The effect of water within the DES is to broaden the orientational distribution slightly. The third line shows

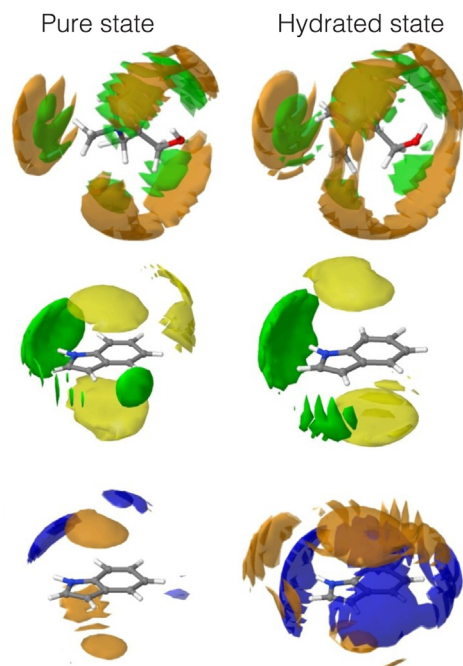


Fig. 14. Spatial density function plots for the choline chloride/malic acid deep eutectic solution containing indole, obtained by EPSR modelling using neutron total scattering data [223]. The left column shows the nominally anhydrous case (0.1 wt%  $\text{H}_2\text{O}$ ) and the right column shows the case with 11.6 wt%  $\text{H}_2\text{O}$ . The top two images show isosurfaces representing the solvation of the choline molecule by the chloride ion (green surface) and by the malic acid molecule (orange surface). The middle and bottom pairs of images show the isosurfaces representing the solvation of the indole molecule by cholinium ions (yellow), chloride (green), malic acid (orange) and water (blue) surfaces. (For interpretation of the references to colour in this figure legend, the reader is referred to the Web version of this article.)



both the interactions of the indole molecule with malic acid and water. The most interesting feature identified by the authors [223] is the way in which the water molecules have come close to the normally hydrophobic indole molecule, to an extent greater than is accounted for simply from the concentration of water. On the other hand, the malic acid molecules do not interact strongly with the indole molecules in either state of hydration.

Hammond et al. [223] pointed out that if one of the advantages of DESs is that they can be tuned for specific applications, this requires detailed understanding of the relationship between local structure and properties. Without this understanding, the tuning can only be based on iterative experience rather than rational design. Thus PDF experiments such as those summarised here are of critical importance in the study of organic solutions.

### 7.5. Atomic and magnetic structure of iron-oxide nanoparticles

One of the key applications of PDF studies – historically x-ray PDF more than neutron PDF – has been in the study of small nanoparticles [225–228], which included the development of the DISCUS software [225] specifically for building models of nanoparticles and calculation of the PDF. Much of this work is being carried out using x-ray PDF analysis [18], but the example we discuss here is one for which neutrons have some advantages.

Iron oxide nanoparticles, mostly with the spinel structure of notional composition  $\text{Fe}_3\text{O}_4$ , have a number of potential applications in both the technological [230–232] and medical [233–238] areas. The structure of iron oxide nanoparticles with chemical composition  $\text{Fe}_{3-x}\text{O}_4$ ,  $x \sim 0.2$ , has recently been investigated using a combination of x-ray and neutron powder diffraction and total scattering, with data analysed by both the Rietveld method and PDF fitting [229]. Neutron data were obtained on the NOMAD diffractometer at the SNS [101,102].

It was found that the atomic structures of the nanoparticles have spinel form, characteristic of the  $\gamma\text{-Fe}_2\text{O}_3$  structure, with a tetragonal distortion and space group  $P4_32_12$  [229]. The atomic structure is shown in Fig. 15, where the image highlights the  $\text{FeO}_4$  tetrahedra and  $\text{FeO}_6$  octahedra, and in particular the ordering of Fe vacancies.

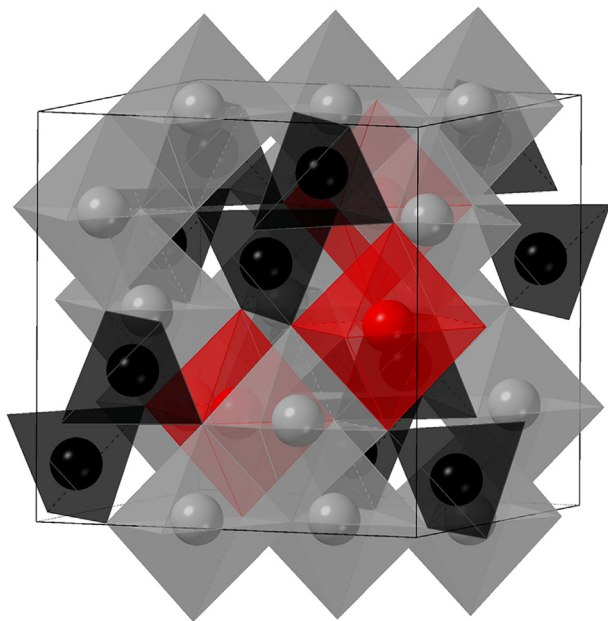


**Fig. 15.** Atomic structure of  $\text{Fe}_{3-x}\text{O}_4$ ,  $x \sim 0.2$ , nanoparticles obtained by both Rietveld analysis and PDF-fitting from neutron scattering data [229]. The structure is of modified spinel form, with space group  $P4_32_13$ . The image shows  $\text{FeO}_4$  tetrahedra (black polyhedra), fully-occupied  $\text{FeO}_6$  octahedra (grey polyhedra), and partially occupied  $\text{FeO}_6$  octahedra (red polyhedra), with oxygen atoms on the polyhedral corners in each case. (For interpretation of the references to colour in this figure legend, the reader is referred to the Web version of this article.)

number of other models were proposed and tested, including a model in which the nanoparticles have a core of  $\text{Fe}_3\text{O}_4$  and a shell of  $\gamma\text{-Fe}_2\text{O}_3$ , but the evidence clearly pointed to a homogenous structure with vacancy ordering.

The experiments performed in this study were both x-ray and neutron PDF measurements. Whilst the x-ray PDF measurements are sensitive only to atomic structure, the neutron PDF data show effects of magnetic order. The PDF fittings of the neutron data are shown in Fig. 16. Fitting without accounting for the magnetic structure was reasonable, but the difference between the data and fitted PDF showed systematic oscillations that could be accounted for by inclusion of magnetic order into the model. This gave an excellent agreement between the fitted PDF and

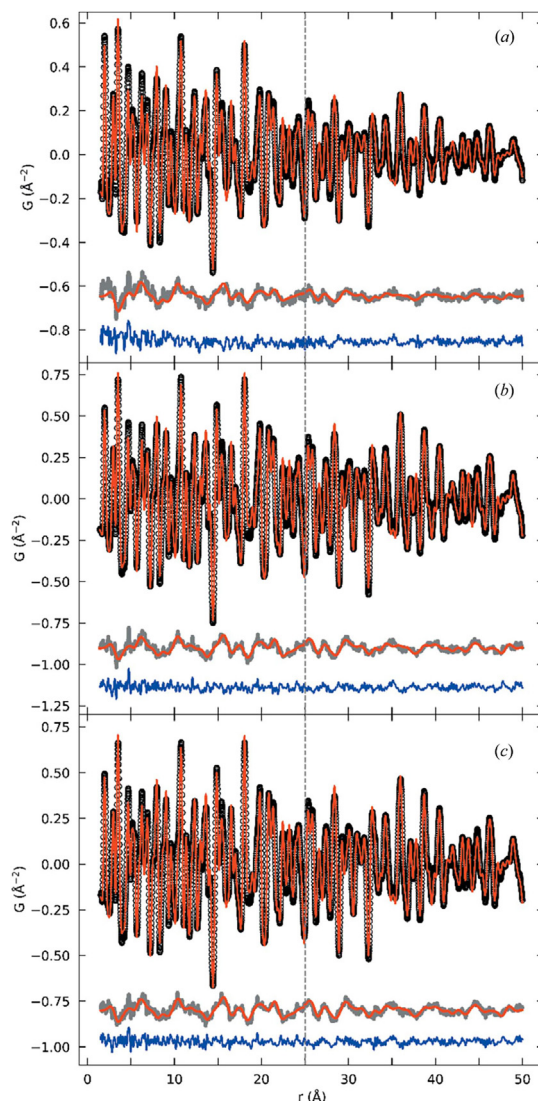


**Fig. 16.** Example of using the method fitting PDF data [116,140], in this case with PDF data obtained from three iron oxide nanoparticles, synthesised at temperatures a) 340, b) 390 and c) 440 °C. The data have been fitted using a spinel structure with tetragonal distortion and one set of vacant iron sites [229]. The grey curves below each data set give the difference between the PDF from the atomic structure and data, and show oscillations that reflect the magnetic structure. The red curves overlaying the grey curves represent the fitted magnetic contribution, and the blue curve shows the resultant difference between the overall model (structural and magnetic PDF) and the data. The vertical dashed line indicates that two ranges of distance were used in the fitting. Note that what these authors have called  $G(r)$  is what we and others call  $D(r)$  [23]; see our discussion of nomenclature in Section 2.4. (For interpretation of the references to colour in this figure legend, the reader is referred to the Web version of this article.)



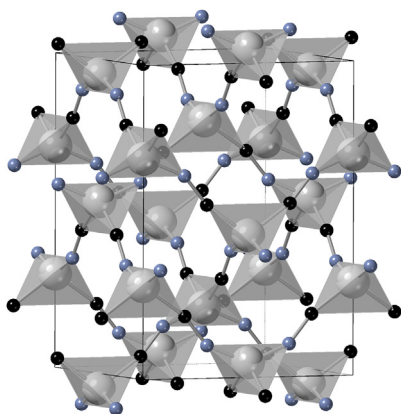


**Fig. 17.** Atomic structure of ordered  $\text{Cd}(\text{CN})_2$  at low temperature (space group  $I4_1/amd$ ) [243]. The image shows Cd-centred tetrahedra (grey polyhedra), with C and N as black and blue spheres respectively. Each Cd tetrahedron has two carbon and two nitrogen atoms, with an off-centre position of the Cd atom. (For interpretation of the references to colour in this figure legend, the reader is referred to the Web version of this article.)

data. The analysis of the magnetic PDF showed that the magnetic structure has ferrimagnetic order, with the magnetic core occupying.

As we noted at the start, most PDF measurements on nanoparticles have been performed using x-ray facilities. However, there are cases where the features of neutron scattering can be usefully employed for this application, as this example shows.

#### 7.6. Spin-ice physics in cadmium cyanide

At high temperature the crystal structure of  $\text{Cd}(\text{CN})_2$  [239,240] is isomorphic with that of  $\text{Zn}(\text{CN})_2$  [240,241], which we have cited above (Section 7.2) as one of the most important NTE materials [176], and for which there have been previous PDF studies reported [192,193]. In fact, the NTE in  $\text{Cd}(\text{CN})_2$  is 20% larger than in  $\text{Zn}(\text{CN})_2$  [176]. The crystal structure of  $\text{Cd}(\text{CN})_2$  has cubic space group  $Pn\bar{3}m$ , with head-to-tail disorder of the cyanide ions [241]. At a temperature of 130 K there is a structural phase transition [176,242] with lowering of the crystal symmetry to the tetragonal space group  $I4_1/amd$ , as shown in Fig. 17. [242, 243]. The lower symmetry then allows for ordering of the head-to-tail orientations of the cyanide molecules. Coates et al. [243] have explored this point in more detail recently using a variety of experimental and simulation techniques, including measurements of the PDF.

Before we discuss the science, it is useful to note that this example highlights a point that will be discussed in the Appendix (Section 10.3), namely that natural cadmium contains one isotope,  $^{113}\text{Cd}$  (12% abundance), that has a very high absorption of neutrons. Thus natural cadmium is really unsuitable for neutron scattering experiments. Because of this, samples used in this study were made using the  $^{114}\text{Cd}$  isotope [243], which has virtually no absorption of neutrons, and it also has the largest scattering length of all the other isotopes of Cd.

The neutron PDFs measured in this study are shown in Fig. 18. The largest effect in  $D(r)$  that can be seen across the range of distances for  $r > 6 \text{ \AA}$  is mostly due to the lattice strain associated with the phase transition, giving more detailed structure in the oscillations. An example is in the range 25–28  $\text{\AA}$ , but this sort of change in the PDF on cooling is seen across the full range of distances. The important region for analysis of the local ordering of CN anions about the Cd atoms is in the range 3–4  $\text{\AA}$ .

It was possible from the PDF to extract quantitative information about the relative populations of different Cd environments,  $\text{CdC}_n\text{N}_{4-n}$ , for different temperatures. The results for the high-temperature cubic phase are shown in Fig. 19, where they are compared with similar results obtained from  $^{113}\text{Cd}$  magic-angle spinning NMR experiments, and also from

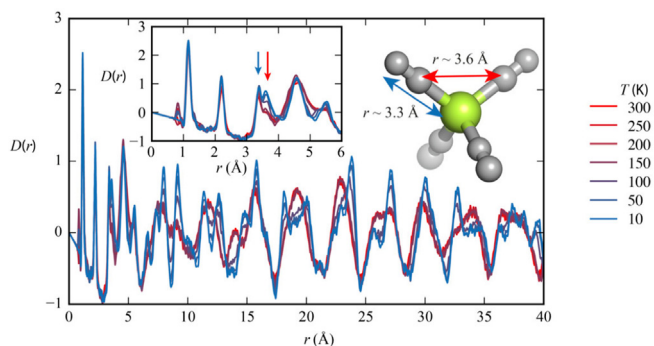


**Fig. 18.** Pair distribution function  $D(r)$  for  $\text{Cd}(\text{CN})_2$  for a range of temperatures encompassing both ordered ( $T < 130 \text{ K}$ ) and disordered phases. The figure is from Coates et al. [243] (Supplementary Information). Again, note that the data are commendably shown down to  $r = 0$ .

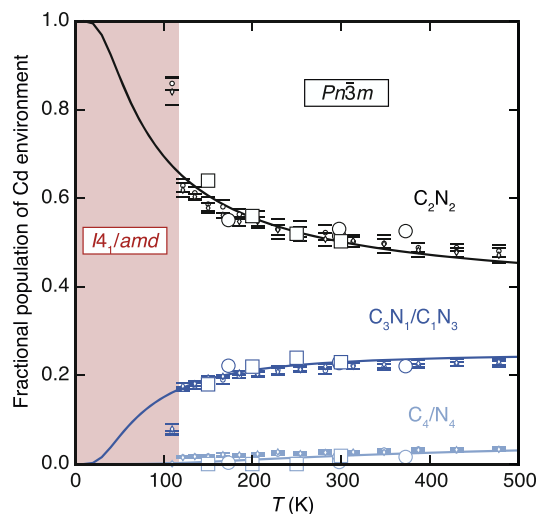


**Fig. 19.** Population of different types of cadmium environment in  $\text{Cd}(\text{CN})_2$  as a function of temperature. Open squares are the result of analysis of the PDFs, large open circles are the results from  $^{113}\text{Cd}$  magic-angle spinning NMR spectra, and small circles are from simulation. The figure is from Coates et al. [243].

Monte Carlo simulations of a parameterised model Hamiltonian [243].

This example shows the value of PDF measurements, with quantitative analysis, used as part of a larger study of a material's properties using a range of experimental and simulation techniques. In this study the PDF gave supporting evidence consistent with the results of other methods, lending weight to the overall conclusions.

## 8. Discussion and forward look

We hope that we have given the impression that the situation for scientific research using PDF analysis is very healthy, with good experimental facilities and analysis methods. It is our conviction that PDF methods can give *unique* insights into the atomic structures of disordered materials, ranging from fluids to weakly-disordered crystalline materials. In many ways the field has matured in recent years, particularly with faster measurements being possible due to enhanced instrumentation. We are encouraged that new facilities, such as CSNS in China, automatically considered a PDF instrument to be a priority, and enabling it to be one of the earliest instruments to come into operation. On the other hand, only ISIS has invested in a deeper way in PDF studies, not only in having four PDF instruments instead of just one, but in having some of these instruments optimised for light elements. It needs to be understood by the scientific community, and by funders, that providing a solution to the problem of accurate measurement of PDFs from materials containing light elements is

not merely a luxury but is essential for much of modern research.

We hope too that we have made clear that measurements of PDFs are not as trivial as sometimes they can appear to be. That is not a message of despair, but giving notice that caution should be wisely heeded. It is right that PDF measurements need to be de-professionalised, because the advantages of PDF measurements coupled with good analysis are too significant for the method to be left only to the professionals. But de-professionalisation does not mean that users can be absolved of responsibility. We want to make clear our conviction that users have a continued responsibility to take ownership of their data, including understanding issues associated with the quality of their data. Users also need to do the work required to understand the information contained within the PDF. In part this will guard against the danger of making unwarranted claims from their data. We continue to advise that one way to avoid risks in the interpretation of PDF data is to use models where the constraints from the model are unambiguous. This includes comparing the data with models to check issues such as near-neighbour coordination numbers obtained as integrals of the peaks in the PDF. In this sense, we advise against the use of data that are not placed on an absolute or properly normalised scale. We also urge caution in the use of PDF data that do not appear to be well-behaved in the two limits  $r \rightarrow 0$  and  $r \rightarrow \infty$ .

Looking to the future, we anticipate a few trends. *First*, as spallation neutron sources follow the example of ISIS and add a second target station, we envisage the development of more instruments, hopefully taking seriously (as do ISIS) the need for instruments that are optimised for the study of materials containing light elements. Most of the current instruments are actually simultaneously good diffractometers, and for work on disordered crystalline materials the ability to measure the total scattering and a high-resolution diffraction pattern simultaneously is essential. This was, in our opinion, the scientific breakthrough represented by the development of the GEM diffractometer at ISIS [28,36,94], because at that time all PDF instruments had little concern for a simultaneous diffraction measurement. In this regard, we advocate that instruments optimised for light elements, where the layout of detectors primarily has them positioned with smaller scattering angles ('forward direction'), should include a set of detectors at a scattering angle close to  $90^\circ$ .<sup>24</sup>

A *second trend* for the future, which need not require much development, is an increased role of PDF + RMC analysis for the study of magnetic materials. We do not advocate the need for special analysis to give magnetic PDFs; recall that in the EPSR method there is little emphasis placed on the overall PDF, with the key data being the total scattering signal. It is the case that the RMC method also can give the magnetic ordering and associated fluctuations without needing a special magnetic PDF to be isolated. However, it is also necessary to ensure that magnetic scattering isn't automatically (and unintentionally) excluded from the data through the data reduction and correction processes.

RMC studies of magnetic structures were first developed by David Keen and Robert McGreevy [244–247]. This approach was then developed within the RMCprofile package [152] and has been used for the study of magnetic order in both the antiferromagnetic and paramagnetic phases of MnO [248,249] and other examples [250–252]. An excellent description of the implementation of the RMC method for magnetic systems has been given within the context of the more-recent SPINVERT software [253], designed to study paramagnetic disorder rather than magnetically-ordered phases. Although we have cited several studies, our feeling is that the potential for studies of magnetic structure using the RMC method has yet to be unlocked beyond these pioneering studies.

A *third trend* for the future is to make greater use of combining neutron and x-ray PDF measurements within a single study. The complementarity of the two types of radiation means that they give

different views of the atomic structure, with different atom types having different weightings in the two. Some examples were given earlier in this paper (Sections 7.3 and 7.5).

A *fourth trend* will be to use neutron PDF measurements to study local structure at high pressure [129,254]. This is far from trivial, because the pressure cells scatter the beam and this scattering needs to be accurately accounted for. Furthermore, it is possible that the data corrections will be different at each pressure as the anvils move together and as the encapsulated sample decreases in size, making the correction measurements complicated.

A *fifth trend* is to include three-dimensional data. There are a number of crystalline materials where there is significant structure of the diffuse scattering in three-dimensional reciprocal space. Sometimes this might be an arrangement of rods of diffuse scattering, but there may also be more complicated shapes of diffuse scattering. Given that RMC normally works with one-dimensional data, much of the information contained within the three-dimensional shape of the diffuse scattering is lost. Much of this scattering is at relatively low values of  $Q$ , at least compared to the typical values of  $Q_{\text{max}}$  that can be obtained on a neutron total scattering instrument, so the resolution of this information in real space will be relatively low. But coupled with the higher- $Q$  data of the total scattering data, and the three-dimensional indexing of the Bragg scattering data included in the RMC analysis, inclusion of three-dimensional diffuse scattering can add significant information. But we do not want to give the impression that all is lost without three-dimensional data. Interestingly, PDF + RMC studies of two polymorphs of silica that undergo displacive phase transitions were able to accurately capture the extensive three-dimensional pattern of diffuse scattering naturally without inclusion of three-dimensional data [255–257]. The route towards modelling based on three-dimensional diffuse scattering was laid out a decade ago by Thomas Weber and Arkadiy Simonov [258], and recently this approach has been developed into an RMC approach for neutron scattering measurements from single crystals in the software *rnc-discord* by Morgan and colleagues [259]. It is probable, given the need for single crystals of sufficient size, that three-dimensional data will be more dominated by x-ray [260] or electron scattering [261] data rather than for neutron scattering data, except for studies of magnetic structure [262]. Because three-dimensional data have a relatively low maximum value of  $Q$ , inevitably the real-space resolution for three-dimensional models is lower than for results discussed in this review. For many applications, this is not a problem, but there is a strong argument in favour of combining three-dimensional data with one-dimensional data taken to higher values of  $Q$  in order to recover a higher resolution in real space.

Although not yet a *sixth trend*, we believe that with higher-quality data it will become increasingly likely that the outputs of the analysis of the PDF will be used to extract collective properties, namely whole-configuration properties that are constructed as the Fourier transform of the set of single-particles variables. That the PDF may contain information about the phonon dispersion curves was first proposed by Dimitrov et al. [263]. The idea was subsequently challenged [264,265], but without closing the door on the possibility of extracting information about collective excitations from PDF data. The question left open concerned the extent of unique information that is contained within the PDF regarding the excitation spectrum. Goodwin et al. [42,266] explored in some detail what information can be extracted from phonon dynamics using multiple configurations of atoms generated by independent RMC simulations, and compared with calculations of the PDF directly from the phonon spectra [40]. The point was that if the RMC configurations are truly reflecting the real distribution of atoms, it is expected that this distribution is determined by the complete set of normal modes, with wave vectors determined by the numbers of unit cells in each direction of the configuration supercell. The eigenvectors and amplitudes of the normal modes can be obtained as the Fourier transform of the instantaneous atomic displacements from their mean positions. Furthermore, the effective angular frequencies of the normal modes can be obtained as the mean-square averages of the Fourier components, obtained using many

<sup>24</sup> There is no need to make this expensive by covering the full circle with detectors, since Bragg scattering is relatively strong, and overall measurement times are quite long due to the solid angle in the forward direction being relatively small.

independent configurations. The key finding of this study was that it is possible to extract key information about the normal mode frequencies from this process up to a certain maximum frequency, within the lattice dynamics calculations confirming the reduced sensitivity of the PDF to higher frequency modes [42]. The same authors also showed that it is possible to use a similar formalism to extract the frequencies of spin waves in magnetically-ordered crystals [267].

The new approach to modelling the PDF based on fitting the amplitudes of normal modes to the PDF discussed in Section 5.3 [143] effectively builds on the earlier work based on RMC [42,266] – certainly on the optimism of this work – although this new approach has two important differences from the RMC approach. The first is that the normal modes are identified in advance, whereas in the earlier analysis of RMC configurations the normal modes are identified by diagonalisation of a correlation matrix. The second is that the fitting to the PDF is essentially limited to a small configuration and hence a small number of wave vectors.

## 9. Summary

We have attempted to introduce experimental methods based on the neutron pair distribution function with an eye to giving pertinent information for the newcomer to the technique. It has not been our intention to evangelise for the use of PDF methods, even though we are enthusiasts for the method and believe that there are many areas of materials physics and chemistry where PDF-based studies can give unique information. Instead we have taken the view that the case for using PDF methods has already been made to the satisfaction of our readers, and therefore our discussion has focussed on details that prospective users need to know. These not only include an understanding of aspects of the background theory and associated terminology, but also some knowledge of experimental methods, methods for treating the experimental data, and methods for analysis of the PDF. Since our approach is not evangelical, we have stressed some of the potential pitfalls with the PDF method, and some of the responsibilities that fall onto the user. These responsibilities are both in terms of actions and in gaining essential knowledge. Finally we have given some examples using PDF methods from contemporary research, with a diversity that we hope highlights the flexibility of the PDF method.

We are convinced that PDF methods have an important role in modern research on materials, particularly for materials where there is disorder and a local structure that is not reflected in the average structure. We are convinced that in many cases the information that can be obtained from PDF methods is unique, and worth the investment of the user into developing some level of expertise. It goes without saying that we hope that PDF methods are not seen by users as little more than as having mere decorative value. We hope that the examples we have cited both in Section 7 and throughout the earlier parts of this review paper will act to encourage a wider exploitation of PDF methods.

## 10. Appendix: neutron–nuclei data

### 10.1. Values of the neutron scattering lengths

Data for the neutron scattering lengths for all stable elements from hydrogen to uranium [120] are shown for natural isotopic abundances in Fig. 20. A number of points should be noted from this figure.

*First* is that in contrast to x-ray atomic scattering factors, the neutron scattering lengths do not vary systematically with atomic number. This has some advantages compared to x-ray scattering. For example, light elements scatter neutrons to a similar extent as heavy elements. In x-ray scattering from an oxide composed of heavy elements, the scattering from oxygen will be much less than from the heavy cations, meaning that the data are much less sensitive to the spatial arrangement of oxygen atoms. Similarly, in any study of organic and hybrid metal-organic materials using x-ray methods, hydrogen is almost invisible to the x-rays, particularly if there are heavy elements present. Hydrogen with a neutron

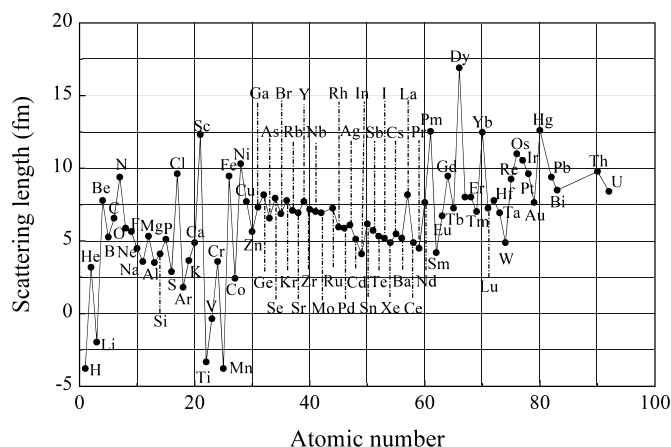


Fig. 20. Neutron scattering lengths for elements with natural isotopic abundance. Data are from the compilation of Sears [120].

scattering length of  $-3.74$  fm, or deuterium with a neutron scattering length of  $6.67$  fm, have comparable visibility in neutron scattering as carbon or nitrogen (neutron scattering lengths of  $6.65$  fm and  $9.36$  fm respectively). Zinc, which is a common element in metal-organic frameworks, has neutron scattering length of  $5.68$  fm, comparable with the values for deuterium, carbon and nitrogen, whereas its x-ray scattering factor is 5 times larger than for carbon and 30 times larger than for hydrogen.

*Second* is that some elements have negative values of their neutron scattering length. This is associated with a  $180^\circ$  phase change in the neutron wave function as it is scattered by the nucleus compared to the case of positive scattering length. The cases are H, Li, Ti and Mn. The negative value of the scattering length provides a very useful contrast with elements of positive value.

*Third* is the near constancy of the values of the neutron scattering length for atomic numbers 30–60. By contrast, over this range the x-ray scattering factors will increase by a factor of 2. This makes it impossible to distinguish between these elements in a neutron scattering experiment, and is why it can be useful to perform complementary neutron and x-ray PDF measurements within a single study.

*Fourth* is the near-zero value of the neutron scattering length for vanadium. This makes vanadium an ideal material for making sample cans for neutron scattering experiments, and also for windows in sample environment equipment. With reference to the second point we made here, it is worth noting that for cases where vanadium is not appropriate, it is possible to make sample containers from an appropriate alloy mixture of zirconium and titanium such that the average scattering length is tailored by composition to have a net value of zero.

*Fifth* is the disappointingly low value of the neutron scattering length for lithium. Values for the two isotopes  $^6\text{Li}$  (natural abundance 7.5%) and  $^7\text{Li}$  (natural abundance 97.5%) are  $2.00$  and  $-2.22$  fm respectively. These values are less than half of the values of the metals we might find in many materials, mainly between 5 and 8 fm, or of oxygen ( $5.80$  fm), which means that the product  $b_j^2$  for pairs of lithium atoms in equation (18) will be correspondingly rather smaller than the products  $b_j b_k$  between pairs of metal atoms or between metal atoms and oxygen atoms. Practically this is a significant disadvantage in the study of lithium-ion battery materials; the low atomic number of lithium means that in practice is not much easier to see than is hydrogen in x-ray PDF measurements.

### 10.2. The case of hydrogen

We have mentioned that the common  $^1\text{H}$  isotope of hydrogen (the proton) has a negative scattering length for coherent scattering, and a very large cross section for incoherent scattering. Whilst the explanation is documented elsewhere, in truth the explanation is not easily found in

modern information sources, and it is the experience of the authors that many PhD candidates who study neutron scattering from systems containing hydrogen do not know why the proton is special. The book of Bée [268] gives a good explanation of many aspects of neutron scattering from hydrogen.

Both the neutron and proton have a nuclear spin of value 1/2. When the neutron and proton interact (via the strong nuclear force), they can form two states with respect to their total spin moment, namely both aligned in the parallel ( $\uparrow\uparrow$ ) state with total nuclear spin  $I=1$ , and antiparallel ( $\uparrow\downarrow$ ) state with total nuclear spin  $I=0$ . It is important to realise that the  $I=1$  state of the deuteron ( ${}^2\text{H}$ , proton + neutron) isotope of hydrogen is stable, but the  $I=0$  state is unstable. Thus the proton can combine with the neutron (in what is called an *absorption process*) to create a deuteron when both spins are in parallel alignment, but will not combine in the antiparallel alignment. This difference means that the scattering lengths for the two processes have positive and negative values respectively. In fact the magnitudes of both are quite large:  $b_{\uparrow\uparrow} = 10.4$  fm, and  $b_{\uparrow\downarrow} = -44.7$  fm.

The coherent scattering length of any element is formally equal to the weighted mean of all possible scattering lengths, given that coherent scattering is sensitive to the average of all states. On the other hand, incoherent scattering reflects the site-by-site fluctuation in the scattering process. To calculate the appropriate mean for neutron scattering from the  ${}^1\text{H}$  isotope, we need to take account of the fact that there are three cases for the  $I=1$  triplet state, namely the projection of spin along the  $z$  axis. These three states are  $I_z = +1, 0, -1$ . Thus the coherent scattering length for  ${}^1\text{H}$  is

$$b_{\text{coh}} = b = \langle b \rangle = (3b_{\uparrow\uparrow} + b_{\uparrow\downarrow})/4 \quad (28)$$

The total cross section is given as  $\sigma_{\text{tot}} = 4\pi\langle b^2 \rangle$ , namely the mean of all cross sections. The coherent cross section is given as  $\sigma_{\text{coh}} = 4\pi\langle b \rangle^2$ . Thus the incoherent cross section is the variance, namely

$$\begin{aligned} \sigma_{\text{inc}} &= \sigma_{\text{tot}} - \sigma_{\text{coh}} = 4\pi(\langle b^2 \rangle - \langle b \rangle^2) \\ &= 4\pi(3b_{\uparrow\uparrow}^2 + 3b_{\uparrow\downarrow}^2 - 6b_{\uparrow\uparrow}b_{\uparrow\downarrow})/16 \end{aligned} \quad (29)$$

The values of  $b_{\uparrow\uparrow}$  and  $b_{\uparrow\downarrow}$  give values of  $b_{\text{coh}}$  that are close to the standard value of  $-3.74$  fm [120], and values of  $\sigma_{\text{inc}}$  that are also close to the standard value of  $80.26$  b (1 b is  $100$  fm $^2$ ). The point is that the different combinations of spin states  $\uparrow\uparrow$  and  $\uparrow\downarrow$  both have large absolute values of scattering lengths, but one has positive value and the other negative. The result is a ‘normal looking’ coherent scattering length obtained as an average, such that the positive and negative terms large cancel, but in the incoherent cross section all terms contribute as large and positive. Thus the incoherent cross section is unusually large.

It is also worth emphasising that for PDF studies incoherent scattering is best avoided if possible, because this adds to the amount of scattering that must be subtracted from the measured signal, and thus it will increase the level of noise. For most practical purposes the main isotope of hydrogen,  ${}^1\text{H}$ , is the one example to be aware of, not least since this has nearly the largest incoherent cross sections of all elements [120]. This problem can be solved by using deuterated samples, although we appreciate that in some cases this may be easier said than done. However, we are aware that inexperienced users, and the people who make samples for them, often under-appreciate the benefits of avoiding absorbing samples and minimising incoherent scattering.<sup>25</sup>

<sup>25</sup> We could have also pointed out earlier – but here is as good as anywhere – that inexperienced users also often under-appreciate the benefits of having large sizes of samples. A typical sample can might be up to 1 cm in diameter and 2 cm long, meaning a sample volume of  $1.5$  cm $^3$  is ideal. Smaller samples mean longer counting times for the same level of accuracy, and because background scattering is a higher proportion of the total signal the statistical accuracy is reduced.

Having made the point that one of the spin states,  $\uparrow\uparrow$ , leads to the possibility of a bound state, it is not surprising that the  ${}^1\text{H}$  isotope has an absorption cross section, which whilst not large, is also not small ( $0.333$  b). It is large enough to have made natural water unusable as a neutron moderator in the first attempts to build a working nuclear fission reactor in the 1940s.

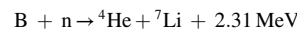
### 10.3. Some absorbing elements

Most atomic nuclei scatter neutrons without significant absorption (or at least with tolerable levels of absorption), but some nuclei absorb neutrons at the energies used in scattering experiments to a significant degree. This may be considered to be both a disadvantage and an advantage.

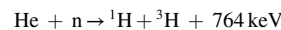
Absorption is obviously a disadvantage if it is strong for one of the elements in the object of our scientific interest. For example,  ${}^6\text{Li}$  has an absorption cross section  $\sigma_a = 940$  b,<sup>26</sup> whereas the corresponding value for  ${}^7\text{Li}$  is only  $0.054$  b. Although  ${}^6\text{Li}$  is the minority component of natural lithium, it still gives an average value of  $\sigma_a = 70.5$  b. Although it is not very high compared to some numbers we will quote below, it is still sufficiently large to make it highly desirable to use samples that are depleted of  ${}^6\text{Li}$  (the examples we will quote below are for very-highly-absorbing materials). We already mentioned in one of our examples, Section 7.6, the use of isotopically pure samples where the natural material has too high a value of  $\sigma_a$ .

Three elements are particularly interesting with regards to the advantages found for their neutron absorption: natural boron with  $\sigma_a = 767$  b ( ${}^{10}\text{B}$  at 20%, abundance has  $\sigma_a = 3835$  b), natural cadmium with  $\sigma_a = 2520$  b ( ${}^{113}\text{Cd}$  at 12.2%, abundance has  $\sigma_a = 20600$  b), and natural gadolinium with  $\sigma_a = 49700$  b ( ${}^{155}\text{Gd}$  at 14.8%, abundance has  $\sigma_a = 61100$  b, and  ${}^{157}\text{Gd}$  at 15.7%, abundance has  $\sigma_a = 259000$  b). These large absorption cross sections mean that these materials are excellent for applications in shielding. For example, coating the inside surfaces of instruments with  $\text{B}_4\text{C}$  significantly reduces unwanted stray scattering of neutrons within the instrument. In applications without significant heating, cadmium, which is ductile and hence easily shaped, is good for shielding components of the sample environment from unwanted scattering. For higher-temperature applications, the more-expensive gadolinium can be used for the same purpose, whether in the form of foil or paint.

The fact that some nuclei absorb neutrons is also central to the detection of neutrons, something that is absolutely essential for the possibility of performing neutron scattering experiments. Early neutron scattering experiments made use of  $\text{BF}_3$  gas in *proportional counters*, which uses the nuclear reaction

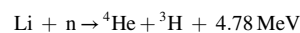


The energy released is shared by the two recoiling nuclei, which generate an electrical pulse that can be measured. It is now more common to use  ${}^3\text{He}$  as the detecting nucleus, with  $\sigma_a = 5333$  b. The nuclear reaction in this case is



${}^3\text{He}$  detectors have more sensitivity than  ${}^{10}\text{BF}_3$  detectors, and need a lower operating voltage. However,  ${}^{10}\text{BF}_3$  detectors have better discrimination of neutrons in the presence of  $\gamma$ -radiation.

${}^3\text{He}$  detectors have become expensive, mostly because  ${}^3\text{He}$  is produced as a decay product of tritium,  ${}^3\text{H}$ , and much less tritium is being produced now following reductions in the development of nuclear weapons. One common alternative is to use  ${}^6\text{Li}$  embedded in a semiconductor in what is called a *scintillator detector*. The nuclear reaction is



<sup>26</sup> 1 b =  $100$  fm $^2$ .



The recoiling nuclei generate a flash of light within the semiconductor as a result of their interaction with the electrons, and the detected flash of light gives the detection of the neutron.

### Use of figures from other papers

Figs. 14, 16, 18 and 19 are reproduced from other publications under the terms of the Creative Commons Licence, details are which are available online. Fig. 14 is from the paper by Hammond et al. [223], and has been constructed here as a composite of Figs. 4 and 7 from the original source. Fig. 16 is from the paper by Andersen et al. [229] and is used without modification. Figs. 18 and 19 are from the paper of Coates et al. [243]. Fig. 18 is used without modification. Fig. 19 has had one set of data removed because the information is not used in this paper. We also modified one axis label. Fig. 11 is from the paper by Božin et al. [138] and is used by permission of the American Physical Society. Fig. 4 is used with permission of ISIS/STFC. All other figures are either created for this paper, or else are taken from our own work [20,171], or from papers from this publisher [90].

### CRedit authorship contribution statement

Martin T Dove: Conceptualization; Investigation; Writing – Original Draft; Writing – Review & Editing; Visualization. Gong Li: Conceptualization; Investigation; Writing – Original Draft; Writing – Review & Editing; Visualization.

### Declaration of competing interest

The authors declare no competing financial interests.

### Acknowledgements

We acknowledge funding from the National Natural Science Foundation of China, grant numbers 12174274 (MTD) and 12274362 (GL), and from the Central Guidance on Local Science and Technology Development Fund of Hebei Province, grant number 216Z1012G (GL). We are grateful to Dr Benqiong Liu (Institute of Nuclear Physics and Chemistry, Mianyang) for the invitation to write this review paper. We are grateful to many colleagues and collaborators who have provided important support over many years, and/or helped in the preparation of this manuscript; in alphabetical order: Edward Beake, Daniel Bowron, Guanqun Cai, Elizabeth Cope, Juan Du, Helen Duncan, Andrew Goodwin, Alex Hannon, Thomas Headen, Qun Hui, David Keen, He Lin, Jiaxun Liu, Anthony Phillips, Yinze Qin, Andrei Sapelkin, Lei Tan, Haolai Tian, Matthew Tucker, Stephen Wells, Wen Yin, Tristan Youngs, Shidong Zhang, Sijie Zhang, and Yuanpeng Zhang. We also thank the reviewers for helpful suggestions.

### References

- [1] W.C. Röntgen, 1. Ueber eine neue Art von Strahlen, *Annalen der Physik und Chemie* 300 (1898) 1–11.
- [2] W.C. Röntgen, 2. Ueber eine neue Art von Strahlen, *Annalen der Physik und Chemie* 300 (1898) 12–17.
- [3] W.C. Röntgen, Weitere Beobachtungen über die Eigenschaften der X-Strahlen, *Annalen der Physik und Chemie* 300 (1898) 18–37.
- [4] W. Friedrich, P. Knipping, M. Laue, Interferenzerscheinungen bei Röntgenstrahlen, *Ann. Phys.* 346 (1913) 971–988.
- [5] W.L. Bragg, The diffraction of short electromagnetic waves by a crystal, *Proc. Camb. Phil. Soc.* 17 (1912) 43–57.
- [6] W.H. Bragg, W.L. Bragg, The reflection of X-rays by crystals, *Proc. Roy. Soc. Lond. A: Math. Phys. Eng. Sci.* 88 (1913) 428–438.
- [7] W.H. Bragg, The reflection of X-rays by crystals (II), *Proc. Roy. Soc. Lond. A: Math. Phys. Eng. Sci.* 89 (1913) 246–248.
- [8] W.L. Bragg, The structure of some crystals as indicated by their diffraction of X-rays, *Proc. Roy. Soc. Lond. A: Math. Phys. Eng. Sci.* 89 (1913) 248–277.
- [9] W.L. Bragg, The determination of parameters in crystal structures by means of Fourier series, *Proc. Roy. Soc. Lond. A: Math. Phys. Eng. Sci.* 123 (1929) 537–559.

- [10] P.P. Ewald, Fifty years of x-ray diffraction. <https://www.iucr.org/pub/50years/roxfordiffraction>, 1999. (Accessed 30 July 2022).
- [11] E.O. Wollan, C.G. Shull, The diffraction of neutrons by crystalline powders, *Phys. Rev.* 73 (1948) 830–841.
- [12] P. Debye, Zerstreuung von Röntgenstrahlen, *Ann. Phys.* 351 (1915) 809–823.
- [13] F. Zernike, J. Prins, Die Beugung von Röntgenstrahlen in Flüssigkeiten als Effekt der Molekülanordnung, *Z. Phys.* 41 (1927) 184–194.
- [14] L. Gelisio, P. Scardi, 100 years of Debye's scattering equation, *Acta Crystallogr. A: Found. Adv.* 72 (2016) 608–620.
- [15] X. Liu, T. Weng, Synchrotron-based x-ray absorption spectroscopy for energy materials, *MRS Bull.* 41 (2016) 466–472.
- [16] T. Egami, S.J.L. Billinge, *Underneath the Bragg Peaks*, 2nd edition, Pergamon, Pergamon, 2012.
- [17] D.A. Keen, Total scattering and the pair distribution function in crystallography, *Crystallogr. Rev.* 26 (2020) 141–199.
- [18] S.J.L. Billinge, The rise of the X-ray atomic pair distribution function method: a series of fortunate events, *Phil. Trans. Roy. Soc. A: Math. Phys. Eng. Sci.* 377 (2019), 20180413.
- [19] C.A. Young, A.L. Goodwin, Applications of pair distribution function methods to contemporary problems in materials chemistry, *J. Mater. Chem.* 21 (2011) 6464–6476.
- [20] M.T. Dove, J. Du, Z. Wei, D.A. Keen, M.G. Tucker, A.E. Phillips, Quantitative understanding of negative thermal expansion in scandium trifluoride from neutron total scattering measurements, *Phys. Rev. B* 102 (2020), 094105.
- [21] A.C. Wright, Neutron scattering from vitreous silica. V. The structure of vitreous silica: what have we learned from 60 years of diffraction studies? *J. Non-Cryst. Solids* 179 (1994) 84–115.
- [22] A.C. Hannon, W.S. Howells, A.K. Soper, ATLAS: a suite of programs for the analysis of time-of-flight neutron diffraction data from liquid and amorphous samples, in: *Neutron Scattering Data Analysis 1990*, Institute of Physics Conference Series, Institute of Physics, 2014, pp. 193–211.
- [23] D.A. Keen, A comparison of various commonly used correlation functions for describing total scattering, *J. Appl. Crystallogr.* 34 (2001) 172–177.
- [24] M.M. Nygård, W.A. Slawinski, G. Ek, M.H. Sørbø, M. Sahlberg, D.A. Keen, B.C. Hauback, Local order in high-entropy alloys and associated deuterides – a total scattering and Reverse Monte Carlo study, *Acta Mater.* 199 (2020) 504–513.
- [25] A.C. Wright, G. Etherington, J.A.E. Desa, R.N. Sinclair, G.A.N. Connell, J.C.M. Jr, Neutron amorphography, *J. Non-Cryst. Solids* 49 (1982) 63–102.
- [26] A.C. Wright, Neutron and X-ray amorphography, *J. Non-Cryst. Solids* 106 (1988) 1–16.
- [27] W.S. Howells, A.C. Hannon, LAD, 1982–1998: the first ISIS diffractometer, *J. Phys. Condens. Matter* 11 (1999) 9127–9138.
- [28] A.C. Hannon, Results on disordered materials from the GEneral Materials diffractometer, GEM, at ISIS, *Nucl. Instrum. Methods Phys. Res. Sect. A: Accel. Spectrom. Detect. Assoc. Equip.* 551 (2005) 88–107.
- [29] X. Qiu, E. Božin, P. Juhas, T. Proffen, S. Billinge, Reciprocal-space instrumental effects on the real-space neutron atomic pair distribution function, *J. Appl. Crystallogr.* 37 (2004) 110–116.
- [30] E. Lorch, Neutron diffraction by germania, silica and radiation-damaged silica glasses, *J. Phys. C: Solid State Phys.* 2 (1969) 229–237.
- [31] E. Lorch, Conventional and elastic neutron diffraction from vitreous silica, *J. Phys. C: Solid State Phys.* 3 (1970) 1314–1322.
- [32] M.G. Tucker, D.A. Keen, M.T. Dove, K. Trachenko, Refinement of the Si–O–Si bond angle distribution in vitreous silica, *J. Phys. Condens. Matter* 17 (2005) S67–S75.
- [33] A.S. Krylov, A.V. Vvedenskii, Software package for radial distribution function calculation, *J. Non-Cryst. Solids* 192–193 (1995) 683–687.
- [34] E. Celeghini, M. Gadella, M.A. del Olmo, Hermite functions and Fourier series, *Symmetry* 13 (2021) 853.
- [35] M. Gao, I. Qun, S. Zhang, S. Zhang, L. Tan, Z. Ma, H. Yin, M.T. Dove, Accounting for instrument resolution in the pair distribution functions obtained from neutron time-of-flight total scattering data using Hermite functions 1, *Principles* (2022) (in preparation).
- [36] GEM, <https://www.isis.stfc.ac.uk/Pages/gem.aspx> (Accessed: 17 July 2022).
- [37] D.C. Palmer, Visualization and analysis of crystal structures using CrystalMaker software, *Z. für Kristallogr. - Cryst. Mater.* 230 (2015) 559–572.
- [38] J.D. Gale, GULP: a computer program for the symmetry-adapted simulation of solids, *J. Chem. Soc., Faraday Trans.* 93 (1997) 629–637.
- [39] J.D. Gale, A.L. Rohl, The General Utility Lattice Program (GULP), *Mol. Simulat.* 29 (2003) 291–341.
- [40] E.R. Cope, M.T. Dove, Pair distribution functions calculated from interatomic potential models using the General Utility Lattice Program, *J. Appl. Crystallogr.* 30 (2007) 589–594.
- [41] E.R. Cope, M.T. Dove, Evaluation of domain models for  $\beta$ -cristobalite from the pair distribution function, *J. Phys. Condens. Matter* 22 (2010), 125401.
- [42] A.L. Goodwin, M.G. Tucker, E.R. Cope, M.T. Dove, D.A. Keen, Model-independent extraction of dynamical information from powder diffraction data, *Phys. Rev. B* 72 (2005), 214304.
- [43] L. Tan, A.J. Misquitta, A. Sapelkin, L. Fang, R.M. Wilson, D.S. Keeble, B. Zhang, T. Zhu, F.S. Riehle, S. Han, K. Yu, M.T. Dove, X-ray total scattering study of magic-size clusters and quantum dots of cadmium sulphide, *Nanoscale* 11 (2019) 21900–21908.
- [44] Neutronsources.org, Your entry into the neutron world <https://neutronsources.org>. (Accessed: 30 July 2022).
- [45] T.E. Mason, T.J. Gawne, S.E. Nagler, M.B. Nestor, J.M. Carpenter, The early development of neutron diffraction: science in the wings of the Manhattan Project, *Acta Crystallogr. A* (2012) 37–44.

- [46] J. Chadwick, Possible existence of a neutron, *Nature* 129 (1932) 312.
- [47] D.P. Mitchell, P.N. Powers, Bragg reflection of slow neutrons, *Phys. Rev.* 50 (1936) 486–487.
- [48] B. Willis, C. Carlike, *Experimental Neutron Scattering*, Oxford University Press, Oxford, UK, 2009.
- [49] J. Carpenter, C. Loong, *Elements of Slow-Neutron Scattering*, Cambridge University Press, Cambridge, UK, 2015.
- [50] A. Boothroyd, *Principles of Neutron Scattering from Condensed Matter*, Oxford University Press, Oxford, UK, 2020.
- [51] C. Carlike, ILL in the changing international context, *Phys. B: Condens. Matter* 385–386 (2006) 961–965.
- [52] C. Alba-Simionesco, A. Menelle, J.-P. Visticot, The Laboratoire Léon Brillouin and the Orphée Reactor: The French National Neutron Facility, *Neutron News* 22 (2011) 10–13.
- [53] H. Fischer, G. Cuello, P. Palleau, D. Feltin, A. Barnes, Y. Badyal, J. Simonson, D4c: A very high precision diffractometer for disordered materials, *Appl. Phys. A* 74 (2002) S160–S162.
- [54] *Disordered materials diffractometer: D4* <https://www.ill.eu/users/instruments/instruments-list/d4>, (Accessed: 17 July 2022).
- [55] G.J. Cuello, J. Darpentigny, L. Hennen, L. Cormier, J. Dupont, B. Homatter, B. Beuneu, 7C2, the new neutron diffractometer for liquids and disordered materials at LLB, *J. Phys. Conf.* 746 (2016), 012020.
- [56] W. Wagner, Y. Dai, H. Glasbrenner, M. Grosse, E. Lehmann, Status of SINQ, the only MW spallation neutron source—highlighting target development and industrial applications, *Nucl. Instrum. Methods Phys. Res. Sect. A: Accel. Spectrom. Detect. Assoc. Equip.* 562 (2006) 541–547.
- [57] W. Wagner, J. Mesot, P. Allenspach, G. Kuehne, H. Rønnow, The Swiss spallation neutron source SINQ – developments and upgrades for optimized user service, *Phys. B: Condens. Matter* 385–386 (2006) 968–971.
- [58] B. Blau, K.N. Clausen, S. Gvasaliya, M. Janoschek, S. Janssen, L. Keller, B. Roessli, J. Schefer, P. Tregenna-Piggott, W. Wagner, O. Zaharko, The Swiss Spallation Neutron Source SINQ at Paul Scherrer Institut, *Neutron News* 20 (2009) 5–8.
- [59] T. Geue, F. Juranyi, C. Niedermayer, J. Kohlbrecher, J. Stahn, U. Gasser, M. Yamada, C. Klausner, M. Kenzelmann, C. Rüegg, U. Filges, SINQ—Performance of the new neutron delivery system, *Neutron News* 32 (2021) 37–43.
- [60] Y. Ishikawa, Studies of condensed matter with a pulsed neutron source (KENS), *Phys. B+C* 120 (1983) 3–14.
- [61] M. Furusaka, KENS neutron scattering facility, *Neutron News* 3 (1992) 8–14.
- [62] K. Crawford, The Intense Pulsed Neutron Source, *Neutron News* 1 (1990) 9–15.
- [63] R. Teller, J. Richardson, J. Carpenter, Correspondent's Report: The Intense Pulsed Neutron Source at Argonne National Laboratory, *Neutron News* 15 (2004) 9–13.
- [64] R. Teller, J. Carpenter, B. Brown, G. Lander, Closure of IPNS at Argonne—The end of an era, *Neutron News* 19 (2008) 24–27.
- [65] C.C. Wilson, ISIS, the UK spallation neutron source – a guided tour, *Neutron News* 1 (1990) 14–19.
- [66] C.C. Wilson, A guided tour of ISIS – the UK spallation neutron source, *Neutron News* 6 (1995) 27–34.
- [67] J. Penfold, Scientific review: ISIS second target station: Overview and progress, *Neutron News* 15 (2004) 9–12.
- [68] D. J. S. Findlay, ISIS – pulsed neutron and muon source, in: 2007 IEEE Particle Accelerator Conference (PAC), pp. 695–699.
- [69] J. Thomson, The ISIS spallation neutron and muon source – the first thirty-three years, *Nucl. Instrum. Methods Phys. Res. Sect. A: Accel. Spectrom. Detect. Assoc. Equip.* 917 (2019) 61–67.
- [70] Lujan Center at LANSCE, <https://lansce.lanl.gov/facilities/lujan/> (Accessed: 3 August 2022).
- [71] J.A. Goldstone, The Manuel Lujan, Jr. Neutron Scattering Center (LANSCE), *Neutron News* 2 (1991) 7–13.
- [72] J.A. Roberts, The Los Alamos Neutron Science Center (LANSCE), *Neutron News* 10 (1999) 11–14.
- [73] T. Mason, D. Abernathy, I. Anderson, J. Ankner, T. Egami, G. Ehlers, A. Ekkebus, G. Granroth, M. Hagen, K. Herwig, J. Hodges, C. Hoffmann, C. Horak, L. Horton, F. Klose, J. Larese, A. Mesecar, D. Myles, J. Neufeld, M. Ohl, C. Tulk, X.-L. Wang, J. Zhao, The Spallation Neutron Source in Oak Ridge: A powerful tool for materials research, 385–386, *Phys. B: Condens. Matter* (2006) 955–960.
- [74] G. Ehlers, M.L. Crow, Y. Diawara, F.X. Gallmeier, X. Geng, G.E. Granroth, R.D. Gregory, F.F. Islam, R.O. Knudson, F. Li, M.S. Loyd, B. Vacaliuc, Modern trends in neutron scattering instrument technologies, *Instruments* 6 (2022).
- [75] Y. Fujii, Overview on neutron sources in Japan, *Nucl. Instrum. Methods Phys. Res. Sect. A: Accel. Spectrom. Detect. Assoc. Equip.* 529 (2004) 1–4.
- [76] M. Arai, F. Maekawa, Japan Spallation Neutron Source (JSNS) of J-PARC, *Nucl. Phys. News* 19 (2009) 34–39.
- [77] M. Futakawa, F. Maekawa, S. Sakamoto, 1-MW Pulsed Spallation Neutron Source (JSNS) at J-PARC, *Neutron News* 22 (2011) 15–19.
- [78] T. Kamiyama, K. Suzuya, Neutron instruments at J-PARC: Toward the state-of-the-art facility, *Neutron News* 22 (2011) 20–25.
- [79] J. Wei, H. Chen, Y. Chen, Y. Chen, Y. Chi, C. Deng, H. Dong, L. Dong, S. Fang, J. Feng, S. Fu, L. He, W. He, Y. Heng, K. Huang, X. Jia, W. Kang, X. Kong, J. Li, T. Liang, G. Lin, Z. Liu, H. Ouyang, Q. Qin, H. Qu, C. Shi, H. Sun, J. Tang, J. Tao, C. Wang, F. Wang, D. Wang, Q. Wang, S. Wang, T. Wei, J. Xi, T. Xu, Z. Xu, W. Yin, X. Yin, J. Zhang, Z. Zhang, Z. Zhang, M. Zhou, T. Zhu, China Spallation Neutron Source: Design, R&D, and outlook, *Nucl. Instrum. Methods Phys. Res. Sect. A: Accel. Spectrom. Detect. Assoc. Equip.* 600 (2009) 10–13.
- [80] F. Wang, T. Liang, W. Yin, Q. Yu, L. He, J. Tao, T. Zhu, X. Jia, S. Zhang, Physical design of target station and neutron instruments for China Spallation Neutron Source, *Sci. China Phys. Mech. Astron.* 56 (2013) 2410–2424.
- [81] H. Chen, X.L. Wang, China's first pulsed neutron source, *Nat. Mater.* 15 (2016) 689–691.
- [82] S.N. Fu, H.S. Chen, Y.B. Chen, L. Ma, F.W. Wang, CSNS Project Construction, *J. Phys. Conf.* 1021 (2018), 012002.
- [83] J.B. Hayter, C.D. West, Status of the advanced neutron source project, *Neutron News* 3 (1992) 16–19.
- [84] High Flux Isotope Reactor. <https://www.ornl.gov/project/hfir>, (Accessed: 23 October 2022).
- [85] J. Rumsey, A history of neutron scattering at ORNL, *Neutron News* 29 (2018) 10–16.
- [86] J.M. Carpenter, Pulsed spallation neutron sources for slow neutron scattering, *Nucl. Instrum. Methods* 145 (1977) 91–113.
- [87] A. Ellison, R. Crawford, D. Montague, K. Volin, D. Price, The New Glass, Liquids and Amorphous Materials Diffractometer (GLAD) at IPNS, *J. Neutron Res.* 1 (1993) 61–70.
- [88] T. Proffen, T. Egami, S. Billinge, A. Cheetham, D. Louca, J.B. Parise, Building a high resolution total scattering powder diffractometer – upgrade of NPD at MLNSC, *Appl. Phys. A* 74 (2002) S163–S165.
- [89] J. Xu, L. Mei, W. Yin, X. Wang, W. Cai, Z. Li, T. Bo, H. Chen, B. Wang, Y. Chen, Physical design of multipurpose physics neutron diffractometer for the CSNS, *Nucl. Instrum. Methods Phys. Res. Sect. A: Accel. Spectrom. Detect. Assoc. Equip.* 927 (2019) 161–168.
- [90] J. Xu, Y. Xia, Z. Li, H. Chen, X. Wang, Z. Sun, W. Yin, Multi-physics instrument: Total scattering neutron time-of-flight diffractometer at China Spallation Neutron Source, in: *Nucl. Instrum. Methods Phys. Res. A: Accel. Spectrom. Detect. Assoc. Equip.*, vol. 1013, 2021, 165642. Spectrometers, Detectors and Associated Equipment.
- [91] J. Chen, L. Kang, H. Lu, P. Luo, F. Wang, L. He, The general purpose powder diffractometer at CSNS, *Physica B: Phys. Condens. Matter* 551 (2018) 370–372.
- [92] R.L. Smith, S. Hull, M.G. Tucker, H.Y. Playford, D.J. McPhail, S.P. Waller, S.T. Norberg, The upgraded Polaris powder diffractometer at the ISIS neutron source, *Rev. Sci. Instrum.* 90 (2019), 115101.
- [93] POLARIS, <https://www.isis.stfc.ac.uk/Pages/polaris.aspx>. (Accessed: 17 July 2022).
- [94] P. Day, J. Enderby, W. Williams, L. Chapon, A. Hannon, P. Radaelli, A. Soper, Scientific reviews: GEM: the general materials diffractometer at ISIS—multibank capabilities for studying crystalline and disordered materials, *Neutron News* 15 (2004) 19–23.
- [95] A.K. Soper, Future perspectives for liquids and amorphous materials at ISIS, in: D.K. Hyer (Ed.), *Advanced Neutron Sources 1988*, vol. 97 of IOP Conference Series, Institute of Physics, Bristol, UK, 1989, pp. 353–366.
- [96] A.K. Soper, First Results from SANDALS - the Small Angle Neutron Diffractometer for Amorphous and Liquid Samples at ISIS, in: M. Misawa, M. Furusaka, H. Ikeda, N. Watanabe (Eds.), *ICANS-XI International Collaboration on Advanced Neutron Sources*, KEK, Tsukuba, Japan, 1990, pp. 809–819.
- [97] SANDALS, <https://www.isis.stfc.ac.uk/Pages/sandals.aspx>. (Accessed: 17 July 2022).
- [98] NIMROD, <https://www.isis.stfc.ac.uk/Pages/nimrod.aspx>. (Accessed: 17 July 2022).
- [99] D.T. Bowron, A.K. Soper, K. Jones, S. Ansell, S. Birch, J. Norris, L. Perrott, D. Riedel, N.J. Rhodes, S.R. Wakefield, A. Botti, M.-A. Ricci, F. Grazzi, M. Zoppi, NIMROD: The Near and Intermediate Range Order Diffractometer of the ISIS second target station, *Rev. Sci. Instrum.* 81 (2010), 033905.
- [100] K. Andersen, D. Argyriou, A. Jackson, J. Houston, P. Henry, P. Deen, R. Toft-Petersen, P. Beran, M. Strobl, T. Arnold, H. Wacklin-Knecht, N. Tsapatsaris, E. Oksanen, R. Woracek, W. Schwaika, D. Mannix, A. Hiess, S. Kennedy, O. Kirstein, S. Petersson Årsköld, J. Taylor, M. Hagen, G. Laszlo, K. Kanaki, F. Piscitelli, A. Khaplanov, I. Stefanescu, T. Kittelmann, D. Pfeiffer, R. Hall-Wilton, C. Lopez, G. Aprigliano, L. Whitelegg, F. Moreira, M. Olsson, H. Bordallo, D. Martín-Rodríguez, H. Schneider, M. Sharp, M. Hartl, G. Nagy, S. Ansell, S. Pullen, A. Vickery, A. Fedrigo, F. Mezei, M. Arai, R. Heenan, W. Halcrow, D. Turner, D. Raspino, A. Orszulik, J. Cooper, N. Webb, J. Galsworthy, J. Nightingale, S. Langridge, J. Elmer, H. Frielinghaus, R. Hanslik, A. Gussen, S. Jaksch, R. Engels, T. Kozielski, S. Butterweck, M. Feygenson, P. Harbott, A. Poqué, A. Schwaab, K. Lieutenant, N. Violini, J. Voigt, T. Brückel, M. Koenen, H. Kämmerling, E. Babcock, Z. Salhi, A. Wischniewski, A. Heynen, S. Désert, J. Jestin, F. Porcher, X. Fabrèges, G. Fabrèges, B. Annghöfer, S. Klimko, T. Dupont, T. Robillard, A. Goukassov, S. Longeville, C. Alba-Simionesco, P. Bourges, J. Guyon Le Bouffé, P. Lavie, S. Rodrigues, E. Calzada, M. Lerche, B. Schillinger, P. Schmakat, M. Schulz, M. Seifert, W. Lohstroh, W. Petry, J. Neuhaus, L. Loaiza, A. Tartagliano, A. Glavic, S. Schütz, J. Stahn, E. Lehmann, M. Morgano, J. Schefer, U. Filges, C. Klausner, C. Niedermayer, J. Fenske, G. Nowak, M. Rouijaa, D. Siemers, R. Kiehn, M. Müller, H. Carlsen, L. Udby, K. Lefmann, J. Birk, S. Holm-Dahlin, M. Bertelsen, U.B. Hansen, M. Olsen, M. Christensen, K. Iversen, N. Christensen, H. Rønnow, P. Freeman, B. Hauback, R. Kolevato, I. Llamas-Jansa, A. Orecchini, F. Sacchetti, C. Petrillo, A. Paciaroni, P. Tozzi, M. Zanatta, P. Luna, I. Herranz, O. del Moral, M. Huerta, M. Magán, M. Mosconi, E. Abad, J. Aguilar, S. Stepanyan, G. Bakedano, R. Vivanco, I. Bustinduy, F. Sordo, J. Martínez, R. Lechner, F. Villacorta, J. Šaroun, P. Lukáš, M. Markó, M. Zanetti, S. Bellissima, L. del Rosso, F. Masi, C. Bovo, M. Chowdhury, A. De Bonis, L. Di Fresco, C. Scatigno, S. Parker, F. Fernandez-Alonso, D. Colognesi, R. Senesi, C. Andreani, G. Gorini, G. Scionti, A. Schreyer, The instrument suite of the European Spallation Source, *Nucl. Instrum. Methods Phys. Res. Sect. A: Accel. Spectrom. Detect. Assoc. Equip.* 957 (2020), 163402.
- [101] J. Neufeld, M. Feygenson, J. Carruth, R. Hoffmann, K.K. Chipley, The Nanoscale Ordered Materials Diffractometer NOMAD at the Spallation Neutron Source SNS,

- Nucl. Instrum. Methods Phys. Res. Sect. B: Beam Interact. Mater. Atoms 287 (2012) 68–75.
- [102] Nanoscale-Ordered Materials Diffractometer, <https://neutrons.ornl.gov/nomad>. (Accessed: 17 July 2022).
- [103] A. Huq, M. Kirkham, P.F. Peterson, J.P. Hodges, P.S. Whitfield, K. Page, T. Hugle, E.B. Iverson, A. Parizzi, G. Rennich, POWGEN: rebuild of a third-generation powder diffractometer at the Spallation Neutron Source, J. Appl. Crystallogr. 52 (2019) 1189–1201.
- [104] BL21 NOVA high intensity total diffractometer. <https://mlfinfo.jp/en/bl21>. (Accessed: 17 July 2022).
- [105] LightSources.org, 75 years of science with synchrotron light. <https://www.lightsources.org>. Accessed: 30 July 2022.
- [106] ISIS and the China Spallation Neutron Source agree new partnership, <https://www.isis.stfc.ac.uk/Pages/ISIS-and-the-China-Spallation-Neutron-Source-agree-new-partnership.aspx>. (Accessed: 28 July 2022).
- [107] D.T. Bowron, A.K. Soper, Taking atomistic insight into the nanoscale: Nimrod, the Near and Intermediate Range Order Diffractometer, Neutron News 22 (2011) 12–14.
- [108] F.R. Elder, A.M. Gurewitsch, R.V. Langmuir, H.C. Pollock, Radiation from electrons in a synchrotron, Phys. Rev. 71 (1947) 829–830.
- [109] H.C. Pollock, The discovery of synchrotron radiation, Am. J. Phys. 51 (1983) 278–280.
- [110] T. Connolly, C.M. Beavers, P. Chater, High-energy adventures at Diamond Light Source, Synchrotron Radiat. News 33 (2020) 31–36.
- [111] XPDF (115-1), <https://www.diamond.ac.uk/Instruments/Crystallography/I115-1.html>. (Accessed: 30 July 2022).
- [112] G. Confalonieri, M. Dapaggi, M. Sommariva, M. Gateshki, A.N. Fitch, A. Bernasconi, Comparison of total scattering data from various sources: the case of a nanometric spinel, Powder Diff. 30 (2015) S65–S69.
- [113] T.D. Bennett, A.L. Goodwin, M.T. Dove, D.A. Keen, M.G. Tucker, E.R. Barney, A.K. Soper, E.G. Bithell, J.-C. Tan, A.K. Cheetham, Structure and properties of an amorphous metal-organic framework, Phys. Rev. Lett. 104 (2010), 115503.
- [114] M.T. Dunstan, S.A. Maugeri, W. Liu, M.G. Tucker, O.O. Taiwo, B. Gonzalez, P.K. Allan, M.W. Gaultois, P.R. Shearing, D.A. Keen, A.E. Phillips, M.T. Dove, S.A. Scott, J.S. Dennis, C.P. Grey, In situ studies of materials for high temperature CO<sub>2</sub> capture and storage, Faraday Discuss 192 (2016) 217–240.
- [115] B. Zhang, T. Zhu, M. Ou, N. Rowell, H. Fan, J. Han, L. Tan, M.T. Dove, Y. Ren, X. Zuo, S. Han, J. Zeng, K. Yu, Thermally-induced reversible structural isomerization in colloidal semiconductor CdS magic-size clusters, Nat. Commun. 9 (2018) 2499.
- [116] C.L. Farrow, P. Juhas, J.W. Liu, D. Bryndin, E.S. Bozin, J. Bloch, T. Proffen, S.J.L. Billinge, PDFfit2 and PDFgui: computer programs for studying nanostructure in crystals, J. Phys. Condens. Matter 19 (2007), 335219.
- [117] M.A. Howe, R.L. McGreevy, W.S. Howells, The analysis of liquid structure data from time-of-flight neutron diffraction, J. Phys. Condens. Matter 1 (1989) 3433.
- [118] A.K. Soper, GudrunN and GudrunX: programs for correcting raw neutron and X-ray diffraction data to differential scattering cross section, Technical Report RAL-TR-2011-013, ISIS Facility, Rutherford Appleton Laboratory, 2011.
- [119] A.K. Soper, E.R. Barney, Extracting the pair distribution function from white-beam X-ray total scattering data, J. Appl. Crystallogr. 44 (2011) 1–13.
- [120] V.F. Sears, Neutron scattering lengths and cross sections, Neutron News 3 (1992) 26–37.
- [121] Neutron scattering lengths and cross sections, <https://www.ncnr.nist.gov/resources/n-lengths/>. (Accessed: 22 July 2022).
- [122] M.T. Dove, M.G. Tucker, D.A. Keen, Neutron total scattering method: simultaneous determination of long-range and short-range order in disordered materials, Eur. J. Mineral 14 (2002) 331–348.
- [123] G. Placzek, The scattering of neutrons by systems of heavy nuclei, Phys. Rev. 86 (1952) 377–388.
- [124] E. Guarini, The neutron double differential cross-section of simple molecular fluids: refined computing models and nowadays applications, J. Phys. Condens. Matter 15 (2003) R775–R812.
- [125] P.S. Salmon, I. Petri, P.H.K. de Jong, P. Verkerk, H.E. Fischer, W.S. Howells, Structure of liquid lithium, J. Phys. Condens. Matter 16 (2004) 195–222.
- [126] H.E. Fischer, A.C. Barnes, P.S. Salmon, Neutron and x-ray diffraction studies of liquids and glasses, Rep. Prog. Phys. 69 (2005) 233–299.
- [127] A. Soper, Inelasticity corrections for time-of-flight and fixed wavelength neutron diffraction experiments, Mol. Phys. 107 (2009) 1667–1684.
- [128] P.F. Peterson, M. Gutmann, T. Proffen, S.J.L. Billinge, PDFgetN: a user-friendly program to extract the total scattering structure factor and the pair distribution function from neutron powder diffraction data, J. Appl. Crystallogr. 33 (2000) 1192.
- [129] P. Juhás, J.N. Louwen, L. van Eijck, E.T.C. Vogt, S.J.L. Billinge, PDFgetN3: atomic pair distribution functions from neutron powder diffraction data using *ad hoc* corrections, J. Appl. Crystallogr. 51 (2018) 1492–1497.
- [130] S.J.L. Billinge, C.L. Farrow, Towards a robust *ad hoc* data correction approach that yields reliable atomic pair distribution functions from powder diffraction data, J. Phys. Condens. Matter 25 (2013), 454202.
- [131] A.K. Soper, E.R. Barney, On the use of modification functions when Fourier transforming total scattering data, J. Appl. Crystallogr. 45 (2012) 1314–1317.
- [132] P. Juhás, T. Davis, C.L. Farrow, S.J.L. Billinge, PDFgetX3: a rapid and highly automatable program for processing powder diffraction data into total scattering pair distribution functions, J. Appl. Crystallogr. 46 (2013) 560–566.
- [133] J.H. Konnert, J. Karle, The computation of radial distribution functions for glassy materials, Acta Crystallogr. A 29 (1973) 702–710.
- [134] D. Wendt, E. Bozin, J. Neuefeind, K. Page, W. Ku, L. Wang, B. Fultz, A.V. Tkachenko, I.A. Zaliznyak, Entropic elasticity and negative thermal expansion in a simple cubic crystal, Sci. Adv. 5 (2019), eaay2748.
- [135] A.C. Wright, A.G. Clare, D.I. Grimley, R.N. Sinclair, Neutron scattering studies of network glasses, J. Non-Cryst. Solids 112 (1989) 33–47.
- [136] L.B. McCusker, R.B.V. Dreele, D.E. Cox, D. Louer, P. Scardi, Rietveld refinement guidelines, J. Appl. Crystallogr. 32 (1999) 36–50.
- [137] X. Qiu, T. Proffen, J.F. Mitchell, S.J.L. Billinge, Orbital correlations in the pseudocubic O and rhombohedral R phases of LaMnO<sub>3</sub>, Phys. Rev. Lett. 94 (2005), 177203.
- [138] E.S. Bozin, M. Schmidt, A.J. DeConinck, G. Paglia, J.F. Mitchell, T. Chatterji, P.G. Radaelli, T. Proffen, S.J.L. Billinge, Understanding the insulating phase in colossal magnetoresistance manganites: Shortening of the Jahn-Teller long-bond across the phase diagram of La<sub>1-x</sub>Ca<sub>x</sub>MnO<sub>3</sub>, Phys. Rev. Lett. 98 (2007), 137203.
- [139] T. Proffen, Neutron total scattering analysis of nanoparticles, JOM 64 (2012) 112–116.
- [140] T. Proffen, S.J.L. Billinge, PDFFIT, a program for full profile structural refinement of the atomic pair distribution function, J. Appl. Crystallogr. 32 (1999) 572–575.
- [141] PDFgui, <https://www.diffpy.org/products/pdfgui.html>. (Accessed: 17 October 2022).
- [142] Topas Academic. <http://www.topas-academic.net>. (Accessed: 17 October 2022).
- [143] T.A. Bird, A. Herlihy, M.S. Senn, Symmetry-adapted pair distribution function analysis (SAPA): a novel approach to evaluating lattice dynamics and local distortions from total scattering data, J. Appl. Crystallogr. 54 (2021) 1514–1520.
- [144] T.A. Bird, J. Woodland-Scott, L. Hu, M.T. Wharmby, J. Chen, A.L. Goodwin, M.S. Senn, Anharmonicity and scissoring modes in the negative thermal expansion materials ScF<sub>3</sub> and CaZrF<sub>6</sub>, Phys. Rev. B 101 (2020), 064306.
- [145] T.A. Bird, M.G.L. Wilkinson, D.A. Keen, R.I. Smith, N.C. Bristowe, M.T. Dove, A.E. Phillips, M.S. Senn, Soft-mode anisotropy in the negative thermal expansion material ReO<sub>3</sub>, Phys. Rev. B 104 (2021), 214102.
- [146] A. Herlihy, T.A. Bird, C.J. Ridley, C.L. Bull, N.P. Funnell, M.S. Senn, Recovery of harmonic-like behavior of the polar mode in BaTiO<sub>3</sub> at high pressures, Phys. Rev. B 105 (2022), 094114.
- [147] R.L. McGreevy, L. Pusztai, Reverse Monte Carlo simulation: A new technique for the determination of disordered structures, Mol. Simulat. 1 (1988) 359–367.
- [148] R.L. McGreevy, M.A. Howe, RMC: Modeling disordered structures, Annu. Rev. Mater. Sci. 22 (1992) 217–242.
- [149] L. Pusztai, Structural modelling using the reverse Monte Carlo technique: Application to amorphous semiconductors, J. Non-Cryst. Solids 227–230 (1998) 88–95.
- [150] R.L. McGreevy, Reverse Monte Carlo modelling, J. Phys. Condens. Matter 13 (2001) R877–R913.
- [151] D.A. Keen, M.G. Tucker, M.T. Dove, Reverse Monte Carlo modelling of crystalline disorder, J. Phys. Condens. Matter 17 (2005), S15–S22.
- [152] M.G. Tucker, D.A. Keen, M.T. Dove, A.L. Goodwin, Q. Hui, RMCProfile: reverse Monte Carlo for polycrystalline materials, J. Phys. Condens. Matter 19 (2007), 335218.
- [153] A. Mellergård, R.L. McGreevy, Reverse Monte Carlo modelling of neutron powder diffraction data, Acta Crystallogr. A 55 (1999) 783–789.
- [154] A. Mellergård, R. McGreevy, Recent developments of the rmcpow method for structural modelling, Chem. Phys. 261 (2000) 267–274.
- [155] O. Gereben, P. Jónvári, L. Temleitner, L. Pusztai, A new version of the RMC++ Reverse Monte Carlo programme, aimed at investigating the structure of covalent glasses, J. Optoelectron. Adv. Mater. 9 (2007) 3021–3027.
- [156] O. Gereben, L. Pusztai, Extension of the invariant environment refinement technique + reverse Monte Carlo method of structural modelling for interpreting experimental structure factors: The cases of amorphous silicon, phosphorus, and liquid argon, J. Chem. Phys. 135 (2011), 084111.
- [157] O. Gereben, L. Pusztai, RMC\_POT, a computer code for Reverse Monte Carlo modeling the structure of disordered systems containing molecules of arbitrary complexity, J. Comput. Chem. 33 (2012) 2285–2291.
- [158] A. Soper, Empirical potential Monte Carlo simulation of fluid structure, Chem. Phys. 202 (1996) 295–306.
- [159] A.K. Soper, Tests of the empirical potential structure refinement method and a new method of application to neutron diffraction data on water, Mol. Phys. 99 (2001) 1503–1516.
- [160] A.K. Soper, Partial structure factors from disordered materials diffraction data: An approach using empirical potential structure refinement, Phys. Rev. B 72 (2005), 104204.
- [161] M. Falkowska, D.T. Bowron, H.G. Manyar, C. Hardacre, T.G.A. Youngs, Neutron scattering of aromatic and aliphatic liquids, ChemPhysChem 17 (2016) 2043–2055.
- [162] T.-L. Hughes, M. Falkowska, M. Leutzsch, A.J. Sederman, M.D. Mantle, T.F. Headen, T.G.A. Youngs, D.T. Bowron, C. Hardacre, Bulk and confined benzene-cyclohexane mixtures studied by an integrated total neutron scattering and NMR method, Top. Catal. 64 (2021) 722–734.
- [163] A.K. Soper, D.T. Bowron, Adsorption of simple gases into the porous glass MCM-41, J. Chem. Phys. 154 (2021), 184503.
- [164] R. Hargreaves, D.T. Bowron, K. Edler, Atomistic structure of a micelle in solution determined by wide Q-range neutron diffraction, J. Am. Chem. Soc. 133 (2011) 16524–16536.
- [165] D.T. Bowron, K.J. Edler, Decyltrimethylammonium bromide micelles in acidic solutions: Counterion binding, water structuring, and micelle shape, Langmuir 33 (2017) 262–271.



- [166] T. Youngs, Dissolve: next generation software for the interrogation of total scattering data by empirical potential generation, *Mol. Phys.* 117 (2019) 3464–3477.
- [167] C. Ma, H. Cheng, T. Zuo, G. Jiao, Z. Han, H. Qin, NeuDATool: an open source neutron data analysis tools, supporting GPU hardware acceleration, and across-computer cluster nodes parallel, *Chin. J. Chem. Phys.* 33 (2020) 727–732.
- [168] M. Dove, D. Keen, A. Hannon, I. Swainson, Direct measurement of the Si–O bond length and orientational disorder in the high-temperature phase of cristobalite, *Phys. Chem. Miner.* 24 (1997) 311–317.
- [169] L. Hu, J. Chen, A. Sanson, H. Wu, C.G. Rodriguez, L. Olivi, Y. Ren, L. Fan, J. Deng, X. Xing, New insights into the negative thermal expansion: Direct experimental evidence for the “guitar-string” effect in cubic  $\text{ScF}_3$ , *J. Am. Chem. Soc.* 138 (2016) 8320–8323.
- [170] A.C. Wright, Diffraction studies of glass structure, *J. Non-Cryst. Solids* 123 (1990) 129–148.
- [171] G. Cai, H. Lin, Z. Zhao, J. Liu, A.E. Phillips, T.F. Headen, T.G. Youngs, Y. Hai, H. Tian, C. He, Y. Ke, J. Tao, T. Ben, M.T. Dove, Atomic structure of the continuous random network of amorphous  $\text{C}[(\text{C}_6\text{H}_4)_2]_2$  PAF-1, *Cell Rep. Phys. Sci.* 3 (2022), 100899.
- [172] R. Riedel, A. Greiner, G. Miehe, W. Dressler, H. Fuess, J. Bill, F. Aldinger, The first crystalline solids in the ternary Si–C–N system, *Angew. Chem. Int. Ed. Engl.* 36 (1997) 603–606.
- [173] R. Riedel, E. Kroke, A. Greiner, A.O. Gabriel, L. Ruwisch, J. Nicolich, P. Kroll, Inorganic solid-state chemistry with main group element carbodiimides, *Chem. Mater.* 10 (1998) 1–16.
- [174] P. Kroll, R. Riedel, R. Hoffmann, Silylated carbodiimides in molecular and extended structures, *Phys. Rev. B* 60 (1999) 3126–3139.
- [175] L. Li, K. Refson, M.T. Dove, Negative thermal expansion of cubic silicon dicarbodiimide,  $\text{Si}(\text{NCN})_2$ , studied by ab initio lattice dynamics, *J. Phys. Condens. Matter* 32 (2020), 465402.
- [176] A.L. Goodwin, C. Kepert, Negative thermal expansion and low-frequency modes in cyanide-bridged framework materials, *Phys. Rev. B* 71 (2005), 140301.
- [177] K.S. Park, Z. Ni, A.P. Cote, J.Y. Choi, R. Huang, F.J. Uribe-Romo, H.K. Chae, M. O’Keeffe, O.M. Yaghi, Exceptional chemical and thermal stability of zeolitic imidazolate frameworks, *Proc. Natl. Acad. Sci. USA* 103 (2006) 10186–10191.
- [178] T. Ben, H. Ren, S. Ma, D. Cao, J. Lan, X. Jing, W. Wang, J. Xu, F. Deng, J.M. Simmons, S. Qiu, G. Zhu, Targeted synthesis of a porous aromatic framework with high stability and exceptionally high surface area, *Angew. Chem. Int. Ed.* 48 (2009) 9457–9460.
- [179] S.R. Elliott, The origin of the first sharp diffraction peak in the structure factor of covalent glasses and liquids, *J. Phys. Condens. Matter* 4 (1999) 7661–7678.
- [180] C. Massobrio, A. Pasquarello, Origin of the first sharp diffraction peak in the structure factor of disordered network-forming systems: Layers or voids? *J. Chem. Phys.* 114 (2001) 7976–7979.
- [181] J. Du, L.R. Corrales, First sharp diffraction peak in silicate glasses: Structure and scattering length dependence, *Phys. Rev. B* 72 (2005), 092201.
- [182] G. Lucovsky, J.C. Phillips, Nano-regime length scales extracted from the first sharp diffraction peak in non-crystalline  $\text{SiO}_2$  and related materials: Device applications, *Nanoscale Res. Lett.* 5 (2010) 550–558.
- [183] M. Micoulaut, M. Bauchy, Anomalies of the first sharp diffraction peak in network glasses: Evidence for correlations with dynamic and rigidity properties, *Phys. Status Solidi B* 250 (2013) 976–982.
- [184] M.T.M. Shatnawi, The first sharp diffraction peak in the total structure function of amorphous chalcogenides: Anomalous characteristics and controversial views, *New J. Glass Ceram.* 6 (2016) 37–46.
- [185] B.E. Warren, H. Krutter, O. Morningstar, Fourier analysis of x-ray patterns of vitreous  $\text{SiO}_2$  and  $\text{B}_2\text{O}_3$ , *J. Am. Ceram. Soc.* 19 (1936) 202–206.
- [186] B.E. Warren, J. Bisce, The structure of silica glass by x-ray diffraction studies, *J. Am. Ceram. Soc.* 21 (1938) 49–54.
- [187] B.K. Greve, K.L. Martin, P.L. Lee, P.J. Chupas, K.W. Chapman, A.P. Wilkinson, Pronounced negative thermal expansion from a simple structure: cubic  $\text{ScF}_3$ , *J. Am. Chem. Soc.* 132 (2010) 15496–15498.
- [188] K.D. Hammonds, M.T. Dove, A.P. Giddy, V. Heine, B. Winkler, Rigid-unit phonon modes and structural phase transitions in framework silicates, *Am. Mineral.* 81 (1996) 1057–1079.
- [189] M.T. Dove, Flexibility of network materials and the Rigid Unit Mode model: a personal perspective, *Phil. Trans. Math. Phys. Eng. Sci.* 377 (2019), 20180222.
- [190] V. Heine, P.R.L. Welche, M.T. Dove, Geometrical origin and theory of negative thermal expansion in framework structures, *J. Am. Ceram. Soc.* 82 (1999) 1793–1802.
- [191] C.W. Li, X. Tang, J.A. Muñoz, J.B. Keith, S.J. Tracy, D.L. Abernathy, B. Fultz, Structural relationship between negative thermal expansion and quartic anharmonicity of cubic  $\text{ScF}_3$ , *Phys. Rev. Lett.* 107 (2011), 195504.
- [192] K.W. Chapman, P.J. Chupas, C.J. Kepert, Direct observation of a transverse vibrational mechanism for negative thermal expansion in  $\text{Zn}(\text{CN})_2$ : an atomic pair distribution function analysis, *J. Am. Chem. Soc.* 127 (2005) 15630–15636.
- [193] S.J. Hibble, A.M. Chippindale, E. Marelli, S. Kroeker, V.K. Michaelis, B.J. Greer, P.M. Aguiar, E.J. Bilbé, E.R. Barney, A.C. Hannon, Local and average structure in zinc cyanide: toward an understanding of the atomistic origin of negative thermal expansion, *J. Am. Chem. Soc.* 135 (2013) 16478–16489.
- [194] S.J. Hibble, S.M. Cheyne, A.C. Hannon, S.G. Eversfield, Beyond Bragg scattering: the structure of  $\text{AgCN}$  determined from total neutron diffraction, *Inorg. Chem.* 41 (2002) 1042–1044.
- [195] S.J. Hibble, A.C. Hannon, S.M. Cheyne, Structure of  $\text{AuCN}$  determined from total neutron diffraction, *Inorg. Chem.* 42 (2003) 4724–4730.
- [196] S.J. Hibble, A.M. Chippindale, A.H. Pohl, A.C. Hannon, Surprises from a simple material—the structure and properties of nickel cyanide, *Angew. Chem. Int. Ed.* 46 (2007) 7116–7118.
- [197] A.M. Chippindale, S.J. Hibble, E.J. Bilbé, E. Marelli, A.C. Hannon, C. Allain, R. Pansu, F. Hartl, Mixed copper, silver, and gold cyanides,  $(\text{M}_3\text{M}'_{1-x})\text{CN}$ : Tailoring chain structures to influence physical properties, *J. Am. Chem. Soc.* 134 (2012) 16387–16400.
- [198] M. Dapiaggi, H. Kim, E.S. Bozin, S.J.L. Billinge, G. Artioli, Study of the negative thermal expansion of cuprite-type structures by means of temperature-dependent pair distribution function analysis: Preliminary results, *J. Phys. Chem. Solid.* 69 (2008) 2182–2186.
- [199] K.W. Chapman, P.J. Chupas, Anomalous thermal expansion of cuprites: A combined high resolution pair distribution function and geometric analysis, *Chem. Mater.* 21 (2009) 425–431.
- [200] M.G. Tucker, A.L. Goodwin, M.T. Dove, D.A. Keen, S.A. Wells, J.S.O. Evans, Negative thermal expansion in  $\text{ZrW}_2\text{O}_8$ : Mechanisms, rigid unit modes, and neutron total scattering, *Phys. Rev. Lett.* 95 (2005), 255501.
- [201] M.G. Tucker, D.A. Keen, J.S.O. Evans, M.T. Dove, Local structure in  $\text{ZrW}_2\text{O}_8$  from neutron total scattering, *J. Phys. Condens. Matter* 19 (2007), 335215.
- [202] F. Bridges, T. Keiber, P. Juhas, S.J.L. Billinge, L. Sutton, J. Wilde, G.R. Kowach, Local vibrations and negative thermal expansion in  $\text{ZrW}_2\text{O}_8$ , *Phys. Rev. Lett.* 112 (2014), 045505.
- [203] M.-H. Tsai, J.-W. Yeh, High-entropy alloys: A critical review, *Mater. Res. Lett.* 2 (2014) 107–123.
- [204] H. Mauroy, K. Klyukin, M.G. Shelyapina, D.A. Keen, A. Thøgersen, B.C. Hauback, M.H. Sørbø, Short-range structure of  $\text{Ti}_{0.63}\text{V}_{0.27}\text{Fe}_{0.10}\text{D}_{1.73}$  from neutron total scattering and Reverse Monte Carlo modelling, *Energies* 13 (2020) 1947.
- [205] B. Jiang, C.A. Bridges, R.R. Unocic, K.C. Pitike, V.R. Cooper, Y. Zhang, D.-Y. Lin, K. Page, Probing the local site disorder and distortion in pyrochlore high-entropy oxides, *J. Am. Chem. Soc.* 143 (2021) 4193–4204.
- [206] M.W. Terban, S.J.L. Billinge, Structural analysis of molecular materials using the pair distribution function, *Chem. Rev.* 122 (2022) 1208–1272.
- [207] H.D. Duncan, M.T. Dove, D.A. Keen, A.E. Phillips, Local structure of the metal–organic perovskite dimethylammonium manganese(ii) formate, *Dalton Trans.* 45 (2016) 4380–4391.
- [208] H.D. Duncan, E.O.R. Beake, H.Y. Playford, M.T. Dove, A.E. Phillips, Local structure of a switchable dielectric Prussian blue analogue, *CrystEngComm* 19 (2017) 7316–7321.
- [209] E.O.R. Beake, M.G. Tucker, M.T. Dove, A.E. Phillips, Orientational disorder in adamantane and adamantanecarboxylic acid, *ChemPhysChem* 18 (2017) 459–464.
- [210] G. Cai, A.E. Phillips, D.A. Keen, M.G. Tucker, M.T. Dove, Neutron scattering study of the orientational disorder in potassium cyanide, *J. Phys. Commun.* 4 (2020), 023001.
- [211] G. Cai, A.E. Phillips, M.G. Tucker, M.T. Dove, Neutron scattering study of the orientational disorder and phase transitions in barium carbonate, *J. Phys. Condens. Matter* 32 (2020), 374014.
- [212] Y. Qin, S. Zhang, S. Zhang, M.G. Tucker, D.A. Keen, G. Cai, A.E. Phillips, M.T. Dove, Orientational order and phase transitions in deuterated methane: a neutron total scattering and reverse Monte Carlo study, *J. Phys. Condens. Matter* 34 (2021), 015401.
- [213] S. Zhang, Y. Qin, S. Zhang, M. Gao, M.G. Tucker, D.A. Keen, G. Cai, A.E. Phillips, M.T. Dove, Orientational disorder in sulfur hexafluoride: a neutron total scattering and reverse Monte Carlo study, *J. Phys. Condens. Matter* 34 (2022), 295401.
- [214] I.M. Svishechev, P.G. Kusalik, Structure in liquid water: a study of spatial distribution functions, *J. Chem. Phys.* 99 (1993) 3049–3058.
- [215] P.G. Kusalik, I.M. Svishechev, The spatial structure in liquid water, *Science* 265 (1994) 1219–1221.
- [216] A. Soper, Spherical-harmonic reconstruction of liquids diffraction data, *Phys. B: Condens. Matter* 213–214 (1995) 448–453.
- [217] A. Soper, Estimating the three-body correlation function for a liquid using spherical harmonic analysis, *Nucl. Instrum. Methods Phys. Res. Sect. A: Accel. Spectrom. Detect. Assoc. Equip.* 354 (1995) 87–95.
- [218] E.L. Smith, A.P. Abbott, K.S. Ryder, Deep eutectic solvents (DESS) and their applications, *Chem. Rev.* 114 (2014) 11060–11082.
- [219] S. Hammond, K.J. Edler, Structure and Implications, John Wiley & Sons, Ltd, (2019), pp. 25–42.
- [220] K. De Oliveira Vigier, F. Jérôme, Synthesis and Properties, John Wiley & Sons, Ltd, (2019), pp. 1–23.
- [221] H. Vanda, R. Verpoorte, P.G.L. Klinkhamer, Y.H. Choi, Natural Deep Eutectic Solvents: from Their Discovery to Their Applications, John Wiley & Sons, Ltd, (2019), pp. 61–81.
- [222] A.P. Abbott, G. Capper, D.L. Davies, R.K. Rasheed, V. Tambyrajah, Novel solvent properties of choline chloride/urea mixtures, *Chem. Commun.* (2003) 70–71.
- [223] O.S. Hammond, R. Atri, D.T. Bowron, K.J. Edler, Neutron diffraction study of indole solvation in deep eutectic systems of choline chloride, malic acid, and water, *Chem. Eur. J.* 28 (2022), e202200566.
- [224] O.S. Hammond, D.T. Bowron, A.J. Jackson, T. Arnold, A. Sanchez-Fernandez, N. Tsapatsaris, V. Garcia Sakai, K.J. Edler, Resilience of malic acid natural deep eutectic solvent nanostructure to solidification and hydration, *J. Phys. Chem. B* 121 (2017) 7473–7483.
- [225] T. Proffen, R.B. Neder, *DISCUS*, a program for diffuse scattering and defect structure simulations – update, *J. Appl. Crystallogr.* 32 (1999) 838–839.
- [226] R.B. Neder, V.I. Korsunskiy, Structure of nanoparticles from powder diffraction data using the pair distribution function, *J. Phys. Condens. Matter* 17 (2005) S125–S134.



- [227] K. Page, T.C. Hood, T. Proffen, R.B. Neder, Building and refining complete nanoparticle structures with total scattering data, *J. Appl. Crystallogr.* 44 (2011) 327–336.
- [228] A.S. Masadeh, Total scattering atomic pair distribution function: new methodology for nanostructure determination, *J. Exp. Nanosci.* 11 (2016) 951–974.
- [229] H.L. Andersen, B.A. Frandsen, H.P. Gunnlaugsson, M.R.V. Jørgensen, S.J.L. Billinge, K.M.Ø. Jensen, M. Christensen, Local and long-range atomic/magnetic structure of non-stoichiometric spinel iron oxide nanocrystallites, *IUCr* 8 (2021) 33–45.
- [230] A.L.-T. Pham, C. Lee, F.M. Doyle, D.L. Sedlak, A silica-supported iron oxide catalyst capable of activating hydrogen peroxide at neutral pH values, *Environ. Sci. Technol.* 43 (2009) 8930–8935.
- [231] I.C. Lekshmi, R. Buonsanti, C. Nobile, R. Rinaldi, P.D. Cozzoli, G. Maruccio, Tunneling magnetoresistance with sign inversion in junctions based on iron oxide nanocrystal superlattices, *ACS Nano* 5 (2011) 1731–1738.
- [232] S.-I. Ohkoshi, A. Namai, M. Yoshikiyo, K. Imoto, K. Tamazaki, K. Matsuno, O. Inoue, T. Ide, K. Masada, M. Goto, T. Goto, T. Yoshida, T. Miyazaki, Multimetal-substituted epsilon-iron oxide  $\epsilon\text{-Ga}_{0.31}\text{Ti}_{0.05}\text{Co}_{0.05}\text{Fe}_{1.59}\text{O}_3$  for next-generation magnetic recording tape in the big-data era, *Angew. Chem. Int. Ed.* 55 (2016) 11403–11406.
- [233] Q.A. Pankhurst, J. Connolly, S.K. Jones, J. Dobson, Applications of magnetic nanoparticles in biomedicine, *J. Phys. D: Appl. Phys.* 36 (2003) R167–R181.
- [234] C.C. Berry, A.S.G. Curtis, Functionalisation of magnetic nanoparticles for applications in biomedicine, *J. Phys. Appl. Phys. D: Appl. Phys.* 36 (2003) R198–R206.
- [235] J.-H. Lee, Y.-M. Huh, Y.-W. Jun, J.-W. Seo, J.-T. Jang, H.-T. Song, S. Kim, E.-J. Cho, H.-G. Yoon, J.-S. Suh, J. Cheon, Artificially engineered magnetic nanoparticles for ultra-sensitive molecular imaging, *Nat. Med.* 13 (2007) 95–99.
- [236] H.B. Na, I.C. Song, T. Hyeon, Inorganic nanoparticles for MRI contrast agents, *Adv. Mater.* 21 (2009) 2133–2148.
- [237] J.-t. Jang, H. Nah, J.-H. Lee, S. Moon, M. Kim, J. Cheon, Critical enhancements of MRI contrast and hyperthermic effects by dopant-controlled magnetic nanoparticles, *Angew. Chem. Int. Ed.* 48 (2009) 1234–1238.
- [238] C.A. Quinto, P. Mohindra, S. Tong, G. Bao, Multifunctional superparamagnetic iron oxide nanoparticles for combined chemotherapy and hyperthermia cancer treatment, *Nanoscale* 7 (2015) 12728–12736.
- [239] E. Shugam, H. Zhdanov, The crystal structure of cyanides. The structure of  $\text{Cd}(\text{CN})_2$ , *Acta Physicochimica URSS* 20 (1945) 247–252.
- [240] B.F. Hoskins, R. Robson, Design and construction of a new class of scaffolding-like materials comprising infinite polymeric frameworks of 3D-linked molecular rods. A reappraisal of the zinc cyanide and cadmium cyanide structures and the synthesis and structure of the diamond-related frameworks  $[\text{N}(\text{CH}_3)_4][\text{Cu}^{\text{II}}(\text{CN})_4]$  and  $\text{Cu}^{[4, 4', 4'', 4''']}\text{-tetracyanotetraphenylmethane}[\text{BF}_4]\text{x}\text{C}_6\text{H}_5\text{NO}_2$ , *J. Am. Chem. Soc.* 112 (1990) 1546–1554.
- [241] D. Williams, D. Partin, F. Lincoln, J. Kouvatakis, M. O'Keefe, The disordered crystal structures of  $\text{Zn}(\text{CN})_2$  and  $\text{Ga}(\text{CN})_3$ , *J. Solid State Chem.* 134 (1997) 164–169.
- [242] V.E. Fairbank, A.L. Thompson, R.I. Cooper, A.L. Goodwin, Charge-ice dynamics in the negative thermal expansion material  $\text{Cd}(\text{CN})_2$ , *Phys. Rev. B* 86 (2012), 104113.
- [243] C.S. Coates, M. Baise, A. Schmutzler, A. Simonov, J.W. Makepeace, A.G. Seel, R.I. Smith, H.Y. Playford, D.A. Keen, R. Siegel, J. Senker, B. Slater, A.L. Goodwin, Spin-ice physics in cadmium cyanide, *Nat. Commun.* 12 (2021) 2272.
- [244] D.A. Keen, R.L. McGreevy, Determination of disordered magnetic structures by RMC modelling of neutron diffraction data, *J. Phys. Condens. Matter* 3 (1991) 7383–7394.
- [245] D. Keen, R. McGreevy, R. Bewley, R. Cywinski, Magnetic structure determination of amorphous materials using RMC modelling of neutron diffraction data, *Nucl. Instrum. Methods Phys. Res. Sect. A: Accel. Spectrom. Detect. Assoc. Equip.* 354 (1995) 48–52.
- [246] D.A. Keen, R.I. Bewley, R. Cywinski, R.L. McGreevy, Spin configurations in an amorphous random-anisotropy magnet, *Phys. Rev. B* 54 (1996) 1036–1042.
- [247] L. Karlsson, A. Wannberg, R.L. McGreevy, D.A. Keen, Modeling the magnetic structure of  $\text{Dy}_7\text{Fe}_3$  metallic glass, *Phys. Rev. B* 61 (2000) 487–491.
- [248] A.L. Goodwin, M.G. Tucker, M.T. Dove, D.A. Keen, Magnetic structure of  $\text{MnO}$  at 10 K from total neutron scattering data, *Phys. Rev. Lett.* 96 (2006), 047209.
- [249] J.A.M. Paddison, M.J. Gutmann, J.R. Stewart, M.G. Tucker, M.T. Dove, D.A. Keen, A.L. Goodwin, Magnetic structure of paramagnetic  $\text{MnO}$ , *Phys. Rev. B* 97 (2018), 014429.
- [250] P.J. Saines, J.A.M. Paddison, P.M.M. Thygesen, M.G. Tucker, Searching beyond Gd for magnetocaloric frameworks: magnetic properties and interactions of the  $\text{Ln}(\text{HCO}_2)_3$  series, *Mater. Horiz.* 2 (2015) 528–535.
- [251] P.M.M. Thygesen, C.A. Young, E.O.R. Beake, F.D. Romero, L.D. Connor, T.E. Proffen, A.E. Phillips, M.G. Tucker, M.A. Hayward, D.A. Keen, A.L. Goodwin, Local structure study of the orbital order/disorder transition in  $\text{LaMnO}_3$ , *Phys. Rev. B* 95 (2017), 174107.
- [252] R.J.C. Dixey, G.B.G. Stenning, P. Manuel, F. Orlandi, P.J. Saines, Ferromagnetic Ising chains in frustrated  $\text{LnODCO}_3$ : the influence of magnetic structure in magnetocaloric frameworks, *J. Mater. Chem. C* 7 (2019) 13111–13119.
- [253] J.A.M. Paddison, J.R. Stewart, A.L. Goodwin, SPINVERT: a program for refinement of paramagnetic diffuse scattering data, *J. Phys. Condens. Matter* 25 (2013), 454220.
- [254] A. Herlihy, H.S. Geddes, G.C. Sosso, C.L. Bull, C.J. Ridley, A.L. Goodwin, M.S. Senn, N.P. Funnell, Recovering local structure information from high-pressure total scattering experiments, *J. Appl. Crystallogr.* 54 (2021) 1546–1554.
- [255] M.G. Tucker, M.T. Dove, D.A. Keen, Simultaneous analysis of changes in long-range and short-range structural order at the displacive phase transition in quartz, *J. Phys. Condens. Matter* 12 (2000) L723–L730.
- [256] M.G. Tucker, D.A. Keen, M.T. Dove, A detailed structural characterization of quartz on heating through the  $\alpha$ - $\beta$  phase transition, *Mineral. Mag.* 65 (2001) 489–507.
- [257] M.G. Tucker, M.P. Squires, M.T. Dove, D.A. Keen, Dynamic structural disorder in cristobalite: neutron total scattering measurement and reverse Monte Carlo modelling, *J. Phys. Condens. Matter* 13 (2000) 403–423.
- [258] T. Weber, A. Simonov, The three-dimensional pair distribution function analysis of disordered single crystals: basic concepts, *Z. Kristallogr.* 227 (2012) 238–247.
- [259] Z.J. Morgan, H.D. Zhou, B.C. Chakoumakos, F. Ye, *rmc-discord*: reverse Monte Carlo refinement of diffuse scattering and correlated disorder from single crystals, *J. Appl. Crystallogr.* 54 (2021) 1867–1885.
- [260] P. Upreti, M. Krogstad, C. Haley, M. Anitescu, V. Rao, L. Poudel, O. Chmaissem, S. Rosenkranz, R. Osborn, Order-disorder transitions in  $(\text{Ca}_x\text{Sr}_{1-x})_3\text{Rh}_4\text{Sn}_{13}$ , *Phys. Rev. Lett.* 128 (2022), 095701.
- [261] S.D. Funni, Z.J. Yang, M.J. Cabral, C. Ophus, X.M. Chen, E.C. Dickey, Theory and application of the vector pair correlation function for real-space crystallographic analysis of order/disorder correlations from STEM images, *Apl. Mater.* 9 (2021), 091110.
- [262] R. Baral, J.A. Christensen, P.K. Hamilton, F. Ye, K. Chesnel, T.D. Sparks, R. Ward, J. Yan, M.A. McGuire, M.E. Manley, J.B. Staunton, R.P. Hermann, B.A. Frandsen, Real-space visualization of short-range antiferromagnetic correlations in a magnetically enhanced thermoelectric, *Matter* 5 (2022) 1853–1864.
- [263] D.A. Dimitrov, D. Louca, H. Röder, Phonons from neutron powder diffraction, *Phys. Rev. B* 60 (1999) 6204–6207.
- [264] W. Reichardt, L. Pintschovius, Influence of phonons on the pair distribution function deduced from neutron powder diffraction, *Phys. Rev. B* 63 (2001), 174302.
- [265] M.J. Graf, I.-K. Jeong, D.L. Starr, R.H. Heffner, Limits on phonon information extracted from neutron pair-density functions, *Phys. Rev. B* 68 (2003), 064305.
- [266] A.L. Goodwin, M.G. Tucker, M.T. Dove, D.A. Keen, Phonons from powder diffraction: a quantitative model-independent evaluation, *Phys. Rev. Lett.* 93 (2004), 075502.
- [267] A.L. Goodwin, M.T. Dove, M.G. Tucker, D.A. Keen,  $\text{MnO}$  spin-wave dispersion curves from neutron powder diffraction, *Phys. Rev. B* 75 (2007), 075423.
- [268] M. Bée, *Quasielastic Neutron Scattering: Principles and Applications in Solid State Chemistry, Biology, and Materials Science*, Adam Hilger, Bristol, UK, 1988.



**Prof Martin Dove** received his BSc and PhD in Physics from the University of Birmingham. After post-doctoral positions in Physics at the University of Edinburgh and Theoretical Chemistry at the University of Cambridge, he was appointed to a faculty position in the Department of Earth Science in the University of Cambridge in 1986. In 2011 he moved to the School of Physical and Chemical Sciences in Queen Mary University of London. Since 2019 he has been Professor in Sichuan University, with visiting positions in Wuhan University of Technology and Dongguan University of Technology. His primary research interests are in understanding the atomic structure of materials and in understanding how structure affects physical properties. His research frequently uses experiments with radiation beams (particularly the ISIS spallation neutron source in the UK) and computer simulation. He has a long-standing interest in disordered materials, both crystalline and amorphous, and in issues such as the flexibilities of networks, lattice dynamics, and phenomena such as phase transitions and negative thermal expansion. He is one of the key developers of the application of the RMC method to crystalline systems.



**Prof Gong Li** received her PhD in Condensed matter physics from the Institute of Physics, Chinese Academy of Sciences. After a post-doctoral position in Metal physics at the Max-Planck-Institut für Metal, she obtained a professorial position in the State Key Laboratory of Metastable Materials Science and Technology in Yanshan University. From 2012 to 2017 she held a visiting position in The University of Tennessee, undertaking research on disordered multi-principal element alloys using synchrotron radiation in Argonne National Laboratory, and neutrons in the Oak Ridge National Laboratory. During Spring 2019 she visited Rice University, Texas, to develop a new direction of scientific research on Bio-materials. Her current research interests include phase transitions and effects on properties under extreme condition, particularly in disordered system, including metals, inorganic non-metallic and small organic materials by synchrotron and neutron sources.